INVESTIGATING HEMODYNAMICS OF THE DEVELOPING EMBRYONIC HEART USING OPTICAL COHERENCE TOMOGRAPHY

by

LINDSY M. PETERSON

Submitted in partial fulfillment of the requirements

For the degree of Doctor of Philosophy

Dissertation Adviser: Dr. Andrew M. Rollins

Department of Biomedical Engineering

CASE WESTERN RESERVE UNIVERSITY

May, 2015

CASE WESTERN RESERVE UNIVERSITY

SCHOOL OF GRADUATE STUDIES

We hereby approve the thesis/dissertation of

Lindsy M. Peterson

candidate for degree of Ph.D. *.

Andrew M. Rollins

(signed)_____

(chair of the committee)

Michiko Watanabe

_____

David L. Wilson

_____

Kenneth D. Singer

_____

(date) _____ March 18th 2015 _____

*We also certify that written approval has been obtained for any proprietary material contained therein.

Table of Contents

List of Tables

List of Figures

Acknowledgements

I have been very lucky to be part of an amazing lab here at Case Western Reserve University. I am thankful to all the present and past members that have helped me throughout the years. I am especially thankful to my advisor Dr. Andrew Rollins for all his patience, support, and guidance during my graduate studies. I would also like to thank the other members of my committee, Dr. Michiko Watanabe, Dr. David Wilson, and Dr. Kenneth Singer, for their advice and assistance throughout my thesis work.

I also need to thank all the amazing friends that I have made here that have helped me maintain my sanity. I was fortunate welcomed into a lab environment filled with people that have been supportive colleagues as well as priceless friends. Thank you to Ganga, Pei, Mike, Sid, Wei, Big Zhao, Little Zhao, and Lynn for all the Rock Band and Dance Central sessions. Also thanks to the guys that I met when we all first started here at Case, Yves, Nathan, and Dan for all the memorable board game evenings.

Finally, I would like to thank my wonderful family. My parents for telling me that I could do anything I want with my life and giving me the opportunities, support, inspiration, and love needed to accomplish my goals. My grandparents for their love and for being there for all the important moments in my life. My loving sisters for being my very best friends and being inspirations for me to strive to be the very best that I can be. I am blessed to have incredibly supportive family members who have helped to shape me into the person that I am today and for that I am eternally thankful.

List of Abbreviations

AA	Arch of the Aorta
A-scan	Axial Scan
AV	Atrioventricular
B-scan	Cross sectional image
CHD	Congenital Heart Defect
CNCC	Cardiac Neural Crest Cell
CytoD	Cytochalasin D
DOCT	Doppler Optical Coherence Tomography
ET-1	Endothelin 1
FAS	Fetal Alcohol Syndrome
FDML	Fourier Domain Mode Locking
FD-OCT	Fourier Domain Optical Coherence Tomography
FFT	Fast Fourier Transform
FWHM	Full Width Half Max
GPU	Graphics Processing Unit
HH	Hamburger Hamilton
InGaAs	Indium Gallium Arsenide
KLF2	Krüppel-Like Factor 2
LBA	Left Brachiocephalic Artery
LPA	Left Pulmonary Artery
NCC	Neural Crest Cell
NOS-3	Nitric Oxide Synthase 3
OCT	Optical Coherence Tomography

OFDI	Optical Frequency Domain Imaging
OP	Optical Pacing
OSI	Oscillatory Shear Index
pERK	Phosphorylated Extracellular Signal-Regulated Kinase
PTA	Persistent Truncus Arteriosis
RBA	Right Brachiocephalic Artery
RPA	Right Pulmonary Artery
SD	Standard Deviation
SD-OCT	Spectral Domain Optical Coherence Tomography
SNR	Signal to Noise Ratio
SS-OCT	Swept Source Optical Coherence Tomography
STFFT	Short Time Fast Fourier Transform
TD-OCT	Time Domain Optical Coherence Tomography
TEASAR	Tree-Structure Extraction Algorithm delivering Skeletons that are Accurate and Robust
VSD	Ventricular Septal Defects
WSS	Wall Shear Stress
µPIV	Micro Particle Image Velocimetry

Investigating Hemodynamics of the Developing Embryonic Heart using Optical Coherence Tomography

Abstract

By

LINDSY PETERSON

Blood flow is a critical factor that regulates developmental programs during cardiogenesis. During early embryonic development, deviations from the normal blood flow pattern have been shown to lead to congenital heart defects including septal defects and outflow tract anomalies. To better understand the role flow and the resulting hemodynamic forces play during cardiovascular development precise tools are needed to rapidly calculate and monitor these forces. Optical coherence tomography (OCT) is a noninvasive imaging modality that is well suited for imaging the developing heart due to its high spatial and temporal resolution. OCT is also capable of analyzing various cardiac functions by measuring the blood flow through the developing heart via the Doppler effect. Here we present several techniques we have developed that use structural and Doppler OCT to monitor and measure hemodynamic parameters in the early embryonic heart. First, we generated 4-D (3-D volumes over time) shear stress maps from Doppler OCT data sets. These maps enabled comparisons of shear stress from the inner curvature versus the outer curvature at different regions of the looping heart tube over the duration of a heartbeat. We also developed an

orientation independent technique for measuring the absolute blood flow in a vessel from individual cross sectional images. This technique utilizes a dual angle delay encoding technique to obtain instantaneous pulsatile blood flow measurements irrespective of the vessel orientation. We used this technique to image the aortic arches in control and ethanol exposed embryos. The aortic arches undergo a significant morphogenesis from a symmetrical system of paired vessels to an asymmetrical structure and hemodynamics is thought to play a critical role in this transformation. Blood flow and shear stress were both calculated as well as the cross sectional area of the pharyngeal tissue surrounding the aortic arch vessel. Finally, we developed a technique for measuring the contractile wave velocity in different regions of the heart tube. These values were then compared with conduction velocities obtained from optical mapping. Here we have developed and demonstrated a range of novel techniques for measuring cardiac function in the developing embryonic heart. These techniques may prove to be powerful tools for future investigations of the role of blood flow and the resulting hemodynamic forces play in congenital heart defects.

Chapter 1: Background

1.1 Congenital Heart Disease

In the US, congenital heart disease (CHD) occurs in approximately 8 of every 1000 live births [1]. An estimated 32,000 infants are expected to be affected with CHDs each year and of these 25% will require invasive treatment within the first year of life [2]. These defects include coarctation of the aorta, d-transposition of the great arteries, valve stenosis, atrioventricular (AV) canal defects, and Tetralogy of Fallot [3]. Due to this prevalence, the developing embryonic heart and vasculature have been widely investigated in an attempt to better understand the origins of CHDs. Unfortunately many of the mechanisms which result in these defects remain poorly understood. Surgical techniques and treatments for patients with CHDs have dramatically improved, however patients still may require follow-up interventions and lifetime monitoring [4]. In order to potentially prevent CHDs from occurring, a better understanding of the underlying mechanism is required.

1.2 Embryonic Cardiology

Invasive imaging of early embryonic human hearts is not possible. Therefore, a range of animal models have been employed in order to study the various mechanism of cardiac development. Fortunately, many of the mechanisms of heart development seem to have been highly conserved. Different models have been utilized based on the topic of interest as well as the technology employed. Avian (chicken/quail), mouse, zebrafish, drosophila, and xenopus have been some of the most widely studied animal models.

The widely-used mouse model has clear advantages for use in elucidating mechanisms of cardiovascular development, one being that, like humans, they are mammalian. The genetics and molecular biology of the murine model is well known and remains a popular area of study. There are also a wide variety of mouse lines available for the study of cardiac development and disease. These mouse lines can be crossed to study genetic interactions and conditional knockout technology now allows us to alter genes in specific cell types. Unfortunately, accessing the mouse embryo during development is a challenge. It is difficult to image through the maternal abdominal wall and the uterus with high enough resolution to visualize the developing heart. A balance must be struck between depth penetration and imaging resolution when visualizing early mouse development. Imaging has been performed *in utero* in which the uterine horn is externalized by Cesarian section and imaged externally. In this procedure, the pregnant mouse is anesthetized, an incision is made on the lower abdomen, a portion of the uterine horn is externalized and imaged, and then the uterine horn is returned and the incision closed with sutures [5]. This allowed for multiple imaging sessions at different stages of development however, it is unclear how the anesthesia and overall surgery may influence the cardiac functions of the embryo. Groups have also removed mouse embryos entirely from the uterus for *ex vivo* imaging [6, 7]. The embryos are then cultured in some form of serum or media. Unfortunately, this procedure involves making an incision in the yolk sac of the mouse embryo potentially rupturing vessels necessary for proper cardiac function.

The work presented here focuses on the use of avian embryos as a model for heart development. Avian embryos much like mammals, develop a fully septated, four chambered heart that is very similar in structure and physiology to the human heart [8]. The gestation period for quails is around 16-18 days allowing for the rapid visualization of the effects of perturbations and interventions. Fertilized quail eggs are very economical and easy to obtain (commercially available) and grow. Once the eggs are obtained they only require an incubator that allows for temperature and humidity controls. Quail embryos are also easily accessible. The eggs can be "windowed" that is a hole can be made in the egg shell and then covered with glass or plastic film. Alternatively the egg shell can be removed entirely to produce a shell-less culture. In this case the egg shell is cracked and the contents of the egg placed in either a sterile Petri dish or some other covered container [9, 10]. Each procedure allows the avian embryos to develop under near physiological conditions until very late stages of development allowing for investigations of cardiac function. One shortcoming to the avian model is that the study of their genetics is less developed in comparison to other animal models. However, this is being overcome by increasing our knowledge of the chicken and other avian genomes [11-15].

The heart first begins as a pair of bilaterally paired cardiogenic fields of cells [8]. These precursor cells then migrate and fuse together to form the heart tube. This midline heart tube contains blood flowing from the inflow at the caudal end to the cranial outflow tract. The heart tube then lengthens and begins to loop to the right initially into a C shape and then an S shape. Cardiac looping is one of

the first visible structural signs of left-right asymmetry of the body. The early stage of cardiac looping is also around the time that the heart first begins to beat. The looping contortions continue and bring the inflow section of the heart tube closer to the outflow tract at the cranial end of the embryo in a process called convergence. This proximity precedes septation. The cardiac cushions emerge from the myocardial wall of the atrioventricular canal to separate the atrium from the ventricle and later into the right and left AV canals. The cardiac cushions transform into the valve leaflets necessary to maintain the proper direction of blood flow. We have focused on investigations during the stages of cardiac looping. These stages of development include complex processes whose mechanisms have yet to be completely understood [16, 17]. Abnormal looping has been shown to precede congenital heart defects such as transposition of the great arteries and valvuloseptal defects [18]. Direct observation of the looping heart has been challenging due to the small size and rapidly changing nature of the 3-D changes involved in heart development.

1.3 Model of Fetal Alcohol Syndrome (FAS) by Prenatal Alcohol Exposure

Various perturbation models have been investigated in order to gain a better understanding of the mechanisms of cardiac development. One such perturbation model is fetal ethanol exposure that results in craniofacial and cardiac defects. In the United States more than 500,000 women were reported to consume alcohol at some point during pregnancy, despite maternal alcohol intake being known to cause birth defects [19]. Additionally, 1 in 5 of this population admitted to binge drinking, which for women is defined as 4 or more

drinks per session. Since pregnancy is usually not recognized until approximately 5 weeks after conception and as many as half of the pregnancies in the United States are unplanned [20], many women may be consuming alcohol before they even realize they are pregnant. Even a single dose of prenatal ethanol exposure can result in birth defects termed Fetal Alcohol Syndrome (FAS). FAS is commonly associated with craniofacial abnormalities such as a thin upper lip and absence of a philtrum [21, 22]. It is also associated with growth retardation and neurological abnormalities. However, one aspect of the disease that is commonly overlooked is that as many as 54% of live-born children with FAS present with some kind of cardiac anomaly [23]. These anomalies commonly include outflow tract anomalies and valvuloseptal defects [24]. Despite many studies and proposed hypotheses focusing on the molecular mechanisms of ethanol induced heart defects [25-28], the precise mechanisms remain largely unclear.

We have developed an ethanol exposure protocol for quail embryos that produces cardiac defects associated with FAS [29]. In this model, the embryos are exposed to ethanol at HH stage 4-5 [30] while the embryo is in the stage of gastrulation. The eggs are injected into the air gap with 40 μL of 50% ethanol in saline. This single dosage of ethanol was based on previously established protocols and is equivalent to a binge drinking episode in humans [28]. This is approximately equivalent to a blood alcohol content of 0.179%. Using this model we have observed altered cardiovascular structure and function at early stages of developmental [29] as well as congenital heart defects at later stage hearts [31]. We believe that the altered cardiac function at earlier stages of development may

17

be playing a causal role in the development of the congenital heart defects observed at later stages.

1.4 Hemodynamic Forces during Development

As blood flows through the heart and vasculature it exerts forces on the embryo. The blood flow creates a wall shear stress (WSS) due to the dragging of the blood flow along the vessel walls, a force from the pressure of the blood flow, circumferential strain from vessel deformation resulting from pressure, as well as many others. These forces play a critical role in the developing cardiovascular system and deviations from normal blood flow patterns have been shown to lead to congenital heart defects [32-36]. Ligation of the vitelline vein in avian embryos altered blood flow in the outflow tract and induced ventricular septum defects (VSDs), semilunar valve anomalies, and pharyngeal arch artery malformations [32, 37]. It has also been shown that retrograde blood flow in the looping heart is critical for proper valve development [38]. Even alterations in heart rate have been shown to influence heart development. Through the use of optical pacing [39] we have demonstrated that altering the embryonic heart rate results in early hemodynamic forces alterations [40] as well as late stage heart valvulospetal defects [41].

Hemodynamic forces clearly play a significant role in heart development and are critical for the proper formation of the cardiovascular system. This is due in part to the wide variety of signaling molecules whose expression and activity are influenced by alterations in biomechanical forces. Some of these proteins including KLF2, ET-1, NOS-3, and pERK which have all been shown to be

influenced by hemodynamic forces and play a role in the developing avian cardiovascular system [38, 42-46]. Abnormal biomechanical forces lead to altered molecular expression that can result in altered cardiac structure. Abnormal cardiac structure then results in altered function which in turn alters molecular expression (Figure 1.1). This feedback loop is poorly understood due to the lack of appropriate imaging tools to capture function. In order to better understand the connection between mechanotransducing molecules, blood flow-induced forces, and heart development, it is important for us to be able to accurately visualize, measure, and monitor hemodynamic forces.
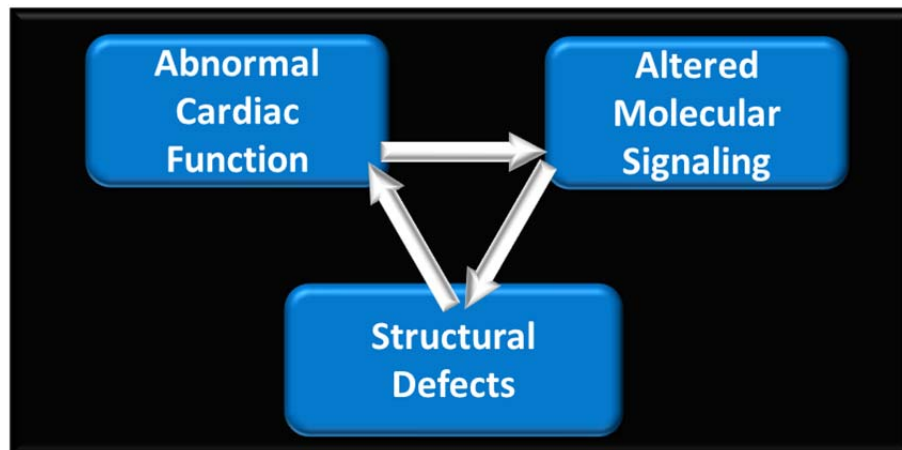
Figure 1.1: Cardiac function feedback loop.

Abnormal cardiac function is transduced and alters gene and molecular expression, which alters cardiac structure. The altered structure then results in abnormal cardiac function which alters molecular signaling. This feedback loop is poorly understood because of the lack of proper tools to assess the forces on the early looping heart and their resultant effects in cardiogenesis.

1.5 History of Cardiac Function Imaging

The earliest investigations of cardiovascular hemodynamics focused on visual observation of flow patterns [47, 48]. These were performed through visual observation of the erythrocytes traveling through the vasculature. Dye injections such as india ink and methylene blue have also been utilized to greatly improve our ability to visualize the flow dynamics [49-52]. Injections at various stages of development have yielded insight into how fluid patterns change during the course of development. However, these studies depend largely on the injection site of the dye and remain largely qualitative. The injection itself could add substantial volume to early embryonic CV system that could alter blood flow. Dye injections also are restricted to visualizing a 2-D projection of the vessel network, when in fact the fluid is flowing in 3 dimensions.

Micro particle image velocimetry (µPIV) is another very useful technique for visualizing fluid flow as well as measuring blood flow velocities. µPIV is performed by measuring the displacement of tracer particles between two consecutive images captured within a small time interval. The images are typically acquired through the use of a high speed camera coupled with a microscope or high speed confocal imaging. The displacements of the particles are then calculated by using a cross correlation algorithm. This technique can be applied by either using the red blood cells [53] or an exogenous tracer particle injected into the system [34, 54]. µPIV has also been demonstrated by imaging zebrafish with transgenically labeled endothelial and red blood cells. In addition to blood velocities, µPIV measurements have been used to calculate shear

stress in the developing heart and aortic arches [34, 55, 56]. Unfortunately, µPIV also suffers from the fact that it is a 2-D measurement of a 3 dimensional structure. It results in a field of 2-D velocity vectors which has provided many insights into the developing cardiac function; however it does not completely portray the 3-D hemodynamic forces that are present in a heart that is undergoing complex morphogenesis.

For years, ultrasound has been used to visualize and monitor developing embryos. By making use of the Doppler effect, Doppler ultrasound is able to measure the phase shift between sequential pulses to determine the velocity of moving particles (e.g. blood cells). This technique enables measurements of a wide variety of cardiac functional parameters including stroke volume, blood velocity, cardiac output, ejection fraction, and many more [57-62]. Advances in high-frequency ultrasound systems, also known as ultrasound biomicroscopy, operate at higher center wavelengths (~40-100 MHz). The higher frequency enables imaging at higher resolutions (~30 µm) compared with diagnostic clinical transducers. This increased spatial resolution enables measurement of chamber specific cardiac flows as well as velocity measurements in vessels such as the aortic arches [59, 63-69].

1.6 Optical Coherence Tomography

Optical coherence tomography (OCT) has been widely used for both structural and functional imaging of a variety of embryonic models including avian [29, 31, 70-86], mouse [79, 87-90], zebrafish [91, 92], Drosophila [93, 94], and Xenopus [95-99]. OCT is a medical imaging modality that allows for cross sectional and 3-

D visualization of biological tissue with micrometer resolution. In the range of resolution and depth penetration, it lies between ultrasound and confocal microscopy. OCT was first demonstrated in 1991 [100] and is already widely used in the clinic to assist in the diagnosis of a variety of diseases in the eye [101]. In addition to ophthalmology and developmental biology, OCT has been adapted for use in imaging coronary arteries[102-104], gastrointestinal tract [105-107], pulmonary medicine [108], dermatology [109], dentistry [110], and many other applications.

1.6.1 Time Domain-OCT

OCT is analogous to ultrasound, and is a non-invasive imaging modality that measures backscattered light from a sample. Ultrasound is able to measure the transit time of the sound waves, however the speed of light makes this measurement challenging in OCT. Therefore, OCT measures the interference of the reflected light through the use of a photodetector. OCT uses an infrared light source which enables imaging approximately 1-2 mm in depth depending on the properties of the tissue. OCT measures the interference from the light that directly reflects back (backscattered light) and rejects the rest of the light which scatters multiple times before detection using a technique called interferometry. The large scattering coefficient of biological samples limits the amount of light that can be collected from structures located farther than approximately 2mm below the surface. The basic time-domain OCT system utilizes a Michelson interferometer (Figure 1.2). The incident light is split into two paths. Half of the light travels to the sample to be imaged while half the light goes to a reference

mirror. The backscattered or reflected light from the two paths is recombined and the inference fringes are detected by a photodetector. OCT makes use of short coherence length light sources in order to generate high axial resolution images. Light sources with broader bandwidths have shorter coherence lengths. The reflected light from the two paths will only interfere if they have traveled within one coherence length of each other. This coherence length determines the axial resolution of OCT. In OCT imaging the axial and lateral resolutions are decoupled from one another. The axial resolution is a function of the light source and is measured using the FWHM of the point spread function of a single reflector. The lateral resolution of an OCT system is determined by the spot size of the optical system determined by the numerical aperture of the focusing lens and can be assessed with a beam analyzer. The coherence length can then be used to select certain depths in the sample by moving the reference mirror position. Different depths of the sample can be imaged by scanning the reference mirror and demodulating the interference signal. This scan generates a single line of data which is termed an A-scan (Figure 1.3). By scanning the light incident on the sample through the use of galvanometers, multiple A-scans can be acquired to generate a B-scan or 2-D cross sectional image. This can be repeated in the other spatial dimension, resulting in the acquisition of multiple B-scans, to generate a 3-D volume.
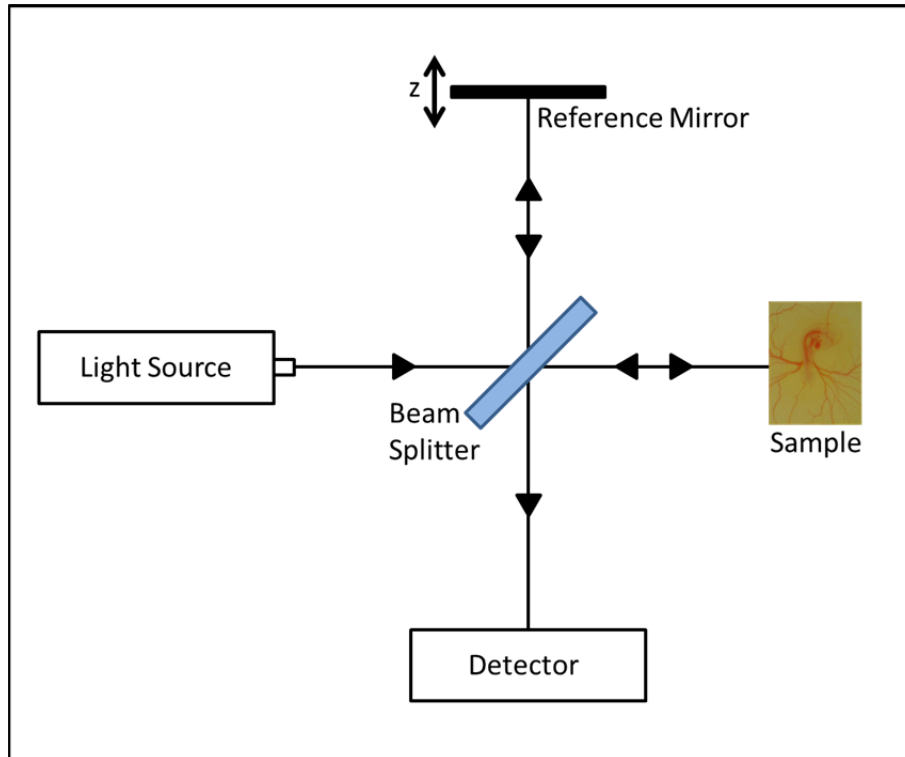
Figure 1.2: Time domain OCT schematic.

A modified Michelson interferometer is used to perform TD-OCT. The light is split into two paths

by a beam splitter. The backscattered light from both the sample and the reference mirror is then

measured by the detector. The reference mirror travels back and forth in order to visualize points

in depth in the sample.
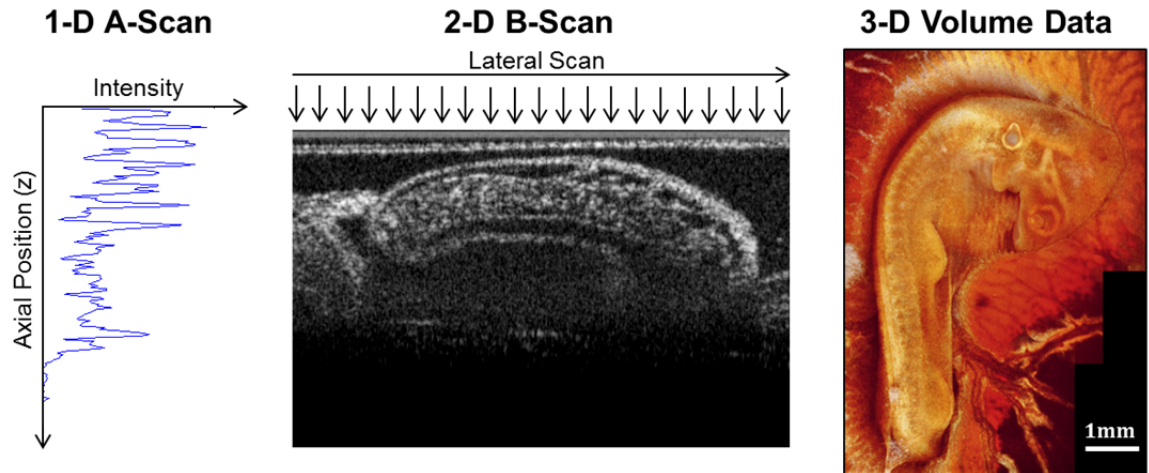
Figure 1.3: Different OCT scanning patterns.

A cross sectional OCT image is generated from multiple sequential A-scans. Each A-scan is obtained by translating the reference mirror to adjust the axial position in depth. By translating the imaging beam laterally along the sample, multiple A-scans can be acquired. The measured intensity can then be given grayscale values and displayed together to generate a B-scan as shown in the center image of an embryonic heart tube. Multiple B-scans can be acquired by repeating this lateral scanning along the last axis to generate a 3-D volumetric data set as shown in the right most image of a quail embryo.

The sources of noise in an OCT system generally consist of 3 different noises; shot noise, thermal noise, and excess intensity noise. Shot noise arises from the quantum nature of light. Light represented as photons emitted from a source is not entirely constant and exhibits some statistical fluctuations. This random arrival and detection of photons can be modeled as a Poisson distribution and is detected as noise. Excess intensity noise is fluctuations in the light source power resulting from beating within the linewidth of the optical source. Finally, thermal noise needs to be considered in any system that utilizes

electronic elements. It results from the random thermal fluctuations of electronics in receiver electronics. Ideal OCT systems attempt operate in the shot noise limited domain by reducing thermal and excess intensity noise. Thermal noise can be reduced by operating with sufficiently high reference arm power so that shot noise dominates, while excess intensity noise can be reduced through the use of dual-balanced detection.

1.6.2 FD-OCT

The next generation of OCT systems was termed Fourier domain OCT systems in which the reference mirror is fixed. The depth information instead is determined through the use of a Fourier transform. FD-OCT has been demonstrated to have significantly improved SNR compared to TD-OCT [111-113]. Imaging speeds were also significantly increased in FD-OCT due to the use of a static reference mirror. In TD-OCT systems, each point on an A-scan was acquired individually where as in FD-OCT systems, the entire A-scan is acquired simultaneously. There are two different methods to perform FDOCT imaging based on the light source used and the detection methods (Figure 1.4). In spectral domain OCT, a spectrometer present in the detection arm of the system disperses the light into a high speed line scanning camera. Each pixel in the line scanning camera detects a different portion of the spectrum and all wavelengths are detected simultaneously [114, 115]. The other method is swept source OCT (SS-OCT) [116] otherwise known as optical frequency domain imaging (OFDI) [117]. SS-OCT utilizes a rapidly sweeping laser that generates narrow bands of the spectrum in sequence. The narrow portions of the spectrum are detected by

a simple photodetector as a function of time. Recent advancements in light sources have enabled the creation of ultrahigh speed SSOCT systems. Fourier domain mode locked (FDML) lasers function by adjusting the cavity roundtrip time to be in sync with the intracavity wavelength filter [118]. This results in all wavelengths being active within the cavity simultaneously allowing for rapid tuning limited only by the filter. Buffered FDML lasers use multiple outputs from the cavity enabling SSOCT systems of acquiring A-scans at megahertz rates and real-time volumetric imaging [119, 120].
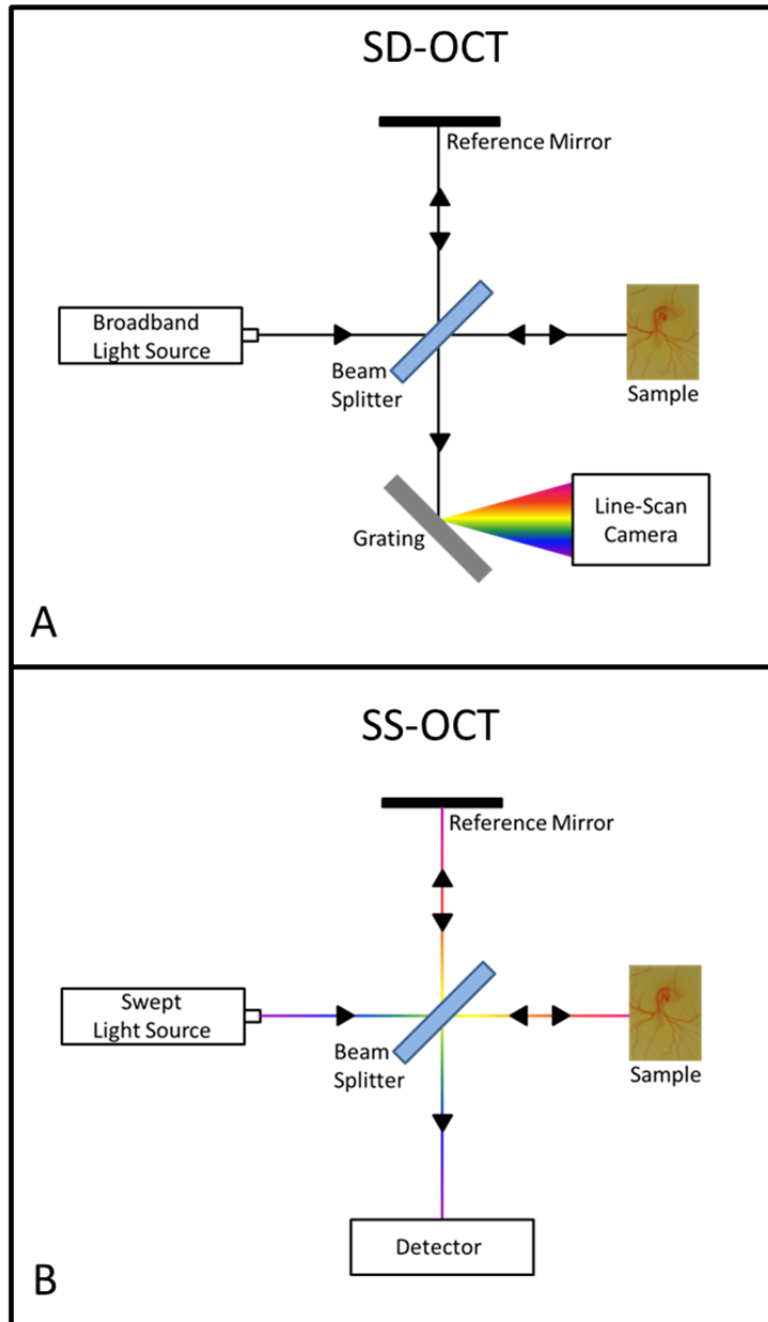
Figure 1.4: Fourier domain OCT system diagrams.

(A) In SD-OCT, a broadband light source is used and the detected light is dispersed along a high speed line scan camera. (B) In SS-OCT, a swept light source is used that outputs a narrow band of the spectrum over time as represented by the rainbow light paths. The reflected light is then detected by a photodetector. Both system setups have a stationary reference mirror.

1.7 Doppler OCT

In addition to structural imaging, OCT is capable of performing functional imaging to monitor and measuring moving reflectors in biological tissue. These functional images are generated by combining the Doppler effect with OCT. When light is backscattered from a particle that is moving axially the signal experiences a Doppler frequency shift. This Doppler shift can be expressed as:

$$f_D = \frac{2v_s \cos \theta}{\lambda_0} \tag{1.1}$$

where v_s is the velocity of the particle, θ is the angle between the velocity vector and the sample beam, and λ_0 is the central wavelength of the light source. In early TD-OCT systems, the Doppler shift was obtained through a spectrogram method [121, 122]. This involves using short time fast Fourier transformations (STFFT) to calculate the flow velocity. This method allowed for simultaneous imaging of *in vivo* structure and velocities; however it had limitations in velocity sensitivity. STFFT calculations of flow have the resolution limited by the window size of the Fourier transform. The minimal detectable frequency shift varied inversely with the window size. However, the spatial resolution is also proportional to the STFFT window size. Therefore there is a tradeoff between the velocity sensitivity and spatial resolution that makes imaging flow in small blood vessels challenging.

An alternative method involves determining the phase difference between sequential A-scans. This approach offers the advantage of decoupling spatial resolution and velocity sensitivity. At each position in depth, the phase difference

is calculated between two A-scans at each lateral position in the image. This results in the Doppler shift being expressed as

$$f_d = \frac{\Delta\varphi}{2\pi T} \tag{1.2}$$

which can be combined with equation 1.1 to express the velocity as

$$v_s = \frac{\lambda_0 \, \Delta\varphi}{4\pi T \cos\theta} \tag{1.3}$$

where $\Delta\varphi$ is the phase difference between subsequent A-scans and T is the time between the two scans. Doppler OCT was first demonstrated in TD-OCT systems [97, 123, 124] and has since been applied to FD-OCT systems as well. The minimal detectable velocity usually depends the phase sensitivity and on the scan rate parameters, which determine the time between subsequent scans. The maximal detectable velocity that can be unambiguously determined is when $\Delta\varphi$ is either $-\pi$ or π resulting in a maximum velocity of $v = \pm\lambda_0/4nT$. When $\Delta\varphi$ approaches π it becomes phase wrapped by -2π and the velocity appears to be moving in the opposite direction. In order to utilize this velocity information above π, groups have been working on phase unwrapping algorithms. By decreasing the speed between sequential A-scans, the maximum detectable velocity is increased. Unfortunately the minimal detectable velocity is also increased which may result in slow flow rates appearing invisible. This can be alleviated somewhat by measuring phase shifts from sequential B-scans as well as A-scans thereby generating two Doppler dynamic ranges [125].

The different FD-OCT system set-ups each have their own advantages and disadvantages of Doppler OCT. SD-OCT systems that make use of spectrometers suffer from fringe washout at higher velocities[126]. This results from phase shifts over the duration of a single A-scan and results in significant SNR degradation. SS-OCT systems acquire spectral channels in series which results in an effective higher spectral sampling rate minimizing fringe washout effects. However, SS-OCT systems suffer from worse phase stability. A variety of both hardware and software techniques have been developed to improve the phase stability of SS-OCT systems [127-129].

Due to the fact that Doppler OCT makes use of the Doppler effect for measuring flow, it is only able to perceive motion along the axial direction or in parallel with the imaging beam. Therefore if the velocity vector is at an angle with the imaging beam, Doppler OCT will only capture a component of the absolute velocity (Figure 1.5). The absolute velocity can be determined by using the following expression

$$V_{dopp} = V \cos \theta \qquad\qquad (1.4)$$

where V is the absolute velocity of the moving particle, V_{dopp} is the velocity component measured by the Doppler OCT, and θ is the angle between the velocity vector and the imaging beam.
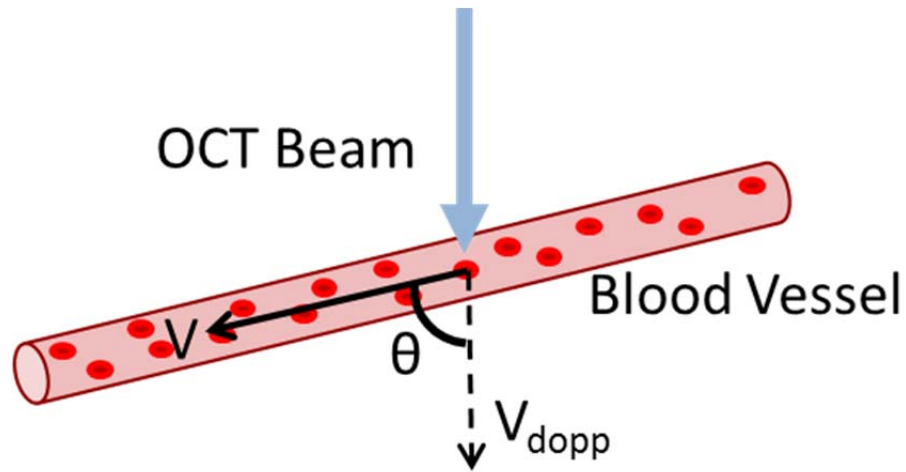
Figure 1.5: Doppler OCT angle dependence

Doppler OCT captures the component of velocity that is in parallel with the imaging beam. Additional information such as the angle of the velocity vector with the imaging beam is necessary to determine the absolute velocity.

Various methods have been developed to determine the additional information necessary for absolute velocity calculations. Firstly, the angle between the velocity vector and the imaging beam, also known as the Doppler angle, can be directly measured. This can be accomplished using OCT or any other imaging modality capable of 3-D volumetric imaging of the vessel orientation. A 3-D volume of the vessel is acquired and the Doppler angle is measured using the vessel's geometry [85, 130-134]. The vessel angle has also been determined by measuring the same vessel and two different lateral positions. This is easily done when imaging the vessels surrounding the optic nerve head by performing two circumpapillary scans and slightly different radii [135-137]. The two cross sections can then be used to determine the vessel orientation.

The absolute velocity vector can also be determined by interrogating the same location from multiple different angles. In order to completely determine the absolute velocity vector in 3-D, at least 3 different measurements are necessary [138, 139]. This can be accomplished by using three interferometers to image the same position. Another method for imaging the same position from multiple angles is polarization multiplexing [140, 141]. In this technique the light is split into different polarization states and then shown onto the sample at different angles. Finally delay encoding [86, 138, 142] can be utilized in which a refractive material is placed into the imaging beam to split it into different sub-beams that interrogate the sample at different angles. These techniques can be performed with only 2 imaging beams so long as the angle between the vessel and the imaging plane is known or aligned to zero.

Doppler OCT has been utilized extensively in embryonic imaging to monitor and measure various cardiac functions at different stages of development. Through the acquisition of multiple A-scans in a single position over time (M-scan), pulsed Doppler traces can be generated [132, 143]. This has been performed both directly in the developing heart as well as in other areas of the vasculature. The blood flow and blood velocities directly within the developing heart can be calculated at various stages of development [71, 72, 86, 132, 144]. Blood flow and velocity information obtained from Doppler OCT has also been used as input parameters for computational fluid dynamic modeling [145, 146] to assess wall shear stress in the developing heart. Other groups have taken this a step farther and used Doppler OCT to directly measure shear rate or shear

stress in the developing heart as well as the vasculature [71, 85, 132, 147]. Various strain measurements have also been made in the developing heart using Doppler OCT of the moving heart wall [144, 148].

1.8 Overview of Presented Work

In the work presented here, a variety of techniques were developed in order to measure cardiac function in the developing embryonic heart. These techniques include shear stress maps, absolute blood flow calculations, and contractile wave velocities.

Shear stress is a critical biomechanical force for the proper development of the heart. Previous techniques focused on determining the shear at orthogonal cross sectional slices or through computational fluid dynamic modeling. Here we developed and demonstrated a technique to measure the shear stress along the endocardial wall in 3-D over the duration of the heartbeat. 4-D (3-D volumes over time) shear stress maps enable comparisons of shear stress from very specific regions of interest in the endocardium with other points of interest on the same heart.

As discussed above, absolute blood flow calculations from Doppler OCT can be challenging due to the nature of the Doppler effect. Here we developed a dual beam delay encoded technique to measure the same location from two different angles. By aligning these beams perpendicular with the B-scan direction, the absolute flow in the vessel can be determined instantaneously without determination of vessel orientation. This enables rapid pulsatile flow measurements from individual B-scans.

Absolute blood flow and shear stress measurements were then performed in ethanol exposed embryos in which CHDs develop. Ethanol exposure has been shown to alter great vessel morphology in late stage hearts as well as have an influence on the hemodynamics at earlier stages of development. Here we measure the blood flow and shear stress in the developing aortic arches to help determine what role hemodynamics could be playing in these heart defects.

Finally, we developed a technique for measuring the contraction of the beating heart. Using a 4-D data set of the developing heart, we measured the cross sectional area at various orthogonal sections and measured the contraction wave velocity along the length of the heart tube. We then compared these measurements with conduction velocities obtained from optical mapping to better understand how conduction and contraction are related.

Chapter 2: 4-D Shear Stress Maps of the Developing Embryonic Heart

2.1 Introduction

Blood flow is a critical factor that regulates developmental programs during cardiogenesis. Alterations in blood flow during early cardiovascular development can lead to congenital heart defects (CHDs) [34, 36, 38]. Biomechanical forces exerted by the flow of blood likely influence molecular/gene expression in endothelial and support cells [46, 149-151]. The altered molecular/gene expression then affects the form and function of the developing heart resulting in further alterations to the biomechanical forces. Due to the absence of appropriate tools to sensitively assess forces on the early looping heart this biomechanical feedback is poorly understood. Even small alterations in the heart beat may influence blood flow that then results in altered levels and patterns of shear stress on the endocardium and potentially lead to abnormal heart looping, trabeculation, valvulogenesis and septation [32, 38].

One critical biomechanical factor caused by blood flow and involved in heart development is the shear stress experienced by the endocardium. Shear stress in the developing heart is the force that is exerted on the endocardial cells by the blood dragging past them. Shear stress has been shown to be of critical importance in both controlling and regulating various cellular processes involved in heart development (reviewed in [45, 149, 152]). Alterations in the hemodynamic patterns in the developing heart have been shown to result in major cardiovascular defects including septal defects and outflow tract anomalies [32-35]. This is due in part to the wide variety of signaling molecules whose expression and activity are influenced by alterations in shear stress. Some of

37

these proteins including KLF2, ET-1, NOS-3, and pERK which have all been shown to be influenced by shear stress and play a role in the developing avian cardiovascular system [38, 42-46]. In order to better understand the connection between mechanotransducing molecules, blood flow-induced shear stress, and heart development, it is important for us to be able to accurately measure shear stress on the endocardium.

The ability to accurately measure biomechanical forces in the looping embryonic heart is complicated by the diminutive size of the heart at this stage (< 2mm) and the rapidly changing blood flow patterns. High-frequency pulse-echo ultrasound is commonly used to image fetal mouse hearts and to assess their cardiac function [59, 153]. However, ultrasound imaging requires the transducer to be in acoustic contact with the sample and is not amenable to culture methods that maintain the early embryo *in vitro* under physiological conditions. Additionally, the resolution of ultrasound imaging is not sufficient to accurately measure developing hearts that are < 2mm in length. Previously, microparticle image velocimetry (μPIV) has been successfully used to estimate shear stress in the avian embryonic heart [54, 55]. Unfortunately, μPIV is a 2-D measurement and is unable to assess shear throughout the entire heart tube during cardiac looping. Optical coherence tomography (OCT) has shown great promise with regards to both structural and functional imaging of embryonic heart development [71, 72, 74, 82, 84, 88, 144, 154]. Van Leeuwen et al proposed a method to directly measure shear stress in vessels with resolution in depth using Doppler OCT [147]. Blood flow measurements and structural images acquired by OCT

have also been used as boundary conditions for modeling shear stress patterns in the avian heart tube [145, 146], and to measure the shear rate in chicken embryo vitelline vessels [71]. We have previously shown that by using Doppler OCT, shear stress can be measured at selected cross sections of the developing heart tube [132]. However, it is necessary to measure shear stress in 4-D (i.e. 3-D volumes in motion) in the developing heart tube, in order to thoroughly investigate the relationships between dynamic shear stress on the endocardium of the living, beating developing heart and molecular expression patterns regulating normal and defective developmental paths.

Here, we demonstrate a method based on 4-D Doppler OCT to directly measure the blood flow-induced shear stress on the endocardium of early avian embryonic hearts over the course of a full heart cycle. 4-D Doppler OCT image-sets of three individual embryonic hearts were acquired while they were incubated in an environmental chamber under physiological conditions [155, 156]. Using image-based retrospective gating [74, 75, 157] we obtained 4-D image data sets containing both structural and Doppler flow information. These data were used to create maps of shear stress on the endocardium at 14 time points during the cardiac cycle. This method for quantitatively mapping shear stress was verified using a capillary-tube flow phantom at multiple flow rates.

2.2 Material and methods

2.2.1 Embryo preparation

Fertilized quail eggs (Coturnix coturnix; Boyd's Bird Company, Inc. Pullman, WA.) were incubated in a humidified, forced draft incubator at 38°C (G.Q.F.

Manufacturing Co., Savannah, GA). After 48 hours of development the eggs were taken from the incubator, the eggshell was removed, and the contents were placed in a sterilized 35 mm Petri dish [10]. Once in the Petri dish, the surviving embryos were placed in an environmental OCT imaging chamber [158] with controlled temperature ($38^{o}C$) and humidity to ensure imaging under physiological conditions.

2.2.2 OCT imaging

The OCT system used to collect the data utilized a buffered Fourier Domain Mode Locked laser as previously described [82]. The in-depth and transverse resolution was 8 μm and 10 μm, respectively, in tissue. 4-D Doppler OCT data were collected by imaging over multiple heartbeats at sequential slice locations (Figure 2.1B-D) and reassembled using image-based retrospective gating [74]. 1000 A-scans were acquired per frame with a line rate of 117 KHz, and after reassembly a total of seventy volumes per heart beat were acquired. A-scans were recorded at 1.4 μm steps in the B-scan direction. Data were also acquired from a calibration interferometer and used to resample the data evenly in wavenumber and to improve the Doppler signal by correcting for laser phase noise[132]. For each B-scan Doppler image a five-line rolling average was employed to reduce phase noise and phase wrapping was corrected using a Goldstein algorithm [159].

2.2.3 Shear stress measurements

In order to calculate the shear stress in the developing heart tube three assumptions were made. First, it was assumed that the blood is a Newtonian

fluid with an approximate dynamic viscosity, η, of 5 mPa s [54, 132]. Second, it was assumed that the blood flow in the looping avian heart has both a low Reynolds number and a low Womersley number, indicating that the flow is laminar and dominated by viscous forces [54, 132]. Finally, it was assumed that the blood moves in the direction of the center line of the heart tube.

The shear stress, τ, was calculated using the equation $\tau = \eta\,du/dn$ [54] where u is the fluid velocity parallel to the wall and n is the radial distance from the surface of the tube. In order to find the velocity gradient normal to the wall (du/dn) the endocardium was manually segmented at 14 evenly spaced time points throughout the cardiac cycle from the 4-D OCT structural image data using image analysis software (Amira, Visage Imaging). The segmented endocardial surfaces were employed to determine the centerlines of the heart tube at each time point (Figure 2.2A). The centerlines were originally calculated within Amira using a TEASAR (tree-structure extraction algorithm for accurate and robust skeletons)[160] algorithm and then smoothed using custom analysis software (MATLAB, MathWorks). Assuming the blood is all moving in the direction of the center of the heart tube, tangent lines at each point along the centerline were calculated and then used to correct the Doppler OCT data to estimate the absolute blood velocity at each time point. The segmented endocardium was then used to generate an outer surface shell representing the endocardial wall on which the shear stress was calculated. The surface shell was a mesh composed of 4,000 connected triangular faces and the direction normal to each triangle was calculated (Figure 2.2B). This direction was used to determine the velocity

gradient from the endocardial wall, which was computed as the local slope of the velocity profile (within 45 μm of the endocardial wall). The shear stress values were then calculated by the formula above and plotted using a color scale on the corresponding surface mesh. Paired Student's *t*-tests (Excel, Microsoft) were performed on peak shear stress values in various regions, and statistical significance was achieved when $p<0.01$.

2.2.4 Phantom validation experiment

In order to verify the method of shear stress measurement, a capillary tube phantom was created to simulate the flow through the heart with a controlled velocity profile. The capillary tube had an inner diameter of 0.5 mm and was perfused with a 2% lipid suspension solution (Intralipid) solution using a syringe pump. 4-D Doppler OCT data were obtained at five different flow rates ranging from 0.25 ml/min to 2 ml/min. The syringe pump flow rates were calibrated by measuring the total volume of Intralipid solution pumped during a specific period of time using a graduated cylinder. At each flow rate, the Doppler data were then used to calculate wall shear stress at 7 cross-sectional slices utilizing the methods described above. The average shear rate on the inner wall of the capillary tube was then compared with the shear rate calculated using the known flow and tube geometry.

2.3 Results

For this demonstration, stage HH13 quail embryos (n=3) were cultured using a shell-less culture method and imaged using OCT as described in detail in the

Methods section. Stage HH13 embryos were selected because cardiac looping is occurring during this stage and these embryos exhibit dramatic morphological changes during this developmental time period. OCT not only allows clear observation of these morphological changes, but it is also capable of visualizing the internal anatomical structures of the developing avian heart in detail (Figure 2.1).
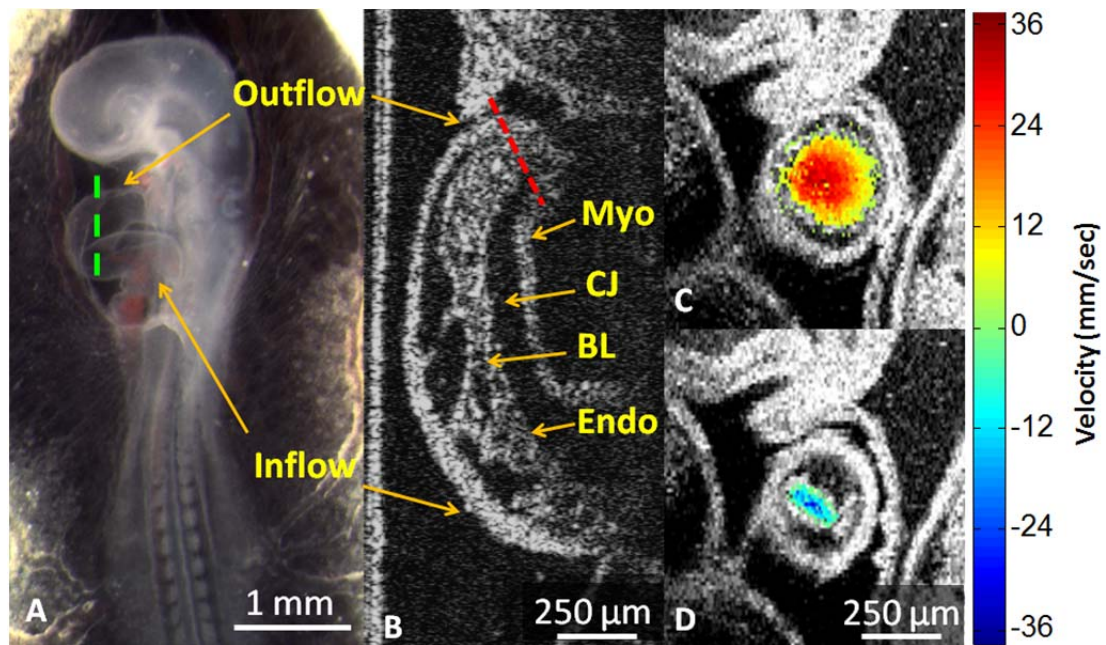
Figure 2.1: Representative quail embryo and OCT images

A shows a quail embryo imaged with a stereomicroscope at 12X magnification. This embryo was removed from the yolk and inverted using the New culture method for clear visualization under the microscope. All other embryos imaged by OCT in this work were left on the yolk as described in detail in the Methods section. Panel B shows a cross sectional image of the quail embryo heart imaged by OCT. The cross section was recorded at approximately the location of the green dotted line in panel A. Imaging by OCT allows for the visualization of the myocardium, cardiac jelly, and endocardium *in vivo* in both the inflow and outflow region of the heart tube. Panel C and D show Doppler OCT data overlaid on a structural cross section of the outflow tract of the heart

tube during diastole and systole respectively at the approximate location of the red dotted line in panel B. The increasing red color represents increasing blood velocity in the forward direction and the blue represents retrograde blood flow as represented by the color bar. Myo – myocardium, CJ – cardiac jelly, BL – blood, Endo – endocardium.

4-D Doppler OCT datasets were assembled as described in detail previously [132] and summarized in the Methods section. These image sets include both structural and Doppler flow velocity data, as shown in Figure 2.1. Extracting endocardial wall shear stress (WSS) from these data requires significant analysis. Under assumptions detailed above, the WSS is proportional to the blood velocity gradient in the direction normal to the wall of the endocardium, known as shear rate, and to the blood viscosity. Determining the shear rate at each point within the heart tube required: (a) the location of the entire surface of the endocardium, which was obtained by segmenting the structural OCT images, and (b) the blood velocity profile, which was obtained from Doppler OCT, corrected by assuming that the blood flows in the direction of the center line of the heart tube (Figure 2.2). Blood viscosity was assumed from previously published work [55].
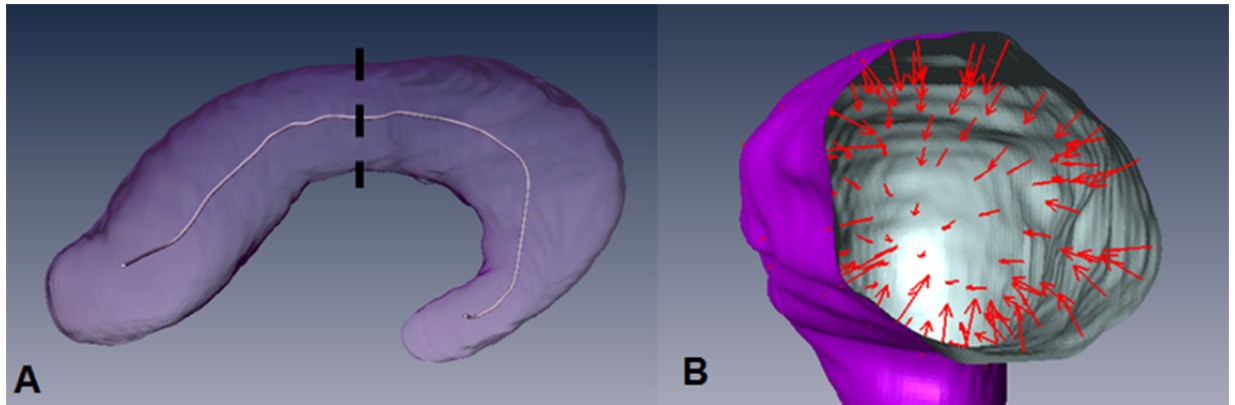
Figure 2.2: Steps in shear stress map generation

Panel A shows the centerline (white line) through the segmented endocardium of a representative heart tube during diastole. Tangents to the centerline were used to determine the Doppler angle for absolute velocity calculations.   Panel B shows the surface mesh of a representative segmented endocardium of a heart tube cut at the location of the dotted line in panel A. The red arrows pointed inward along the surface mesh represent the normal vectors to the endocardium along the entire inner wall of the heart tube.

Shear stress maps were calculated at 14 evenly-spaced time points during the cardiac cycle of each embryo. Examples of four time points from one embryo are displayed in Figure 2.3 (more data are shown in supplementary material S1). The shear maps show shear stress values as high as 7.7 Pa in the outflow segment of the heart tube compared with a maximum at the inflow segment of 3.1 Pa during the course of the heartbeat. Higher shear stress is also apparent on the inner curvature of the heart tube compared to the outer curvature (Figure 2.4). These observations were evident in all three heart tubes mapped.   A segment in the middle of the heart tube (marked in gray in Figure 2.3) was not analyzed because the blood flow in this area is nearly perpendicular to the OCT

imaging beam, leading to little or no Doppler signal. As a result, accurate blood velocity measurements were not obtained in this area. Currently, we are primarily interested in the AV junction and outflow segments of the heart because these are the location of future endocardial cushions and subsequent valve development, and because data from previous studies are available in these regions for verification [146]. However, by recording 4-D Doppler OCT image sets with the scanner oriented at different incidence angles, a complete flow map of the entire heart tube can be generated.
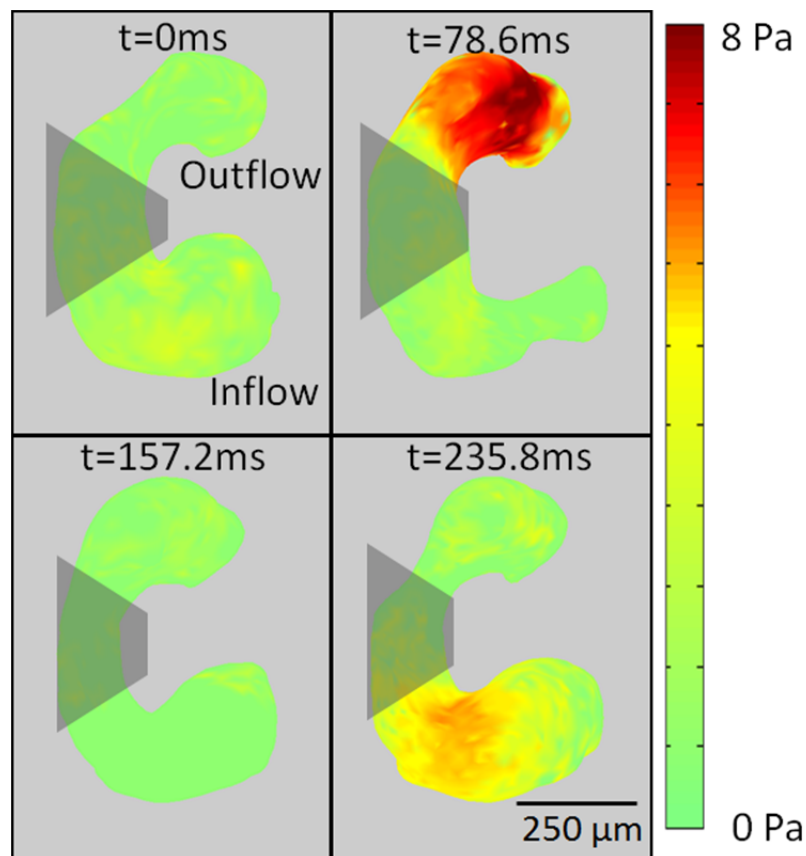
Figure 2.3: Shear stress on the endocardium.

Shear stress is calculated using the velocity gradient normal to the wall of the heart tube and the viscosity of blood. Four evenly spaced time points during a heart cycle are represented and the

shear stress values are displayed on the endocardium surface. The represented heart beat lasted 367ms. The gray region represents the area where valid Doppler OCT data were not obtained because the direction of the blood flow was nearly perpendicular to the OCT imaging beam.

4-D shear stress maps enable visualization of the shear stress patterns at specific areas of interest in the developing heart (Figure 2.4). 3-D maps representing each time point during the cardiac cycle may be examined from multiple orientations. In particular, the outflow tract of the heart tube was examined at the time of highest shear stress from various viewing angles (Figure 2.4B and C). Higher shear stress was consistently observed on the inner curvature of the outflow tract when compared with the outer curvature in all three hearts examined. This trend was also consistent over the course of the entire heart cycle.
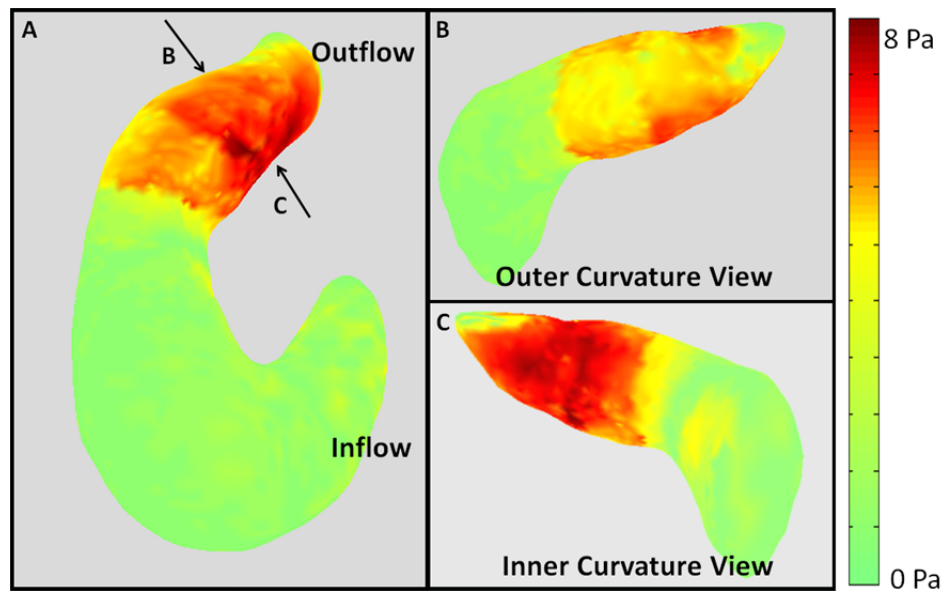
Figure 2.4: Shear stress on the inner and outer curvature of the outflow tract.

Panel A shows the 3-D shear stress map at the time of maximum shear stress in the outflow tract. Panel B and C show the shear stress map of the same heart cropped to show only the outflow tract. Panel B shows the shear stress map oriented to view the outer curvature of the heart tube and Panel C shows the shear stress map oriented to view the inner curvature of the heart. The viewing direction is represented in panel A by the two arrows.

In addition to 3-D spatial shear stress maps, this technology also provides temporal shear stress information as shown in Figure 2.5. Here, shear stress traces at three locations on the endocardial wall are shown over the full heart cycle. The shear stress traces clearly show significant differences in both the magnitude and the shape of the waveform depending on the location in the heart, with the inner curvature of the outflow tract displaying the highest peak shear stress values. At point A in Figure 2.5 (inner curvature) the maximum shear stress is approximately four times the peak shear stress at point B (outer curvature). Negative values of shear stress (e.g. Fig. 2.5A) indicate regurgitant flow, which is common in the outflow tract at this stage of development. The inflow trace (Figure 2.5C) shows a double peak pattern that is also observed in pulsed Doppler traces of the inflow tract and in the venous system in general. This trace shows less shear stress associated with the pumping phase of the heart cycle (the first peak), and higher shear stress associated with the filling phase (the second peak).
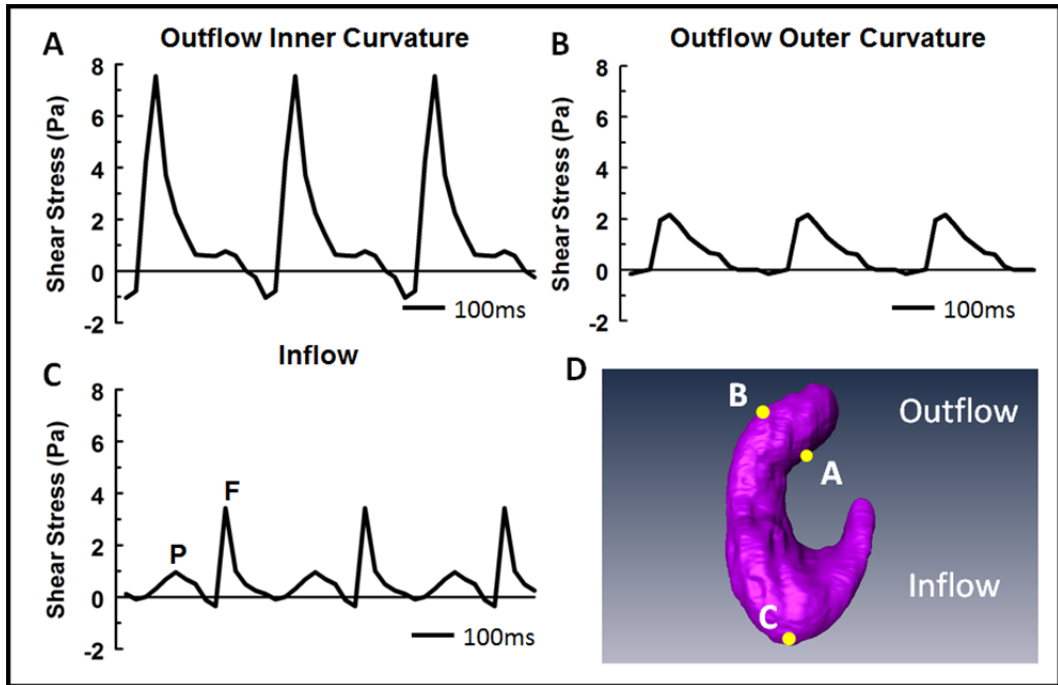
Figure 2.5: Shear stress measured over time.

Panels A-C shows the measured shear stress over time at three different locations in the same heart, namely the inner and outer curvatures of the outflow tract, and the inflow tract, respectively. The shear stress was calculated for the duration of one effective heart cycle and displayed three times for ready visualization. The locations represented by all three traces are indicated in the 3-D surface mesh shown in panel D. P – pumping phase, F- filling phase.

The maximum shear stress values in 3 different embryonic quail hearts at HH13 (Table 2.1) at the inflow tract and the inner and outer curvature of the outflow tract are shown in Table 2.1. The patterns of peak shear stress in all three embryos were found to be very similar. The average peak shear stress was found to be 7.7 Pa on the inner curvature of the outflow tract, 2.0 Pa on the outer curvature of the outflow tract, and 3.1 Pa on the inflow tract. The inner

curvature of the outflow exhibits significantly higher peak shear stress than the outer curvature (*p*=0.003) or the inflow (*p*=0.005).

Table 2.1: Maximal shear stress at the inflow and outflow regions of the heart (Pa)

	Max Inflow	Max Outflow IC	Max Outflow OC
Heart 1	3.0	7.4	2.0
Heart 2	3.1	8.1	1.6
Heart 3	3.4	7.6	2.5
Average ± S.D.	3.1 ± 0.1	7.7 ± 0.1	2.0 ± 0.2

IC – Inner Curvature, OC – Outer Curvature

In order to verify the accuracy of this new method of shear stress measurement, a phantom experiment was performed under known flow conditions. A syringe pump forced a 2% Intralipid solution through a straight capillary tube with an inner diameter of 0.5 mm. A segment of the tube was imaged by 3-D Doppler OCT at 5 different flow rates controlled by the syringe pump. At each of the 5 different flow rates, shear rate on the inner wall of the capillary tube was measured at seven locations on the tube. Because the flow was constant and the tube was straight, the shear rate on the tube wall was expected to be uniform, so that variability between the seven measurements would represent the measurement precision. The range of flow rates were selected to cover the range of shear rates experienced within the heart tube at this stage of development. The results are summarized in Figure 2.6. The dotted

line represents the peak shear stress value measured using this method in the embryonic heart tube. The solid line indicates the theoretical shear rate based on the flow values assuming a laminar flow profile. The measured values deviated from the theoretical value by an average of 2% across all flow rates. The precision of multiple measurements at each flow rate was 2% as estimated by relative standard deviation (the ratio of standard deviation to the mean). These results are reported in terms of shear rate rather than shear stress because shear rate is the fundamental measurement obtained from the Doppler OCT data. Viscosity is assumed to be a constant scaling factor, and the viscosity of Intralipid solution (~1mPa s) differs significantly from that of embryonic blood at this stage of development (~5mPa s).
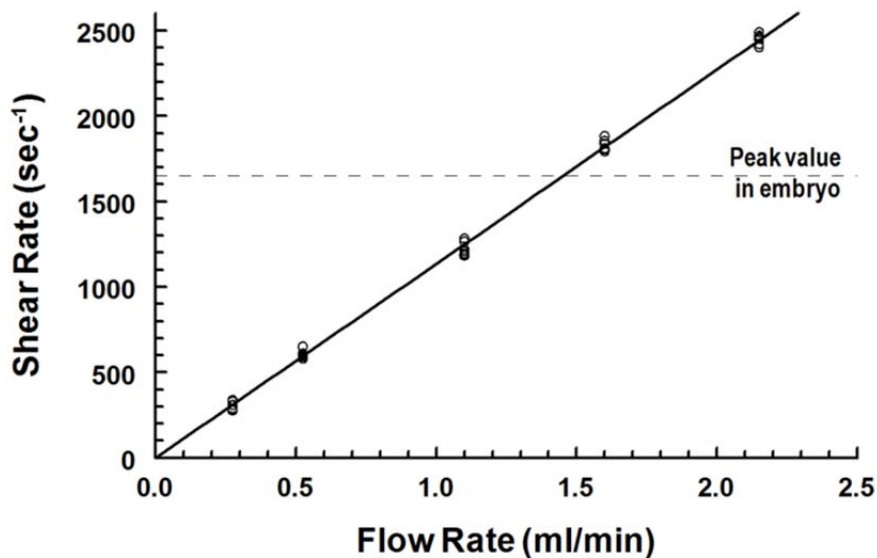
Figure 2.6: Shear rate measurement verification.

The x-axis represents the actual flow rate recorded from the syringe pump. The y-axis shows the shear rate values measured from the Doppler OCT data taken at each flow rate. These calculations were repeated for 7 experiments at each flow rate. The solid line represents the

theoretical shear rate based on the measured flow rates. The dotted line represents the peak shear stress value measured in the embryonic heart.

Shear stress maps can be utilized to better understand hemodynamic alterations resulting from perturbation experiments. One such perturbation that we have previously demonstrated is optical pacing (OP). We have shown that at low radiant exposures, OP is capable of reliably pacing embryonic quail hearts *in vivo* without detectable damage to the tissue [39]. Optical pacing was conducted utilizing an 1851 nm diode laser [39]. The light was delivered through a 400 μm multimode fiber and aimed at the inflow region of the heart tube using an aspheric lens which generated a spot size of ~ 400 μm on the tissue's surface. The heart was paced 50% above the intrinsic rate (4.5Hz) for the duration of the 4-D imaging session (~5min). Following cessation of optical pacing the heart returned to its natural heart rhythm. Figure 2.7 shows a view of a 3-D shear stress map of the outflow tract of a quail embryo heart both before (left) and during (right) optical pacing. The shear stress map shows the time points corresponding to the highest regurgitant flow. The shear stress map of the endocardium clearly shows stronger regurgitant flow over a more extensive region during OP compared to the heart beat during sinus rhythm. The maximum regurgitant shear stress was 3.9 Pa before OP and 7.7 Pa during OP.

Before Optical Pacing   **During Optical Pacing**
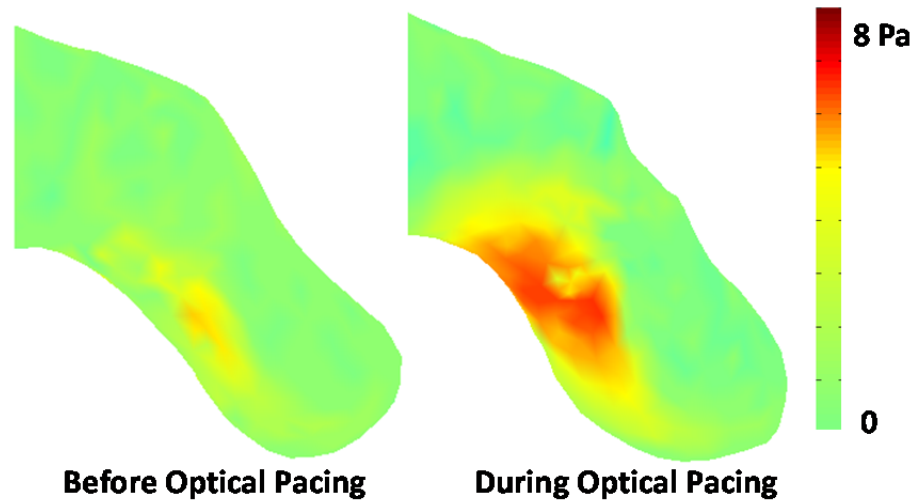
Figure 2.7: Shear stress in the outflow tract of an optically paced heart

3-D shear stress maps of the outflow tract of a stage 14 quail embryo heart before and during optical pacing. Both shear maps display the time point corresponding to the maximum regurgitant flow. The regurgitant flow during OP generates stronger shear stress at the endocardial wall. The maximum regurgitant shear stress before and during optical pacing was 3.9 Pa and 7.7 Pa respectively.

After calculating the shear stress at 14 time points in the cardiac cycle we calculated the oscillatory shear index (OSI) which is a measure of the variation of the instantaneous shear stress vector relative to the average direction over time. This measurement was accomplished by using nonrigid registration to match the points of the segmented surface mesh over the 14 time points. The OSI was then calculated as detailed in [161]. The OSI ranges from 0, if the shear is predominately in the same direction, to 0.5 if the average shear stress over time is zero. In Figure 2.8, OSI is calculated and mapped to a surface rendering of the outflow tract. OSI is significantly increased during OP. This is due to the increased regurgitant flow caused by pacing the heart well beyond its intrinsic

rate. Although regurgitant flow velocities were altered, forward flow remained similar before and during OP. The region of increased regurgitant shear stress and OSI corresponds to the site of future valve development [162]. Because regurgitant flow may facilitate valve development [38], OSI may be a very useful metric. In the future investigators can develop OP protocols to specifically alter OSI to varying degrees in the outflow tract to investigate the effects of regurgitant flow on valvulogenesis.
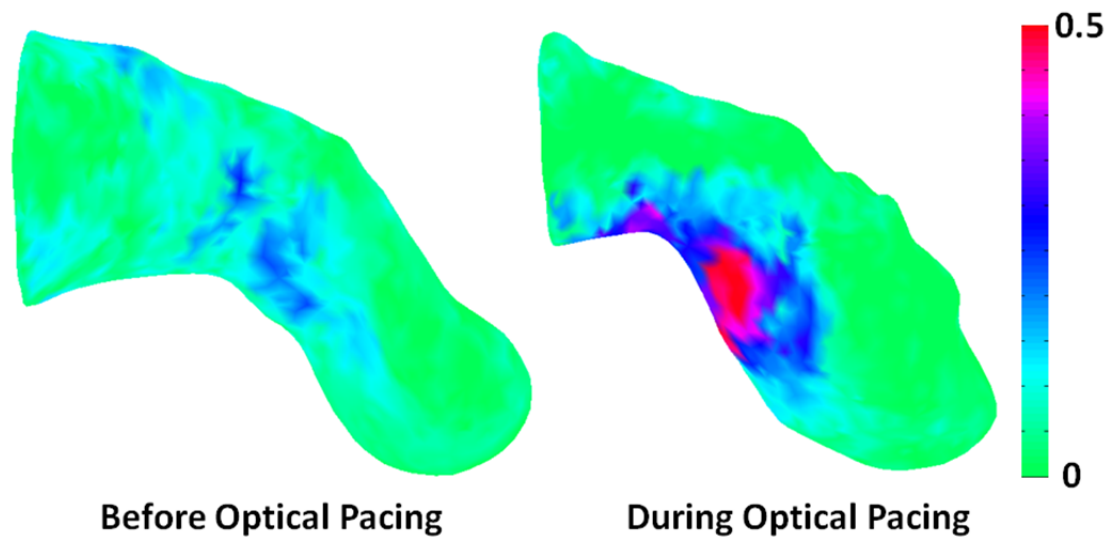
Figure 2.8: OSI of an optically paced heart

Oscillatory shear index (OSI) in the outflow tract of the heart before and during OP. The OSI was calculated over the course of an entire heart beat and displayed on the surface mesh of the segmented outflow tract.

2.4 Discussion

OCT derived 4-D maps allow direct measurement of the shear stress at any region of interest in the developing heart, which is a significant advance over previous 2-D measurement techniques. The shear stress values presented here

correspond well with those reported previously in specific regions of interest. The peak outer curvature shear stress values obtained by 4-D OCT (1.6-2.5 Pa) are similar to those reported by μPIV on the top surface of the outflow tract of a HH 17 stage chicken heart (1-3 Pa) [55]. Also, OCT shear stress values at the inner curvature (7.4-8.1 Pa) are similar to those estimated with finite element modeling of the outflow tract of a HH18 chick embryo (11 Pa) [146]. These associations are encouraging, but exact correspondence is not expected because of differences in animal models, developmental stages, and model preparation methods.

The shear stress measurements presented here made use of three assumptions that have the potential to introduce uncertainty in the shear stress values. One assumption is that of the blood viscosity at this stage of embryonic development. The value of 5mPa s has been used previous works [54, 132] for similarly staged embryos and we believe it to be a reasonable estimate. However, in this shear stress measurement, the viscosity merely serves as a scaling factor. Therefore, the comparisons between different regions of the heart are still valid regardless of the value of the blood viscosity. Another assumption is that the blood flow at this stage of embryonic heart development is dominated by viscous forces, which leads to laminar flow. Previous groups have shown the Reynolds number to be approximately 0.5 in similarly staged embryos which is well below the threshold needed for the development of turbulent flow (<1000-2000) [54]. Additionally, the Womersley number at this stage of development is on the order of 0.2 which allows for the safe assumption of a parabolic velocity

profile (<1-2), which is also observed in our OCT data [54, 153]. Finally, we assume that the blood is flowing in the direction of the heart tube's centerline. This is a reasonable assumption for the same reasons stated above. Were this not to be the case, it would influence our estimations for the absolute velocity of the blood at each cross sectional location. An error in the Doppler angle estimation would impart a proportional error in the absolute velocity measurements. Because such an error would be small, and would not change quickly, there is a potential to cause uncertainty in comparing measurements taken from regions of the heart tube that are far from each other (e.g. inflow tract and outflow tract), but it is unlikely to influence the comparison of measurements taken in close proximity to each other (e.g. inner curvature and outer curvature).

This work represents the first report of shear stress measured by the use of imaging in 3-D throughout the cardiac cycle. 4-D shear maps allowed comparison of shear values at one region of the endocardium to another region within the same heart. Higher shear stress was observed on the inner curvature in the outflow tract of the developing heart compared with the outer curvature. This trend corresponds well with previously reported results obtained through the use of modeling [146, 152] and μPIV measurements [55]. The higher shear stress values on the inner curvature in the outflow tract is interesting due to the fact that the outflow tract is where the future aortic and pulmonary valves and septae will develop [162]. It has also been shown that changes in flow and therefore shear stress may facilitate atrioventricular valve development [38]. 4-D shear mapping will be useful for future investigations of the relationship between

hemodynamics and valve development in specific areas of the developing heart tube.

4-D OCT shear mapping is expected to significantly benefit the investigation of early heart development, but some limitations remain that can be overcome in the future. One limitation is that there are manual processing steps necessary to analyze the image data sets including endocardium segmentation and phase unwrapping. This makes it time-consuming to process the results of experiments that involve a large number of embryos. Automated image processing algorithms are in development in order to enable high-throughput experiments using 4-D data sets from larger numbers of embryos, particularly automated segmentation of the endocardium boundary. A limitation of the presented imaging protocol is that Doppler OCT signal is not obtained from the center of the heart tube. This is due to the fact that the blood flow in this segment is nearly perpendicular to the OCT imaging beam. This limitation can be overcome simply by recording an additional 4-D image set with a different angle of incidence. Multi-beam Doppler OCT methods have also been demonstrated that can image from multiple orientations simultaneously [141, 142].

The combination of Doppler OCT-derived shear stress and molecular staining will enable new investigations to better understand the role of shear stress in the development of the heart tube. Doppler OCT allows analysis of shear stress at each moment during the cardiac cycle. These measurements will allow for the precise localization of highest shear stress both spatially and temporally without relying on modeling. We have demonstrated that Doppler OCT can be used to

monitor the change of shear stress over time and the data obtained can also be analyzed to determine metrics such as the oscillatory shear index (OSI) at specific locations within the heart tube. Abnormal OSI has been shown to have a close correlation with abnormal valve formation in zebrafish [38]. This metric could prove interesting and valuable for investigations of the effects of changes of regurgitant flow on the development of the heart. We have shown that optical pacing can be utilized to precisely perturb the heart rate and thus the hemodynamic forces in the developing heart. The resulting altered hemodynamic forces are difficult to model, however direct imaging with Doppler OCT enables straightforward analysis. In the future, these measurements could be correlated with expression levels shear stress responsive markers to gain a better understanding of exactly which cells are most affected by the altered shear stress. Together these complementary tools may prove to be powerful for future investigations into the role of shear stress in signaling the development of the heart.

Chapter 3: Orientation Independent Absolute Flow Measurements using Dual Beam Delay Encoding

3.1 Introduction

Blood flow is a critical factor that regulates developmental programs during cardiogenesis. During early embryonic development, deviations from the normal blood flow pattern have been shown to lead to congenital heart defects including septal defects and outflow tract anomalies [32-36]. Blood flow and its resulting hemodynamic forces may alter molecular/gene expression in the surrounding cells and thereby influence developing cardiovascular form and function [38, 46, 149-151]. To better understand the role flow plays during cardiovascular development precise tools are needed to rapidly calculate and monitor blood flow.

Volumetric flow rate in a vessel can be defined as the volume of blood that passes a given cross section of that vessel per unit time. The flow rate can be calculated if the cross sectional area of the vessel of interest and the absolute velocity vector everywhere on cross section are known. In cultured avian embryos, which are useful models of heart development that we use routinely [82, 85, 132, 158], vessel cross sectional area is easily measured using optical coherence tomography (OCT) imaging [163]. At the same time, Doppler OCT (DOCT) can provide depth-resolved velocity information with high spatial resolution [121, 122, 164, 165]. DOCT has been used to measure blood velocity and the resulting hemodynamic forces on the vessel wall [71, 85, 132, 144], as well as to estimate total flow [134, 166]. However, DOCT is only sensitive to motion parallel to the imaging beam, so additional information is needed to obtain

the absolute velocity vector in order to calculate absolute flow. This additional information has required volumetric imaging or increased system complexity.

Two major strategies have been employed to overcome this limitation and obtain the absolute velocity vector. One method is to determine the vessel orientation as an estimate of the Doppler angle and use it to correct the measured velocity. The Doppler angle (α) is the angle between the imaging beam and the absolute velocity vector of the blood (Figure 3.2c). If it is assumed that the flow is parallel with the vessel's orientation, the direction of the velocity vector can be estimated by acquiring a 3-D structural OCT volume of the vessel and measuring the vessel orientation [130, 131]. However, the orientation can sometimes be difficult to determine in smaller blood vessels that are usually more tortuous and with borders that are difficult to discern. Around the optic nerve head, the vessel angle has been estimated by recording two concentric circumpapillary scans at slightly different radii and using the two corresponding cross sections of each vessel to determine the vessel orientation [135-137]. This method is faster than acquiring a 3-D volume, but is also more susceptible to error in estimating the vessel orientation. An error in estimating the flow direction leads to an error in the corresponding velocity and flow measurement, which becomes particularly significant when the OCT beam is nearly perpendicular to the flow (Figure 3.1).
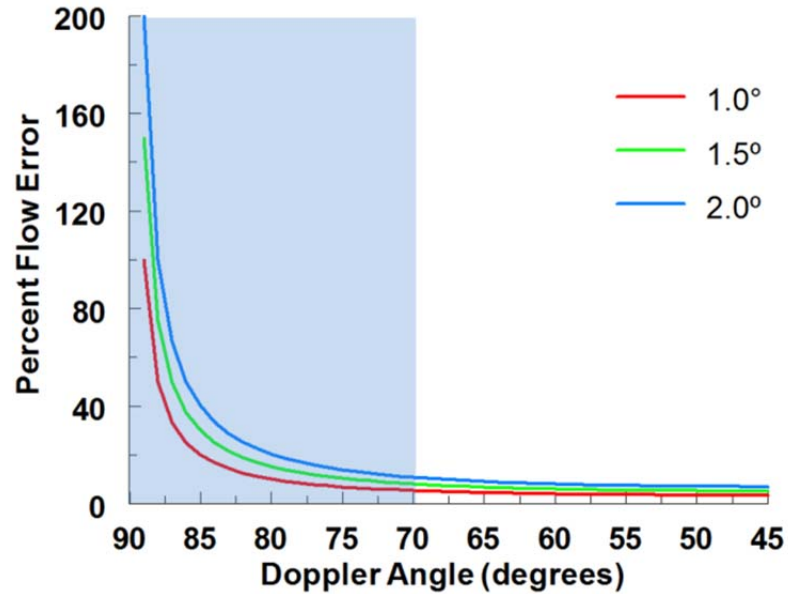
Figure 3.1: Theoretical error from inaccurate vessel angle estimation

Theoretical flow percentage error from vessel angle estimation inaccuracies as a function of Doppler angle. The typical inter-user variability we observe when measuring vessel orientation in 3D volumes is around 1.0° which can result in flow error greater than 20% when the Doppler angle is at 85°. The blue box represents the typical vessel angles for the quail embryonic vascular network.

Alternatively, the absolute velocity vector can be determined by imaging the same location using multiple imaging beams at different angles of incidence [91, 138, 140-142, 167]. This has been accomplished by utilizing polarization multiplexing [140, 141], delay multiplexing [138, 142], and through the use of additional OCT interferometers [91, 167]. To completely determine the velocity vector with no additional information, at least three different measurements are necessary [138]. This can not be done with polarization multiplexing, requires significant range for delay encoding, and increases system and alignment

complexity when adding OCT interferometer channels. The velocity vector can be calculated using only two imaging beams if the angle between the vessel and the incident plane supported by the two illumination beams is aligned to zero, or is known or measured [141, 167].

Recently it has been recognized that flow can be calculated with no knowledge of the orientation of the vessel or absolute velocity vectors. This calculation only requires measurement of the velocity components normal to the imaging plane. To satisfy this condition a 3-D volume of the vessel is acquired with DOCT and the flow is calculated from an *en face* section, which is naturally perpendicular to the acquired velocities and illumination beam [132, 163, 166, 168, 169]. The flow calculation does not suffer from the angle error described previously because vessel orientation is not needed. However, acquiring a 3-D volume can be time consuming, so measuring pulsatile flow using this technique would require either gating data over several heart cycles [74, 169, 170] or imaging a small enough region of interest to acquire volumes in real time [163].

To enable pulsatile flow calculations without the need for 3-D volume acquisition we have extended the *en face* cross section method to the B-scan plane. To measure velocity perpendicular to the B-scan plane with a minimally-modified OCT instrument, we generate imaging beams at two different effective incidence angles using delay encoding [142]. The beams are precisely aligned so that the plane of the two angled beams is perpendicular to the B-scan direction. The perpendicular velocities can then be calculated over the cross sectional area to determine the flow. With this technique, flow rates can be calculated from

individual B-scan images which allows for the measurement of pulsatile flows with high temporal resolution throughout the heart cycle.

To validate this technique, a capillary tube flow phantom was imaged at various orientations and at various flow rates provided by a syringe pump. The technique was validated for *in vivo* blood flow measurement by imaging quail embryo yolk sac vessels. The measurements were compared with the conventional 3-D technique. Vessels were measured at separated positions to determine the consistency of the measurement along the vessel length. Bifurcated vessels were also imaged before and after the bifurcation to confirm that the two smaller measured flow rates equaled the parent vessel's flow rate.

3.2 Methods

3.2.1 Velocity Measurement by Delay Encoding

Flow (F) in a vessel may be calculated from a single cross-sectional B-scan as the product of the pixel area (ΔS) and the sum of the velocity perpendicular to the imaging plane (V_{trans}) at each pixel in the cross-section area S, as

$$F = \Delta S \sum_{S} V_{trans} \ .$$
(3.1)

To determine V_{trans}, at least two Doppler measurements must be taken at different angles of incidence and the plane of those two vectors should be orthogonal to the B-scan imaging plane. To accomplish this, we used a delay-encoded method that we have previously demonstrated [142]. This method requires only a single OCT channel (i.e. one interferometer and detector) and is readily implemented by

adding a single optical element to an OCT scanner. Briefly, a glass plate was placed to half-intersect the imaging beam in the OCT scanner before the scanning elements and objective lens as illustrated in Figure 3.2a (for simplicity, the scanning elements are not depicted in the figure). The separation angle 2θ between the two beams is determined by $2\theta = 2\arctan\left(r_o \, / \, f\sqrt{\pi}\right)$ [142] where r_o is the 1/e radius of the Gaussian beam and f is the focal length of the lens (Figure 3.2c). In this work, the total angle difference 2θ was measured as 8.4 degrees in air and 6.1 degrees in tissue. The introduction of the glass divides the imaging beam into two components with one half of the light delayed. This results in the generation of 3 delay-encoded images as shown in Figure 3.2b from the 4 different paths the light can take. The top image (AA) results from light taking path A twice, which experiences no optical delay. The bottom image (BB) results from light taking path B twice and being optically delayed twice. The middle image (AB/BA) results from light taking either path A forward and path B back or vice versa, and thus being delayed once. The glass is inserted into the imaging beam so that the plane formed by the two components is perpendicular to the B-scan direction. The orientation of the two planes can be verified by ensuring that the three generated images are aligned vertically with one another (Figure 3.2b). The three images result from beams with different effective angles of incidence on the sample which therefore experience different Doppler shifts when imaging flow, as is evident in the three Doppler OCT images in Figure 3.2b. The information in the two images AA and BB is sufficient to determine the transverse velocities.
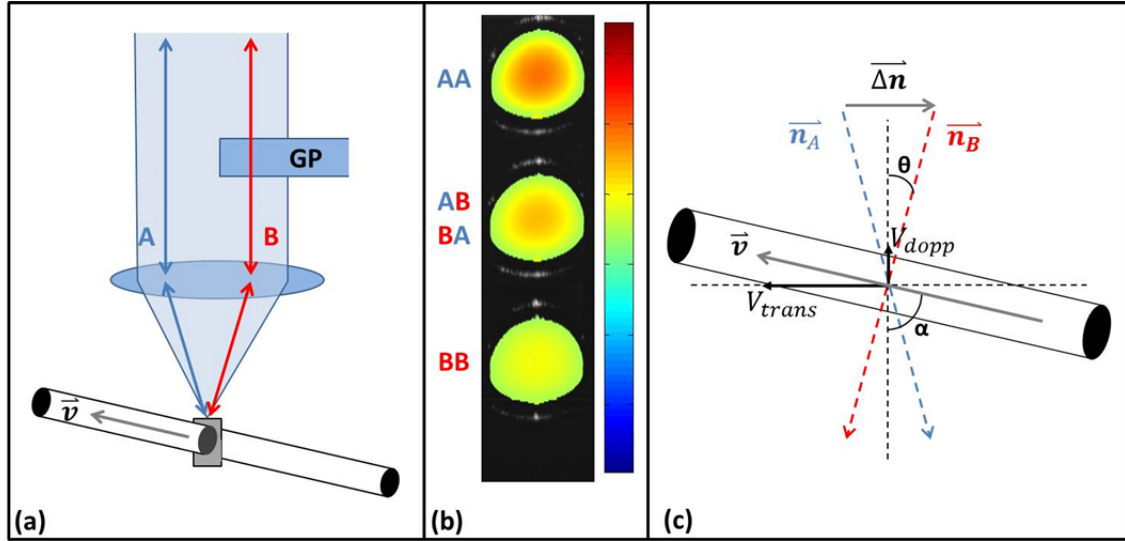
Figure 3.2: Principle of operation

(a) A glass plate (GP) was introduced into the imaging beam and the resulting two imaging sub-beams (A, B) are incident on a capillary tube. (b) OCT Doppler overlay image generated from the plane cross-sectioning the capillary tube showing the three sub-images (AA, BB, AB/BA) generated from the two delay-encoded sub-beam paths (A, B). The illuminating sub-beams have different effective angles of incidence resulting in different Doppler images. (c) Diagram defining the vectors, angles and velocities used for absolute flow calculation (see description in text).

3.2.2 Calculation of Absolute Flow

When velocity components measured in image AA are subtracted from velocity components measured in image BB, the common axial velocity component is eliminated, leaving only the velocity components perpendicular to the B-scan plane. Referring to Figure 3.2c,

$$V_A = \vec{v} \cdot \overrightarrow{n_A} \quad , \text{ and } \quad V_B = \vec{v} \cdot \overrightarrow{n_B} , \text{ so} \qquad (3.2)(3.3)$$

$$V_A - V_B = \vec{v} \cdot \left(\overrightarrow{n_A} - \overrightarrow{n_B} \right) = \vec{v} \cdot \overrightarrow{\Delta n} , \text{ or} \qquad (3.4)$$

66

$$V_A - V_B = V_{trans} \cdot 2\sin(\theta) ,$$ (3.5)

where V_A represents a velocity measured in image AA and V_B represents a velocity measured in image BB. The calculated transverse velocity values can then be input to Eq. (3.1) to determine the flow. In practice, the cross-section areas in image AA and image BB (S_A and S_B respectively) do not correspond pixel-by-pixel, so one may integrate the velocity profiles before calculating the velocity difference:

$$F = \frac{\Delta S}{2\sin(\theta)} \sum_S (V_A - V_B) \simeq \frac{\Delta S}{2\sin(\theta)} \left(\sum_{S_A} V_A - \sum_{S_B} V_B \right) .$$ (3.6)

This straightforward analysis assumes that the two image slices are interrogating the identical cross-section, i.e. $S_A = S_B$. However, due to the angular separation between the two beams this is never quite the case. This discrepancy results in two potential problems: that the cross sectional areas S_A and S_B are different, and that the two slices are not necessarily interrogating exactly the same locations in the vessel. The effect of this error on the flow measurement was examined by computer-simulation (Matlab). Flow velocity data in a cylindrical channel with a perfect parabolic flow profile was generated, and then artificially sectioned at two different angles of incidence. The Doppler velocities in the two cross sections were found, simulating the physical two-beam imaging measurement, and the flow was calculated based on Eq. (3.6). This simulation was repeated at various angles of orientation between the flow and the image planes, from -30° to 30°. The results of the simulation are represented as the solid line in Figure 3.3a and show an overestimation in the flow as the angle

increases. Furthermore, the overestimation is independent of beam separation angle θ, and of the diameter of the flow channel.

We investigated two methods for compensating for the flow error caused by the difference between the two cross-sections.

3.2.2.1 Method 1

The first method is to use the difference between the mean velocities in the two cross-sections to obtain the mean transverse velocity $\overline{V_{trans}}$. Then, $\overline{V_{trans}}$ can be multiplied by the "true" cross-section area, S, which we obtain from image AB/BA. This effectively projects the velocity components measured at the two angles onto a single cross-section, which is orthogonal to the calculated transverse velocity, and eliminates the inaccuracies that result from the differences in cross sectional area between the two slices. Under the assumptions that all flow in the tube is in the same direction, and that the tube is rigid within the sampling region, the flow equation can be rewritten as:

$$F = \Delta S \sum_S V_{trans} = S \cdot \overline{V_{trans}} = \frac{S}{2\sin(\theta)}\left(\overline{V_A} - \overline{V_B}\right) \tag{3.7}$$

where $\overline{V_{trans}}$ is the average perpendicular velocity over the cross-section area, S, and $\overline{V_A}$ and $\overline{V_B}$ are the mean velocities in the two cross sectional areas S_A and S_B. In case of other two beam methods that do not produce this middle image, the average of the two images' cross sectional area could be used instead, which is only slightly less accurate.

68

3.2.2.2 Method 2

Calculating the mean velocity over a cross-section requires dividing by the cross-section area, estimated by segmentation. This step is prone to error. Therefore, we decided to approach the flow measurement from a different direction which does not assume the two slices are interrogating identical points, and does not require dividing by an estimated area. The transverse velocity (V_{trans}) is readily obtained from the measured Doppler velocity (V_{dopp}) when the Doppler angle α is known (Figure 3.2c). Under the assumption that the flow in the tube is all in the same direction, at angle α, Eq. (3.1) can then be rewritten as:

$$F = \Delta S \cdot \sum_S V_{trans} = \Delta S \cdot \tan \alpha \cdot \sum_S V_{dopp} \qquad (3.8)$$

For each of the two beams generated by delay encoding, the flow rate at each cross section can be expressed:

$$F_A = \Delta S \cdot \tan(\alpha + \theta) \cdot \sum_{S_A} V_A \text{ , and } \quad F_B = \Delta S \cdot \tan(\alpha - \theta) \cdot \sum_{S_B} V_B . \qquad (3.9)(3.10)$$

Therefore, $\quad \tan(\alpha + \theta) = \dfrac{F_A}{\Delta S \cdot \sum_{S_A} V_A}$, and $\quad \tan(\alpha - \theta) = \dfrac{F_B}{\Delta S \cdot \sum_{S_B} V_B} \qquad (3.11)(3.12)$

Under the assumption that the portion of the vessel being imaged is rigid the total flow across these planes will be equal to one another ($F = F_A = F_B$) so that Eq. (3.11) and (3.12) can be rearranged to eliminate α using the identity:

$$\tan(2\theta) = \frac{\tan(\alpha + \theta) - \tan(\alpha - \theta)}{1 + \tan(\alpha + \theta)\tan(\alpha - \theta)} = \frac{\dfrac{F}{\Delta S \cdot \sum_{S_A} V_A} - \dfrac{F}{\Delta S \cdot \sum_{S_B} V_B}}{1 + \dfrac{F}{\Delta S \cdot \sum_{S_A} V_A} \cdot \dfrac{F}{\Delta S \cdot \sum_{S_B} V_B}} . \qquad (3.13)$$

Solving for F results in a quadratic equation

$$F^2 + \left(\frac{\Delta S \cdot \sum_{S_A} V_A - \Delta S \cdot \sum_{S_B} V_B}{\tan(2\theta)} \right) F + \left(\Delta S \cdot \sum_{S_A} V_A \right) \cdot \left(\Delta S \cdot \sum_{S_B} V_B \right) = 0 . \qquad (3.14)$$

Solving this equation enables determination of the flow without any prior knowledge of the Doppler angle α and does not require dividing by an estimated cross-section area. Eq. (3.14) will result in the two solutions

$$F = \frac{-B \pm \sqrt{B^2 - 4C}}{2} \qquad (3.15)$$

where $B = \left(\dfrac{\Delta S \cdot \sum_{S_A} V_A - \Delta S \cdot \sum_{S_B} V_B}{\tan(2\theta)} \right)$ and $C = \left(\Delta S \cdot \sum_{S_A} V_A \right) \cdot \left(\Delta S \cdot \sum_{S_B} V_B \right)$. $\qquad$ (3.16)(3.17)

However, in most applications, where the vessels are oriented nearly perpendicular to the imaging beam, it is simple to determine the correct solution by choosing the one corresponding to the larger angle α. In situations where the correct angle is ambiguous (α ~ 45°) method 1 could be used, or the correct solution could be determined from *a priori* information.

3.2.3 Data acquisition and processing

The 2.5mm glass plate was inserted into a quasi-telecentric OCT scanner [171] in a Fourier domain OCT system[172]. A superluminescent diode centered at 1310nm with a FWHM of 75nm was used as the light source. A linear-in-wavenumber spectrometer [172] was used to project interference fringes onto a 1024-pixel InGaAs line-scan camera with a line rate of approximately 47 kHz. The system has an axial and lateral resolution of ~10 μm in tissue, depth range of 4.3 mm in air, and a roll-off of 6dB over 1.7 mm[172]. Doppler shifts were

calculated from phase differences between subsequent A-scans and a mean filter was applied in the complex domain to reduce noise.

3.2.4 Validation experiments

To compare the analysis methods over various Doppler angles, a capillary tube flow phantom with an outer diameter of 0.4 mm and an inner diameter of 0.3 mm was perfused with a 2% lipid suspension solution (Intralipid, Clayton, NC) using a syringe pump (NE-300 from New Era Pump Systems, Inc, Farmingdale NY) and imaged using the OCT system described above. The syringe pump perfused the tube at a constant flow rate of 0.83 µL/sec and B-scan images were acquired at various Doppler angles. For convenience, we plot by polar angle (90−α). The experimental results were furthermore compared with simulated results which were generated as described above. After comparing analysis methods, method 2 was selected for further experimental validation. The technique was validated using the capillary phantom and *in vivo*.

Using the capillary and pump system described above, the absolute flow was measured at various flow rates set by the syringe pump ranging from 0.04 µL/sec to 1.50 µL/sec. Next, the capillary tube was rotated to various azimuthal and polar angles to verify that the flow rate measurement was orientation-independent. At each position, a 3-D structural image set was obtained in order to validate the capillary tube's orientation.

To validate the technique for measuring blood flow *in vivo*, stage HH18 quail embryos' yolk blood vessels were also imaged to measure absolute flow at a variety of locations in the vascular network. These vessels were chosen because

they all reside on the surface of the yolk sac with no moving tissue underneath and hence we were able to avoid any potential tissue overlap between the three images. Embryos were cultured using a shell-less culture method and placed in an environmental OCT imaging chamber with controlled temperature (38°C) and humidity to reproduce physiological conditions [158]. 714 B-scan images were acquired over the duration of approximately 8 seconds or approximately 30 heartbeats. Vessels were imaged at two different positions along their length to determine whether the flow measurement was consistent over the entire vessel. 3-D structural volumes were also acquired to compare the new absolute flow measurement technique to the traditional flow measurement, correction by measuring the vessel orientation using the 3-D image. Finally, vessels were imaged before and after bifurcations to verify that the combined smaller vessels' flow after bifurcation equaled the parent vessel's flow. For each vessel measurement, heart rates were roughly calculated using the FFT of the pulsatile flow measurement. The average flow was calculated over the course of the full 30 heart beats.

3.3 Results

To compare the accuracy of the methods presented here, simulated data were generated at various polar angles and the values were input to Eq. (3.6), Eq. (3.7), and Eq. (3.15). These simulated results were then confirmed by imaging a capillary tube phantom with a constant flow rate at various polar angles. Flow rates were calculated from the phantom measurements using all methods and

plotted together with the simulation results. As shown in Figure 3.3a, the straightforward analysis using Eq. (3.6) is accurate near α =90, but significantly overestimates the flow as the angle deviates from perpendicular. Methods 1 and 2 consistently measure the correct flow without bias, with method 1 and 2 deviating from the actual flow rate by an average of 6.4% and 2.7% respectively. Having determined that analysis method 2 results in a more precise measurement, the balance of the validation experiments were analyzed using this method.
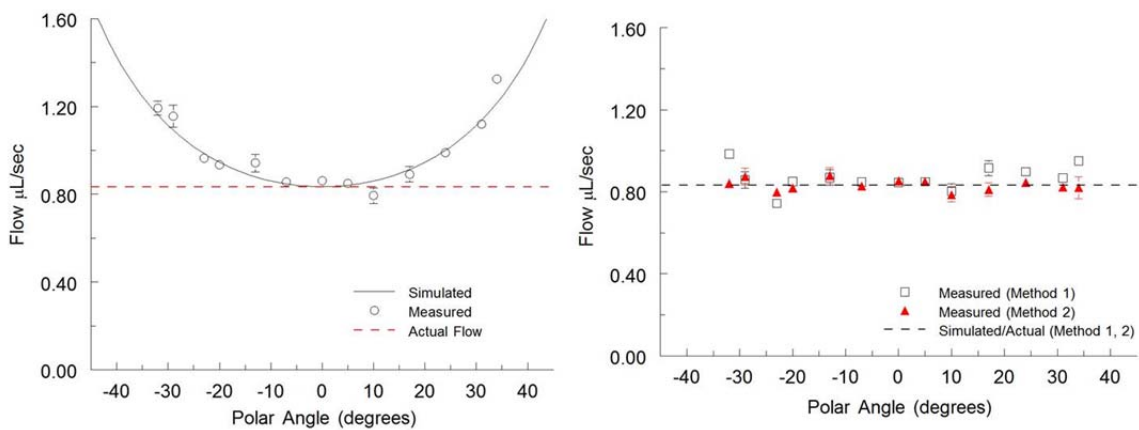
Figure 3.3: Simulated and measured flow rates versus varying polar angles.

A syringe pump perfused the capillary tube at a constant flow rate of 0.83uL/sec represented by the dotted line in both panels. (a)This graph shows the flow rates calculated from the straightforward analysis utilizing Eq. (3.6) plotted as circles. The measured flow rates show a trend of increasing overestimation at larger polar angles due to the difference in the two cross sectional area sizes. The results generated from the simulated data are represented by the solid black line. (b) This graph shows the consistent flow rates calculated using methods 1 and 2 showing unbiased flow measurement at all angles measured. The measured flow rates are plotted at squares and triangles for method 1 and 2 respectively. Both methods show they are not

influenced by the differences in cross sectional area sizes at larger polar angles. The simulated data are identical to the constant flow rate line so they are both represented by a single black dotted line. All measured flow rates are represented as mean ± S.D. over 80 imaging frames.

The capillary tube flow phantom experiment for various flow rates was repeated three times and the means and standard deviations were obtained from the combined results (Figure 3.4a). The linear fit to the data had a slope of 1.001 and a y-intercept of 0.008 indicating that the OCT measurements are consistent with flow rates set by the syringe pump. The measured flow rates varied from the actual flow rates by an average of 3.1%. The capillary tube phantom was then imaged under a constant flow rate of 0.83µL/sec at various azimuthal and polar angles of the tube. For each of these experiments, the angle was confirmed by obtaining a 3-D structural volume of the capillary tube at each position. The means and standard deviations of these experiments are shown in Figure 3.4b-c. Both sets of data generate a trendline with negligible slope (<0.0001) and y-intercept of approximately 0.83 indicating a consistent flow measurement of 0.83µL/sec over the range of angles measured. The measured flow rates varied from the actual rate by an average of 1.7% and 2.4% for the azimuthal data sets and polar data sets respectively.
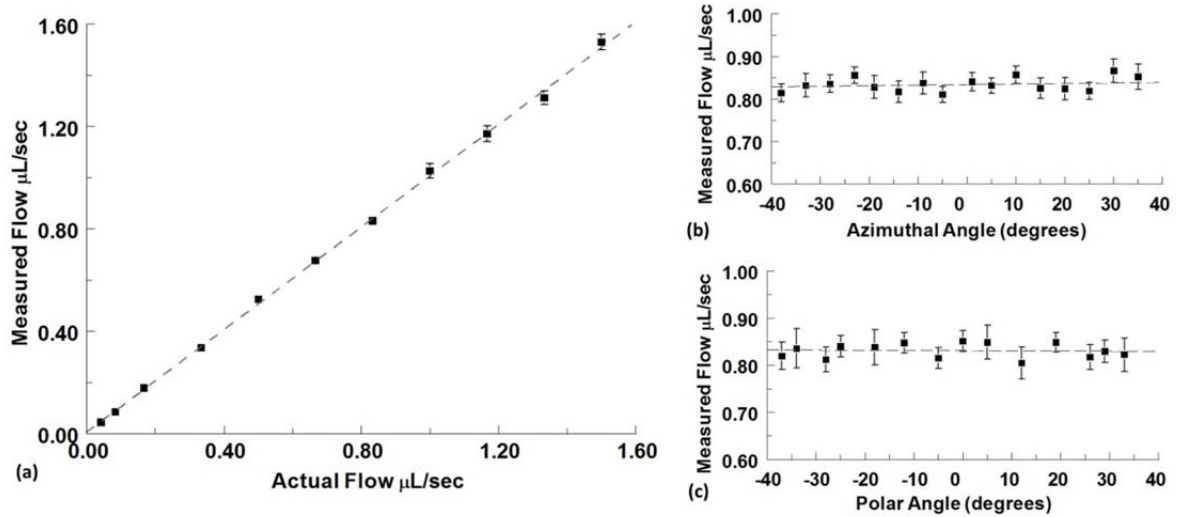
Figure 3.4: Phantom flow rate measurements

(a) Measured absolute flow in a capillary tube plotted versus actual syringe pump flow rates. Flow rates are represented as mean ± S.D. using the combined results from three independent experiments with 80 imaging frames at each angle. (b) Constant absolute flow measured at different azimuthal angle orientations of the capillary tube phantom at a polar angle of 3°. (c) Constant absolute flow measured at different polar angle orientations of the capillary tube phantom at an azimuthal angle of 5° (the actual syringe pump flow rate is set at 0.83 µl/sec for both angle variation experiments). Flow rates are represented as mean ± S.D. over 80 imaging frames.

To validate the technique for measuring blood flow *in vivo*, yolk sac blood vessels from 9 quail embryos at the cardiac looping stage (Figure 3.5a) were imaged and the time-averaged flow rates were calculated over 30 heart beats using analysis method 2. These measurements were compared with those obtained by the conventional technique of compensation by measuring vessel orientation from 3-D image volumes. 15 vessels were measured and compared using a scatter plot and a linear regression analysis was performed resulting in a

slope of 0.98 (95% confidence intervals 0.92-1.05, R^2=0.989) (Figure 3.5c). The majority of the Doppler angles of the selected vessels were around 10-15 degrees so when measured using the conventional 3-D method they did not suffer significantly from the uncertainties described in Figure 3.1, so that they could be used as the gold standard for comparison.

Next, 11 embryonic vessels were imaged before and after bifurcations as shown in Figure 3.5b. The sum of the time-averaged flow in the two branch vessels (e.g. position B and C) were plotted against the time-averaged flow in the parent vessel (position A) resulting in a slope of 1.00 (95% confidence intervals 0.96-1.04, R^2=0.997) (Figure 3.5d). Fifteen vessels were imaged at two different positions along their length to determine if the time-averaged flow measurement was consistent at different vessel positions and orientations (e.g. Figure 3.5b, position B and B'). The linear regression of the comparison resulted in a slope of 0.94 (95% confidence intervals 0.86-1.02, R^2=0.985) (Figure 3.5e). The variance observed in these three experiments can be explained by small biological variability, such as heart rate, during the imaging session. In addition to determining the average flow rate, the pulsatile flow rate profile can be obtained with high temporal resolution across the duration of multiple heart beats (Figure 3.5f). Due to the fact that only a single B-scan is needed to measure the flow, the instantaneous flow rate can be determined at any point during the heart cycle allowing for the observation of systolic and diastolic dynamics without the need for real-time volumetric imaging.
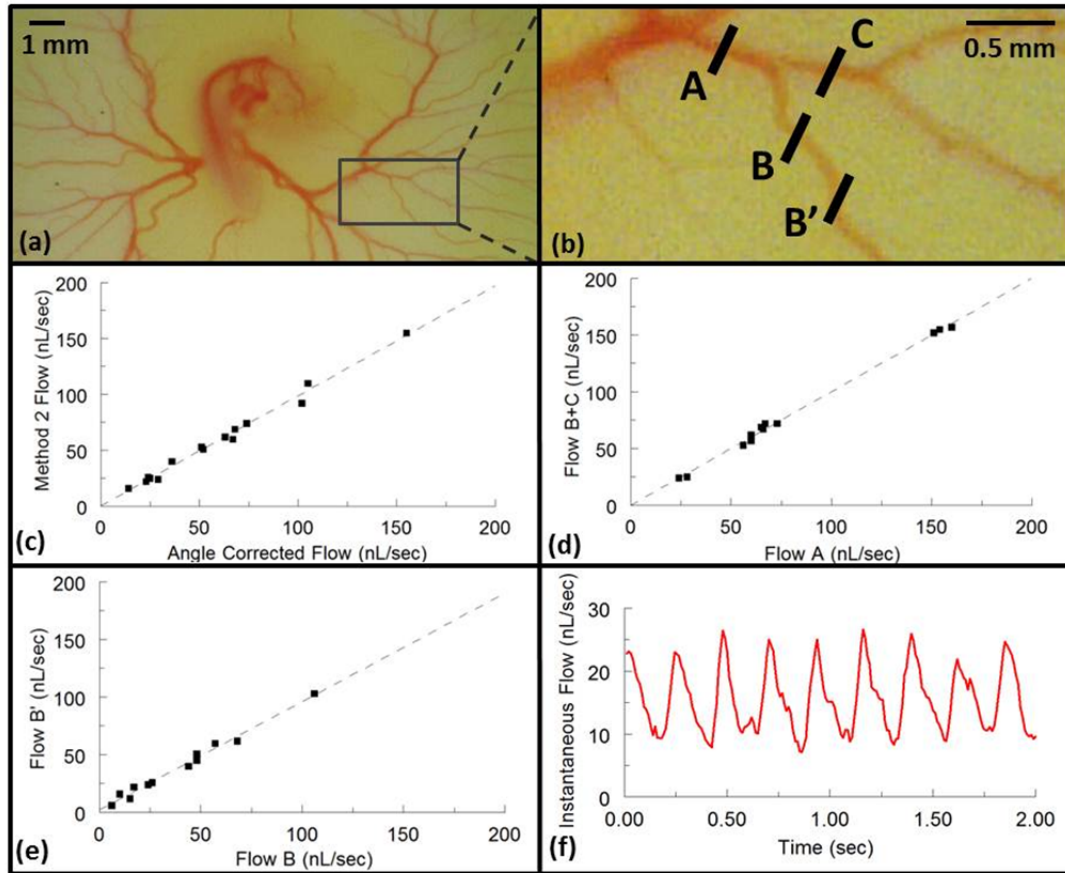
Figure 3.5: Embryonic flow rate measurements

(a) A representative stage HH18 quail embryo in shell-less culture was removed from the incubator and photographed with a microscope (Dino-Lite, AnMo Electronics Corporation, Torrance, CA) for documentation purposes. (b) Enlarged image marked by a box in (a) of representative imaged vessels. B-scan OCT images were obtained and the resulting data processed to calculate flow using analysis method 2 and by correcting for the Doppler angle measured via 3-D structural volumes for the same cross section. The resulting time-averaged flows are plotted against each other in panel c. B-scan OCT images were also obtained at A, B, and C to measure the time-averaged absolute flow before and after bifurcations. The corresponding flows are shown in panel d. Finally, vessels were imaged at two different positions (B and B') to confirm consistent time-averaged flow measurements at different vessel positions and orientations. The resulting flows are represented in panel e. (f) A representative pulsatile flow rate is plotted over 8 heart cycles.

3.4 Discussion

To generate two beams at different angles of incidence we utilized delay encoding. Delay encoding is a simple technique that can be applied to almost any free-space OCT scanner with little difficulty, simply by adding one optical element. This technique also ensures the two sub-beams are perfectly aligned at the focus, greatly simplifying alignment compared to other dual-beam approaches. However, this method does have some potential draw backs, one of which is ensuring that the OCT system has enough axial imaging range to be capable of capturing all three images simultaneously. The pathlength delay caused by a glass plate of thickness D and index n produces the three images spaced by a distance $D(n-1)/2$. This limitation becomes more serious if a vascular network over a range of depth is imaged, requiring longer separation between sub-images. The insertion of the glass plate could potentially generate a dispersion mismatch between the three sub-beams. However, the OCT system used did not have an exceptionally wide bandwidth and by our observation, the dispersion of the glass did not significantly influence the three images. Another limitation of delay encoding is the loss of sensitivity. The light is being broken into four different paths. The top and bottom satellite images, as shown in Figure 3.2b, are each resulting from 25% of the original incident light, while the center image results from 50% of the incident light. Less light results in less sensitivity and less depth penetration for each slice. This could be compensated by increasing the total light, however for some applications, such as retinal imaging, maximum exposure limits cannot be exceeded. Alternatively, other techniques

which generate two imaging beams simultaneously could be used to calculate flow with less loss of light (50% instead of 25%). The analysis presented here could readily be applied to any technique that generates two properly-aligned illumination beams. It should be noted that even low-SNR OCT images can provide reasonably strong Doppler OCT signals, so this is not a strong limitation. Decreased SNR will increase phase noise which may decrease the precision of the flow measurements at larger angles where the phase difference becomes smaller, but this should not introduce bias, affecting accuracy.

Two methods for calculating instantaneous flow rates were presented here. The straightforward analysis expressed in equation 3.6 assumes a pixel by pixel correspondence of the two acquired images. However, this relies on the assumption that the two cross sectional images are interrogating exactly the same slice of the vessel, which is not true because of the angular separation between the probe beams. Two potential problems arise from this difference. The first is that the cross sectional area of the two slices can be different sizes. Secondly, the locations being interrogated are not necessarily identical between the two slices. The error these differences introduce is negligible at small Doppler angles, but quickly causes large overestimations of flow at larger angles as shown in Figure 3.3a. In addition, simulation results indicate that this overestimation is independent of the beam separation or the size of the vessel, therefore reducing the dual beam angle separation or imaging smaller vessels will not solve the problem.

The first way we overcame this error (Method 1) was to compensate for the influence of the different cross sectional areas on the flow by finding the mean velocities and projecting them onto a single cross-sectional area. This method assumes that the flow in the tube is in a single direction and that the tube is rigid. This method proved to be accurate over a wide range of Doppler angles in the flow phantom, and it may work reasonable well even when these conditions are not strictly met.

Although method 1 was shown to be accurate and reasonably precise, its reliance on the mean velocity is susceptible to segmentation errors, which decreases its precision (6.4% error in the phantom) compared with method 2 (2.7% error in the phantom). It can be seen in Figure 3.3b that the error in method 1 is higher than method 2, and the errors are worse at higher angles. A small change the apparent area of either cross section, as measured by segmentation, will directly influence the mean velocities $\overline{V_A}$ and $\overline{V_B}$. Since the mean velocities are already close to one another, small errors will strongly propagate to the final flow calculation. For example, under a typical polar angle of 20°, a small segmentation inaccuracy around the vessel border (1% size change of the segmented area) can result in a 3.2% error in flow measurement. This inaccuracy increases with higher polar angles such that at an angle of 40 degrees the flow measurement could have an estimated error of up to 7.4%. This susceptibility to segmentation errors could become problematic for biological applications where the vessel boundary is more difficult to discern, and therefore difficult to measure by automated segmentation.

Method 2 approaches the flow measurement from a different direction. It does not require the assumption that the two measured images interrogate the identical slice, nor does it involve dividing by a measured cross-section area. This analysis is equally accurate as the other method and is very resistant to segmentation errors and therefore was used for the majority of validation work presented here. With method 2, a 1% area segmentation inaccuracy only results in a 0.1% error in the flow calculation. This resistance to segmentation errors originates from method 2 utilizing the summed velocities to determine the flow rather than the mean velocity. Segmentation errors tend to occur at the boundary of the vessel affecting the pixels with the smallest velocities. This segmentation error therefore has minimum impact on the summed velocities. The resistance of analysis method 2 to segmentation errors may allow the use of less computationally expensive segmentation approaches.

The primary limitation of method 2 is that is generates two solutions for a given measurement. For most cases it is straightforward to determine which of the solutions represents the correct flow measurement. The two flow rate solutions each also have an associated Doppler angle solution, and the two angles sum to 90°. Most applications of OCT blood flow imaging involve imaging vascular networks near tissue surfaces, which are nearly perpendicular to the imaging beam. Therefore, the solution with the larger angle will nearly always be the correct one. When the vessel being imaged approaches 45°, the two solutions and angles become very close to each other to the point that it becomes difficult to determine the correct one. In these cases, method 2 could

be used to determine the flow, or *a priori* information may be obtainable to resolve the ambiguity. Occasionally, at angles near 45°, the solutions can be complex values due to noise in the measurements. This is due to the fact that when the two solutions are close to one another, the discriminant becomes very small, and therefore more susceptible to noise. In these rare occurrences we found that using the real component of the complex solution was a reasonable estimate.

Both methods rely on the assumptions that the vessel is rigid and that flow in the vessel is in one direction. The rigidity assumption guarantees that the flow is constant across both imaging planes, and the single-direction assumption is implicit when velocities are averaged in method 1, and is assumed in the formulation of method 2. However, these assumptions cannot always be met in biological applications where vessels can be tortuous. In these situations, the parallel assumption will be violated and will result in a small error for both methods. Using our simulated data, under a typical Doppler angle with a 3cm radius of curvature, the error resulting from the curvature is usually no more than 2% for both methods. The solution to minimize such errors is to keep the vessel of interest at the focus, thus minimizing the physical separation of the two imaging planes and the curvature between the two planes. The assumption that the vessel is rigid is generally valid on the time-scale and spatial scale of OCT imaging.

An additional assumption for the method presented here is that the plane formed by the two imaging beams is orthogonal to the B-scan direction. This

orientation can easily be ensured by adjusting the position of the glass plate in the imaging beam when raster scanning patterns are used. Alternative scanning patterns such as circular or helical scanning are more challenging to ensure the two planes remain orthogonal to one another. A potential solution could involve rotating the glass within the sample arm in synchronization with the rotation of the B-scan, as has been previously demonstrated with a rotational Dove prism[167].

The method presented here relies on accurate calculation of the transverse velocity by the difference of two slightly angled Doppler images. This difference decreases with both increasing polar and azimuthal angles. The increasing angle results in a larger cross sectional area of the vessel, and therefore requiring a larger field of view. Additionally, the decreasing difference between the two Doppler images brings the value closer to the phase noise at higher angles. At larger polar angles where these issues become problematic, the original *en-face* method[168] would be a valid alternative for the determination of absolute flow. At larger azimuthal angles if the difference between the two sub-images approaches the phase noise, the scanning direction can be rotated 90 degrees to eliminate this problem.

Recently, Blatter *et al* have independently demonstrated an angle-independent method for measurement of absolute flow in retinal blood vessels using a very similar dual-angle Doppler OCT system[173]. That approach made use of two parallel beams that are focused on the same spot on the retina with a known angular separation, and are interrogated by two parallel interferometers.

These two interferometers generate two separate images with different Doppler shifts that are used to calculate flow using a method equivalent to what we described here as method 1. The measurements were validated by use of a capillary tube phantom perfused at a constant flow rate by a syringe pump. The velocity and flow were measured at various capillary tube orientations demonstrating the angle independence of the measurements. Measurements of velocity and flow were also demonstrated *in vivo* by measuring blood flow in a retinal artery. The measurements were averaged over one cardiac cycle and resulted in consistent flow measurements at various locations along the length of the artery at different vessel orientations. The technology presented by Blatter *et al* is very similar to the technology presented here, and results in an equivalent measurement. Both studies found the measurements to be valid and repeatable and provide strong support for the feasibility of orientation-independent measurement of absolute flow in small vessels using dual-angle Doppler OCT systems.

While this work made use of a spectral-domain OCT (SDOCT) system, the technique is equally applicable to swept-source (SSOCT) or time-domain OCT (TDOCT). In fact SSOCT and TDOCT are less limited by the significant axial range needed for delay encoding. The instrument used in this work was configured such that the sub-image separation distance was 0.625 mm. While sufficient for some applications, other target tissues may require a longer separation. In any particular case, the axial range of the OCT system must be long enough to accommodate the three sub-images. If the third sub-image is

attenuated significantly by roll-off, then the phase noise will not be the same as the first sub-image. Additionally, in the case of inadequate separation distances, the static tissue from one of the three sub-images may overlap with the vessel cross section of another sub-image. Both the attenuation caused by the roll-off and the image overlap would be expected to increase noise, but not necessarily to bias the velocity or flow measurement. The technique is also not limited by choice of Doppler OCT processing algorithm. Any method that produces an accurate estimation of Doppler shift is sufficient.

The results of the validation experiments indicate that our proposed technique of orientation-independent absolute blood flow measurement using dual-angle Doppler OCT is accurate and robust. The measurement errors determined by the phantom experiments are very low compared to biological variability, so the technique is very applicable to *in vivo* experimentation. *In vivo* validation results indicate that accurate absolute flow can be obtained rapidly from single B-scans of microvasculature, including flow pulsatility. This technique will enable us to objectively assay hemodynamics in experimental models of congenital heart disease. Measurement of flow rates with high temporal resolution over multiple heartbeats will allow for the examination of beat to beat differences that may result from arrhythmias.

The technology presented here could also be applied to OCT imaging of retinal vasculature. OCT is already an important clinical tool for diagnosing retinal disease [174, 175]. Decreased retinal and choroidal blood flow has been shown to correlate with age related macular degeneration [176-178]. Glaucoma and

diabetic macular edema have been shown to correlate with alterations to blood flow as well [179-182]. Incorporation of the flow measurement technique described here will allow for more precise real-time measurement of retinal blood flow.

In conclusion, we have demonstrated a Doppler OCT technique for absolute blood flow measurement that eliminates the need for volumetric data acquisition or vessel angle knowledge, allowing for rapid flow measurements from single B-scans. The rapid nature of this technique allows for visualization and measurement of pulsatile flow throughout the heart beat without the need for gating techniques or real-time volumetric imaging. The rapid nature and relative ease of implementation of the technique presented here may prove to be a powerful tool for future investigations of the role of blood flow in a variety of vascular models.

Chapter 4: Blood Flow and Shear Stress in the Developing Aortic Arches of Ethanol Exposed Embryos

4.1 Introduction

A recent survey of 345,076 women in the United States found that 7.6% of pregnant women admitted to alcohol use and 1.4% admitted to binge drinking [183]. This survey also found that 15% of nonpregnant women admitted to binge drinking. Since the average pregnancy is not recognized until 5 to 6 weeks after conception [184], a woman who binge drinks could unknowingly expose her embryo to high blood alcohol concentrations before pregnancy is usually detected. Even low levels of prenatal alcohol (ethanol) exposure, such as in a single dose, can produce birth defects termed fetal alcohol syndrome (FAS). The estimated cost to society for the care of children and adults with FAS in the US ranges from 1.4 billion to 9.7 billion dollars [185]. In addition to the craniofacial and neurological abnormalities normally associated with FAS, epidemiological studies suggest that 54% of live-born children with FAS present with cardiac anomalies [23], including valvuloseptal defects, stenosis of the pulmonary artery, Tetralogy of Fallot, and d-transposition of the great arteries [24]. Alcohol-induced congenital heart defects (CHDs) are frequently among the most life threatening and require surgical correction in the newborn. The mechanisms of these alcohol-induced CHDs remain largely unclear.

A significant portion of CHDs associated with fetal alcohol syndrome include defects in the great vessels of the developed heart [186, 187]. These defects include Tetralogy of Fallot, d-transposition of great arteries, persistent truncus arteriosus (PTA), and interrupted aortic arch [186]. We have observed similar phenotypes in our avian ethanol model, such as misplacement of the great

vessels, reduced cross sectional lumen area (Figure 4.1), or in some extreme cases vessels being absent from the level where they would normally be connected (Figure 4.2). During development, the great vessels evolve from six major pairs of aortic arches (numbered I-VI) which sequentially emerge and are selectively and differentially reduced and remodeled. Three of the original six pairs persist to form the brachiocephalic arteries (AA III), the pulmonary arteries (AA VI), and a segment of the aortic arch (AA IV). This sequence of growth, regression, and remodeling events are very sensitive and are vulnerable to perturbations that may result in congenital heart defects
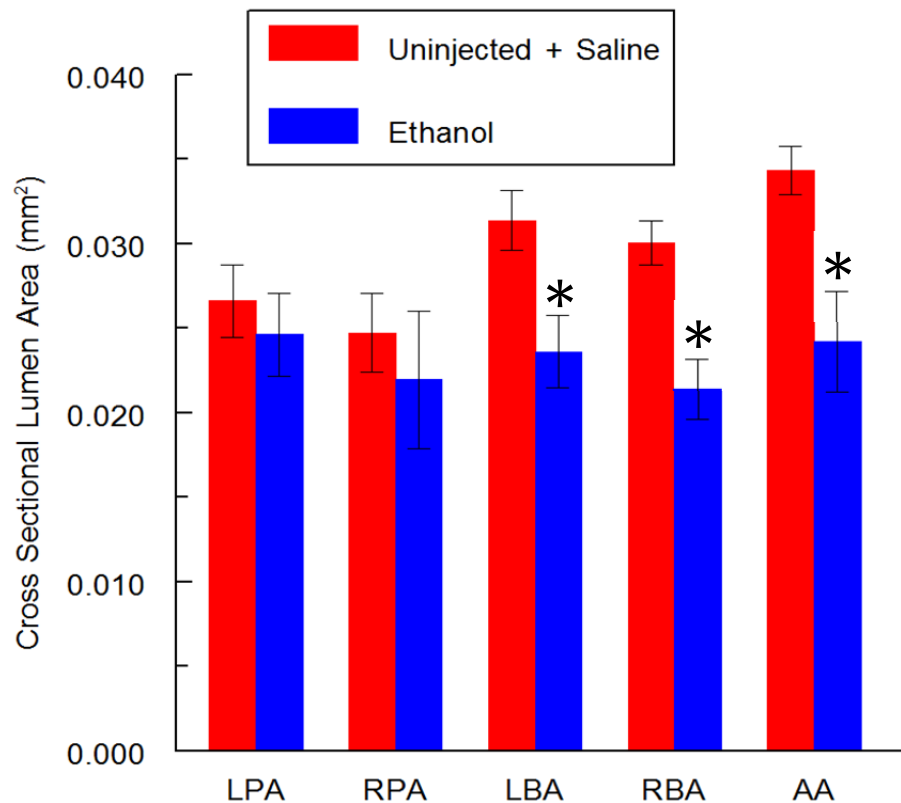
Figure 4.1: Lumen area measurements

Cross sectional lumen areas of the different great vessels in control and ethanol-exposed HH stage 34 embryos. The five great vessels were imaged with OCT (LPA-left pulmonary artery,

RPA-right pulmonary artery, LBA-left brachiocephalic artery, RBA-right brachiocephalic artery, AA-arch of the aorta). Reduced lumen areas were measured in the LBA, RBA, and AA in ethanol exposed embryos compared with the combination of saline and uninjected embryos. There was no statistical difference observed in the LPA and RPA. $*p < 0.05$. The bars represent standard errors.
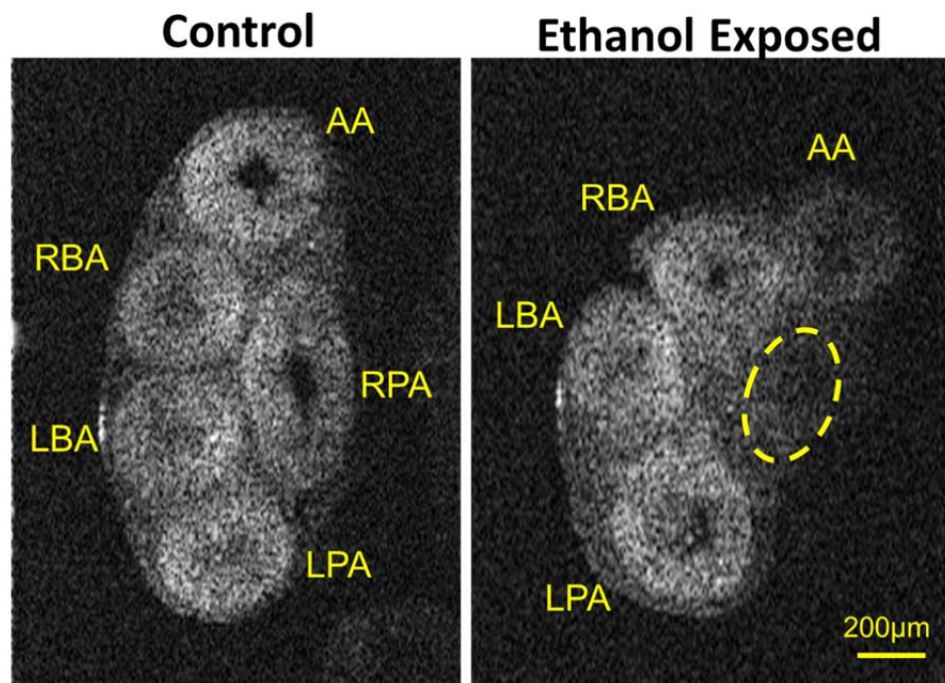
Figure 4.2: Morphology of great vessels

Cross sectional slices through a 3D OCT image of a HH stage 34 heart showing the great vessels of a control and ethanol-exposed embryo. The cross sectional image shows the right brachiocephalic (RBA), left brachiocephalic (LBA), right pulmonary artery (RPA), left pulmonary artery (LPA), and the arch of the aorta (AA). The ethanol-exposed embryo cross section reveals the absence of the RPA. The dotted circle shows where the vessel should be located.

Hemodynamic forces are known to play a significant role in the dynamic process of aortic arch formation and remodeling. Unfortunately, the exact

mechanisms at work in both normal as well as abnormal development of these vessels are poorly understood. Alterations to blood flow have been shown to result in congenital arterial defects such as coarctation of the aorta, interruption of the aortic arch, and double aortic arches [32]. We hypothesize that the abnormal cardiac function results in altered molecular expression which thereby results in the observed structural CHDs. Unfortunately this regulatory feedback loop (summarized in Figure 1.1) is poorly understood largely due to the lack of proper imaging tools to assess hemodynamic forces on the early developing heart. Previous efforts to investigate aortic arch development and hemodynamics have utilized corrosion casts, fluorescent dye microinjections, and micro-particle imaging velocimetry (μPIV) [51, 54, 188, 189]. The results of these measurements have been utilized to model the blood flow and shear stress patterns through each of the aortic arches using computational fluid dynamics. These studies have yielded valuable insights into the development of these vessels however the techniques utilized have short comings. Corrosion casts require sacrificing individual embryos at each stage of development eliminating the potential for longitudinal studies and injections of exogenous agents can potentially alter specific hemodynamic parameters.

Here we utilized optical coherence tomography (OCT) to obtain structural and functional images of the aortic arches in both ethanol exposed and control embryos. We have previously established a quail model of FAS that mimics a binge-drinking exposure at the stage of gastrulation, at which point a woman may not yet be aware of her pregnancy [29]. We previously reported that this model

results in abnormal development of the great vessels that includes missing vessels, double outlet right ventricle, misaligned aorta, as well as others [190]. It was our aim to longitudinally follow the progression of vessel formation from a stage when they were symmetrical through the time when they became asymmetric to test the hypothesis that the abnormal structure was preceded by altered shear stress in the specific aortic arch. We also wanted to monitor and measure the mesenchyme surrounding the vessels to determine if the smaller great vessel dimensions were present at earlier stages of development. To analyze the aortic arches of these embryo cohorts, Doppler OCT data was acquired at HH stage 19 of development. We have previously developed a dual-angle delay-encoded technique to simultaneously image a vessel from two different angles as discussed in Chapter 3. This technique allows for the rapid visualization and measurement of absolute pulsatile blood flow throughout the heartbeat from individual cross sectional images [86]. This data was then used to calculate the shear stress along the endothelium lining the vessel wall. Pulsed Doppler traces were also acquired to analyze trace morphology and measure the percentage of retrograde blood flow at the aortic arch. Finally, 3-D structural OCT volumes were acquired to measure cross sectional lumen areas as well as pharyngeal arch tissue size.

4.2 Experimental Procedures

4.2.1 Embryo preparation

Fertilized quail eggs were incubated in a humidified incubator at 38°C until HH stage 4-5 (gastrulation). At this stage the embryo is highly vulnerable for the induction of CHDs [28]. The eggs were divided into 3 groups: ethanol treated group, saline control group and an untreated group. Ethanol treated eggs were injected with 40 µL of 50% ethanol in saline, and saline control eggs were injected with 40 µL of saline. Ethanol dosage was based on previously published protocols [28] as being equivalent to one binge drink episode in humans and reliably produced FAS-associated abnormal phenotypes. The solutions were injected into the air space at the blunt end of the egg and the eggs were then incubated until HH stage 14 where the eggshells were removed and they were placed in the environmental OCT imaging chamber.

4.2.2 Optical Coherence Tomography Imaging

Once in the Petri dish, the embryos were placed in an environmental OCT imaging chamber [158] with controlled temperature (38°C) and humidity to ensure imaging under physiological conditions. At HH stage 19 the aortic arches of the embryos were imaged with our OCT system. Stage 19 was selected for imaging because at this stage both aortic arch III and IV have formed. These two vessels develop into the brachiocephalic arteries and the arch of aorta which were both shown to have a significantly reduced lumen area in our later stage ethanol exposed embryos. A swept source OCT system with a quasi-telecentric scanner [171] was used to collect simultaneous structural and Doppler images.

The OCT system utilizes a buffered Fourier domain mode-locked (FDML) laser with a line-rate of up to 500 kHz [191]. The axial resolution is 8 μm in tissue and the lateral resolution is ~10 μm [158]. A 1 mm^3 3-D structural data set covering the length of the aortic arches was acquired. The lumen area of the vessels was measured in Amira by analysis of multiple orthogonal cross sections along the length of the aortic arches.

4.2.3 Embryonic Staging

Traditionally, embryonic staging is performed by visualizing the embryo under a stereo microscope. Embryos are usually removed from the yolk due to the poor contrast. While this works well for individual experiment it makes accurate staging during longitudinal experiments very challenging since the embryo must remain on the yolk. Here, we verified embryonic developmental stages by acquiring multiple 3-D OCT structural volumes. Three OCT volumes spanning an area of 4 mm by 4 mm were acquired at sequential positions along the length of the embryo leaving approximately 750 μm of overlap between each data set. These volumes were then processed and imported into Amira for visualization. Volume renderings were generated and enface images were captured from the visualization. These 3 enface images were then loaded in Photoshop and aligned using the shared data from the overlapped region to create a complete image of the entire embryo (Figure 4.3a). The combined volume rendering was used to verify developmental stages. Limb buds, wing buds, head size and body morphology were all examined and compared with known developmental stages [30, 192].
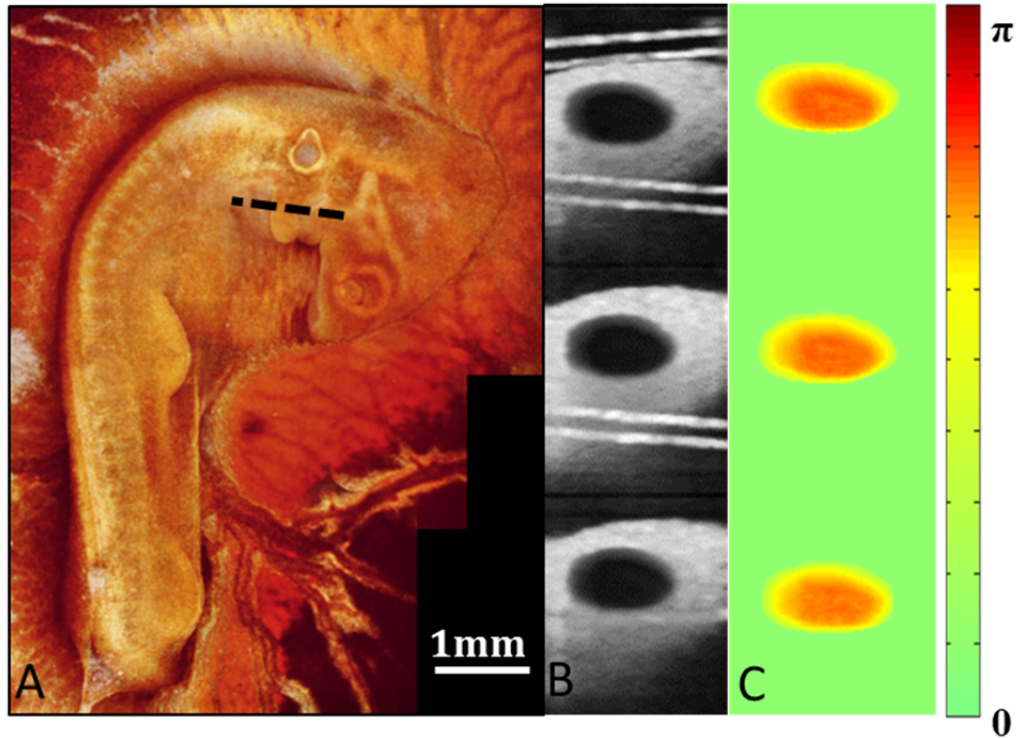
Figure 4.3: Aortic arch imaging

(A) A projection of the 3-D volumetric OCT data acquired for embryonic developmental staging. The image clearly displays the limb buds, wing buds and general head and body morphology necessary for accurate staging. (B) Cross sectional OCT images were acquired at the pharyngeal arches indicated by the dotted line in A. A phase variance image was generated from the Doppler OCT data to segment the aortic arch vessels. (C) The segmentation was applied to the Doppler OCT images for absolute blood flow calculations.

4.2.4 Absolute Blood Flow Calculation

OCT images were acquired of the pharyngeal arches at the location displayed by a dotted line in Figure 4.3a. In addition to structural images, Doppler OCT images were acquired from the aortic arches using dual beam delay encoded OCT as previously described in Chapter 3 [86]. 214 B-scan images spanning 0.5mm

were acquired over 4.6 seconds. Each image was composed of 200 A-scans with a Doppler average of 5. A phase variance image was generated from the OCT data in order to segment the lumen of vessel at each angle as shown in Figure 4.3b. The segmentation was performed manually in Amira for each data set. The segmented Doppler images were then used to determine the average Doppler angle over the 214 images. The average angle was then used to determine the absolute blood flow at each time point of heartbeat.

4.2.5 Hemodynamics Measurements

Absolute blood flow was acquired at each time point of the heartbeat. The flow in the aortic arches can be modeled as a tube in which the flow is laminar and all points are moving in the same direction. The shear stress can then be calculated using the relationship:

$$\tau_\omega = \frac{4Q\mu}{\pi r^3} \tag{4.1}$$

where τ_ω is the wall shear stress, Q is flow, r is the vessel radius, and μ is the fluid viscosity. We assumed a fluid viscosity of 5 mPa s based on previous literature [54, 132]. The average absolute blood flow and shear stress was calculated over a heartbeat. The peak forward and peak retrograde shear stress was determined by taking the 95th and the 5th percentile respectively. The oscillatory shear index (OSI) was also determined over the duration of a heartbeat as detailed in [161]. The OSI ranges from 0, if the shear is predominately in the same direction, to 0.5 if the average shear stress over time is zero.

4.2.6 Pharyngeal Arch Tissue Measurement

3D OCT volumes of the pharyngeal arches were acquired from uninjected, saline, and ethanol exposed embryos. The volumes imaged covered an area of 1mm x 2mm and 9 images were acquired at each location for averaging. This area includes the connection from the heart tube as well as the connection to the dorsal aorta and reflects the mesenchymal tissue volume comprised primarily of cardiac neural crest cells. The average volume was imported into Amira for visualization and segmentation. Orthogonal cross sectional slices were manually selected at the midpoint of the aortic arch. These slices were then manually segmented to measure the lumen area and the area of the surrounding mesenchymal tissue of the aortic arch.

4.3 Results

Pulsed Doppler traces were acquired from the 3rd aortic arch of ethanol exposed, saline injected, and uninjected cohorts of embryos (Figure 4.4). Ethanol exposed embryos were observed to have significantly increased retrograde blood flow compared to saline injected and uninjected control embryos. The average percentage of retrograde blood flow for ethanol exposed embryos was 8.2% while the uninjected and saline injected embryos were observed to have averages of 3.5% and 3.1% respectively. Ethanol exposed embryos were also observed to have altered pulsed Doppler trace morphology. The control and saline injected embryos possessed a positive peak with a prominent shoulder and a negative peak. The pulsed Doppler waveforms for the ethanol exposed

embryos often did not possess a shoulder as is shown in Figure 4.3b. These alterations to retrograde blood flow and pulsed Doppler waveform morphology are consistent with those shown previously [29].
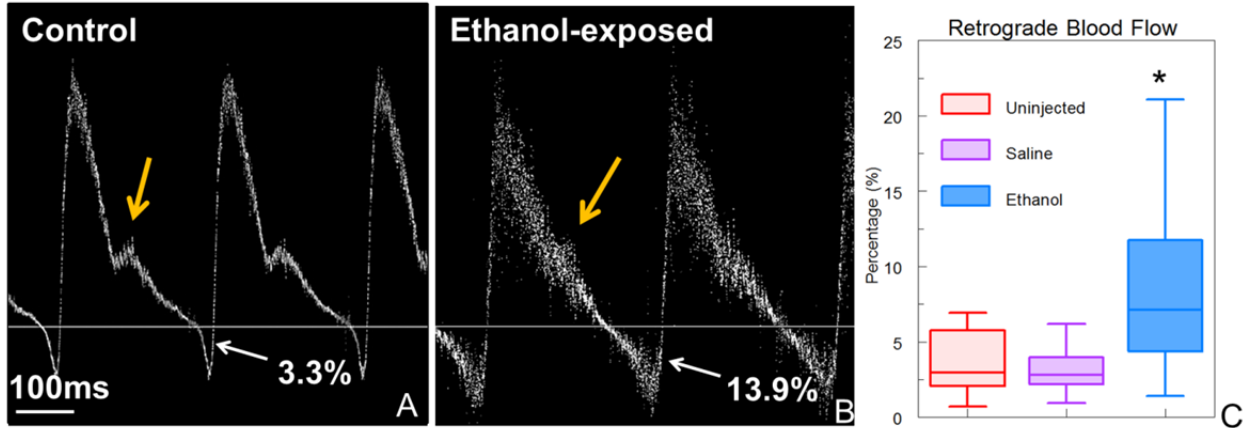
Figure 4.4: Pulsed Doppler traces and retrograde blood flow

Pulsed Doppler traces were acquired in the 3rd aortic arch of control and ethanol exposed embryos. (A) Control (uninjected and saline) embryos had pulsed Doppler traces with a positive peak with prominent shoulder (orange arrow) followed by a minor negative peak indicating the retrograde blood flow. (B) Pulsed Doppler traces for ethanol exposed embryos showed increased retrograde blood flow and often did not exhibit a shoulder. (C) Ethanol exposed embryos exhibited a statistically significant increase in average percentage of retrograde blood flow compared with both saline and uninjected embryos. * indicates $p < 0.05$

Cohorts of ethanol exposed, saline injected, and uninjected embryos were imaged using Doppler OCT at HH stage 19 of development in the aortic arch region. The average blood flow was determined over a heartbeat from dual beam delay encoded images. Ethanol exposed embryos were observed to have significantly higher average blood flow compared to saline and uninjected control

embryos (Figure 4.5A). The average blood flow in the ethanol exposed embryos was 0.26 µL/sec compared with the uninjected and saline embryos having 0.15 µL/sec and 0.14 µL/sec respectively. The shear stress produced by the blood dragging along the vessel lumen was also calculated. Due to the fact that the vessels cross sectional areas were the same while the blood flow was increased, the shear stress in ethanol exposed embryos were significantly higher (Figure 4.5B). Ethanol exposed embryos had an average shear stress of 0.52 Pa compared with uninjected embryos with 0.27 Pa and saline injected embryos with 0.29 Pa. To calculate the average shear stress over the duration of a heartbeat, the shear stress at each time point was calculated. The temporally resolved shear stress enabled the measurement of the oscillatory shear index for each embryo. Due to the increase in retrograde blood flow, the ethanol exposed embryos exhibited a higher OSI (0.08) than the uninjected (0.05) or saline injected (0.05) embryos (Figure 4.5C).

It has been shown that oscillating blood flow is an important factor in cardiovascular development [38]. As a result the peak forward and reverse blood shear stress, rather than the average blood flow, may be a critical factor involved in the hemodynamic response to ethanol exposure. To explore this possibility, we determined the peak magnitude of shear stress produced by both forward blood flow as well as retrograde blood flow. The ethanol exposed embryos exhibited significantly higher magnitudes of shear stress in both the forward and retrograde direction compared with the control and saline injected embryos (Figure 4.5D and 4.5E). On average ethanol exposed embryos had a peak shear stress of 1.81 Pa

in the forward direction and 0.43 Pa in the retrograde direction. Uninjected embryos had an average forward shear stress of 0.87 Pa and retrograde shear stress of 0.15 Pa while saline injected embryos had an average forward shear stress of 0.98 Pa and retrograde shear stress of 0.18 Pa.
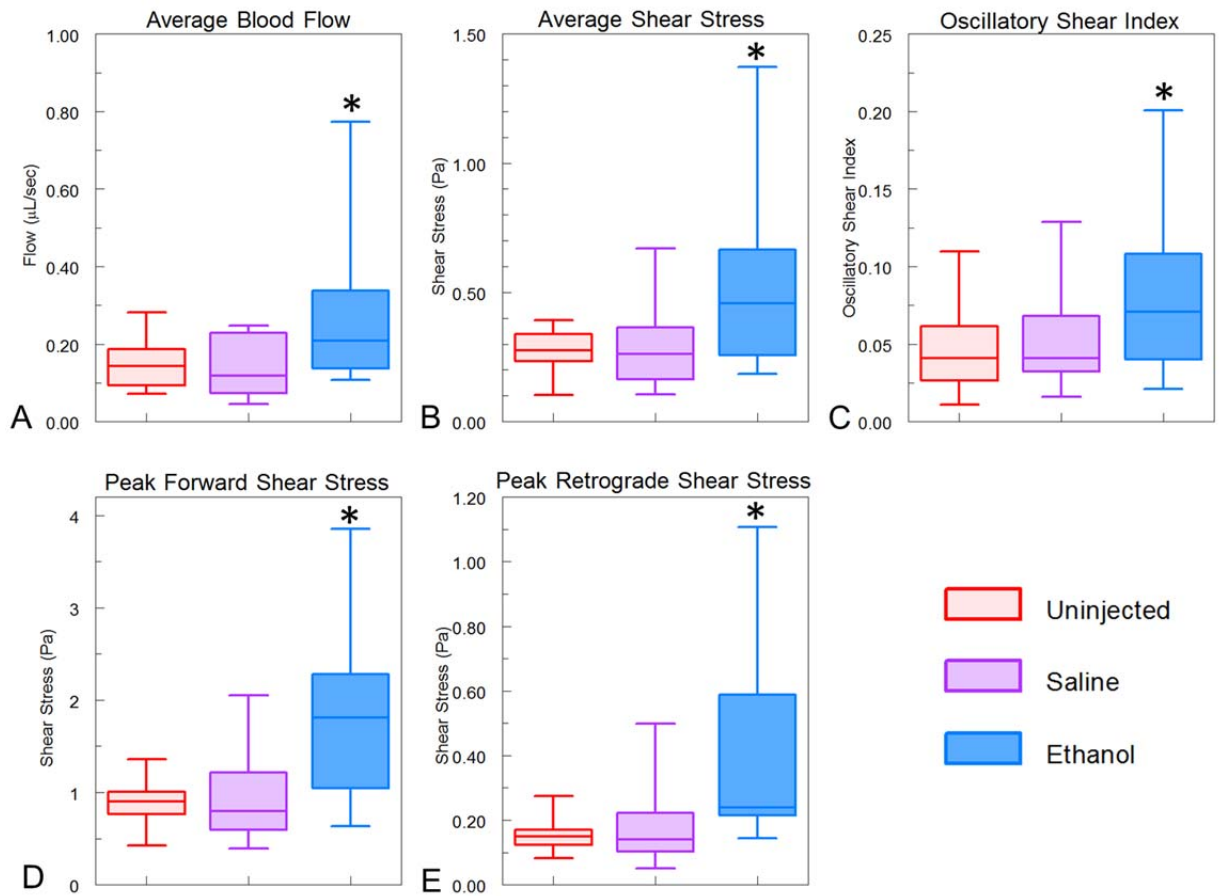
Figure 4.5: Hemodynamic measurements

Ethanol exposed embryos exhibited increased levels of all hemodynamic measurements. (A) Average blood flow was calculated over the duration of a heartbeat from multiple B-scan images. (B) These same images were used to determine the average shear stress produced by the blood dragging along the lumen wall. Ethanol exposed embryos had statistically significant increases in both average blood flow and shear stress. (C) The shear stress values over the heart beat were used to determine the oscillatory shear index which was increased in ethanol exposed embryos

due to the increased retrograde blood flow. (D and E) The peak forward and retrograde shear stress were determined and shown to be increased in ethanol exposed embryos in comparison with uninjected and saline controls. *indicates $p < 0.05$.

In addition to the hemodynamic alterations we wanted to determine if there were any changes to the morphology of the aortic arch vessel or the overall pharyngeal arch. Orthogonal slices from 3-D structural volumes of the aortic arches were selected and segmented to measure the cross sectional areas of the lumen and the surrounding tissue (Figure 4.6A). There was no significant change in the dimensions of the lumen cross sectional area in any of the cohorts of embryos (Figure 4.6B). The average lumen area for the uninjected, saline injected, and ethanol exposed embryos were 0.034 mm^2, 0.033 mm^2, and 0.034 mm^2 respectively. The ethanol exposed embryos did have a statistically significant decrease in the tissue surrounding the aortic arch vessel with an average of 0.055 mm^2. Uninjected embryos and saline injected embryos had similar cross sectional areas of tissue with an average of 0.063 mm^2 and 0.065 mm^2 respectively.
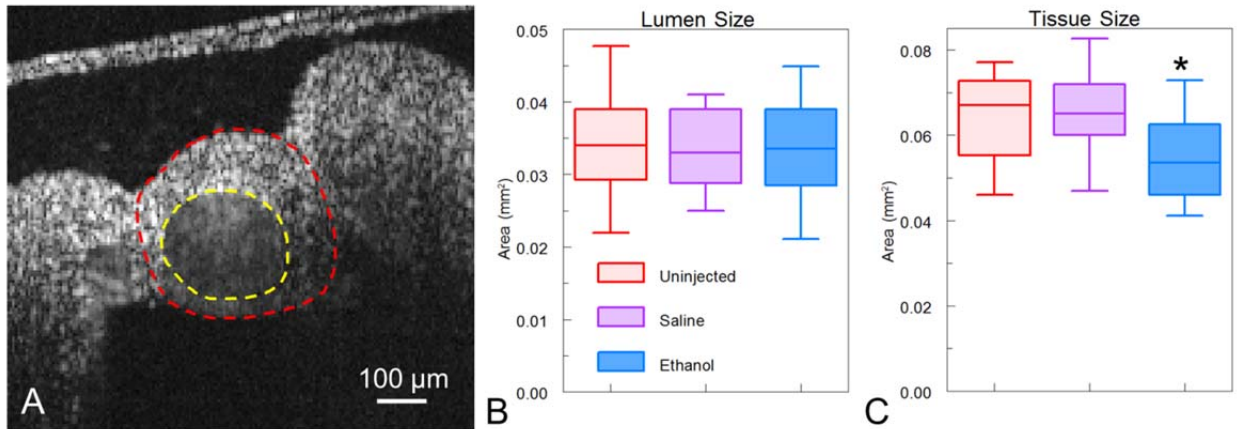
Figure 4.6: Pharyngeal arch tissue measurements

(A) An orthogonal slice from a 3-D volumetric acquisition of the 3rd aortic arch of an uninjected embryo. The lumen area was segmented and is indicated by the yellow dotted line. The surrounding pharyngeal arch tissue was then segmented and is indicated by the red dotted line. (B) Ethanol exposed embryos did not have a statistically significant change in the lumen cross sectional area compared with uninjected and saline embryos. (C) The surrounding pharyngeal arch tissue cross sectional area was statistically reduced in ethanol exposed embryos in comparison to uninjected and saline embryos. * indicates $p < 0.05$.

4.4 Discussion

We have previously reported increased retrograde blood flow and altered pulsed Doppler trace morphology in ethanol exposed embryos [29]. Those measurements were taken in the left vitelline arteries of HH stage 19 embryos. On average, we reported ethanol exposed embryos to have 10.96% of retrograde blood flow, uninjected embryos to have 2.42% of retrograde blood flow, and saline injected to have 3.34% of retrograde blood flow. These numbers are in close agreement with those presented here and any small discrepancies are likely the result of the fact that the pulsed Doppler trace was acquired in a

different region. Pulsed Doppler traces taken from the aortic arches should more accurately reflect cardiac function considering they are the first vessels that the blood enters upon exiting the heart. Both the previously reported pulsed Doppler traces as well as those presented here showed abnormal trace morphology in ethanol exposed embryos in the form of a reduced or missing shoulder. The existence of this abnormality immediately upon exiting the heart tube provides further evidence that this altered morphology is the result of abnormal cardiac cushion formation which has been shown to be related to ethanol exposure [29].

The shear stress calculations performed for this study and presented in this chapter are a simplification of those performed in Chapter 2. The 4-D shear stress maps previously generated were constructed from retrospectively gated imaging of the entire heart of HH stage 14 embryos. The acquisition of the 4-D data set required a few minutes of imaging which was possible with younger embryonic stages. Unfortunately, around 3 days of development (~HH stage 19) the quail embryo beings to randomly rock its entire body approximately once a minute. This made 4-D data acquisition challenging without investing in faster data acquisition methods. Fortunately, we had recently developed a method for rapid absolute flow calculations from individual B-scans as discussed in Chapter 3 [86]. By modeling the vessel as a tube, we were able to take advantage of this instantaneous flow information to calculate the shear stress without fear of gross embryonic movements. The modeling of the aortic arch as a tube does require some assumptions that are similar to those for the dual beam delay encoded imaging. These assumptions include that the vessel is rigid and the flow in the

vessel is in a single direction. There was no visible change in the aortic arch lumen area over the duration of a heartbeat in the imaged region. The cross sectional slices imaged in which Doppler OCT was performed were chosen at a position where the angle and size of the vessel is relatively stable. Thus these assumptions are generally valid on the time and spatial scale of the OCT images acquired here. The disadvantage of calculating shear stress from the blood flow information is that the results in a single number for the given cross sectional slice. Unlike the 4-D shear stress maps which given a shear stress value for every position along the endocardial wall, these shear stress calculations give an average value for the entire circumference of the lumen cross section. This averaged value prevents analysis of differential shear stress at various sections of the vessel. Higher speed 4-D data acquisition will enable shear stress maps of the entire vessel providing a more complete picture of the hemodynamic forces experienced by the aortic arches.

Decreased pharyngeal tissue size in ethanol exposed embryos may be the results of abnormal cardiac neural crest cell (CNCC) development. CNCCs are a subset of neural crest cells (NCCs) that play a critical role in the development of the aortic arches [193]. These cells migrate to the circumpharyngeal ridge and later progress into the pharyngeal arches and subset enter the cardiac outflow tract. The CNCCs in the pharyngeal arches then develop into smooth muscle cells enveloping and supporting the persisting aortic arches. The absence of, defects in, or the abnormal migration of CNCCs can result in an array of structural and functional defects in the great vessels and the heart, including

misalignment of the great vessels, outflow tract septation defects (PTA), and abnormal myocardial function [194-198]. Ethanol exposure has been shown to disrupt NCCs in many ways [199-204]. We hypothesize that the decreased pharyngeal arch tissue area in ethanol exposed embryos is a result of fewer CNCCs due to abnormal migration patterns, reduced proliferation, or simply increased cell death. Abnormal NCCs may also play a role in the observed hemodynamic changes in ethanol exposed embryos. Abnormal NCCs resulting from ablation studies have been shown to contribute to altered hemodynamics such as blood flow velocity, wall stress, cardiac output, and many more [205-208]. The altered hemodynamic forces measured here are likely a result of the combination of CNCCs related morphological and functional changes due to ethanol exposure. The reduced level of mesenchymal tissue around each vessel may alter their eventual ability to restructure and to be enveloped by smooth muscle cells and grow in diameter.

Longitudinal studies will be performed in the future to connect the observed early stage hemodynamic and structural abnormalities with the late stage great vessel defects. In this study, some embryos from each cohort were left to develop to HH stage 34. This is the stage at which our previously published great vessel measurements were taken [31]. In the previous paper, embryos were injected at the same embryonic stage, but were incubated in the eggshell until HH stage 34. The embryos were then removed from the eggshell and the hearts were excised and imaged with OCT after optical clearing [209]. The embryos presented here were allowed to develop until HH stage 34 in the covered Petri

dishes. The hearts were then excised, cleared and imaged just as the previous cohorts. Despite the different culturing protocols, both experiments showed decreased great vessel dimensions in ethanol exposed embryos compared with uninjected and saline injected controls [31](Figure 4.1). Future work will focus on improving our long term culturing protocols to enable sufficient yield for longitudinal analysis.

Chapter 5: Contractile Wave Velocity Measurements

5.1 Introduction

The heart is the first functional organ to develop during embryogenesis and its function is critical for the healthy development of the embryo and extraembryonic vasculature. Unfortunately, the mechanisms involved in cardiogenesis are still a poorly understood despite being the focus of much study in a variety of animal models. The avian embryonic heart tube begins to contract as early as HH stage 10 [50]. Interestingly, there is some evidence to suggest that this early contraction occurs before the embryonic tissue requires significant active transport of oxygen and nutrients. Studies have shown that the chick does not possess hemoglobin transport of oxygen before 3 days of development [210]. Additionally, groups have shown that complete ligation of the cardiac outflow results in no significant influence on oxygen consumption in the short term during early stages of development [211]. The role of early cardiac contraction is unclear; however, recent studies suggest that the resulting hemodynamic forces that the contraction generates are necessary for proper cardiogenesis.

Despite the unclear role of early cardiac contraction, abnormalities in the heart's tube ability to contract have been shown to result in various heart defects. Altered sarcomeric proteins which are key for contraction have been shown to result in altered cardiac cushions and the resulting valve leaflets [212]. Similarly, disruption of different myosin chains result in abnormal septal formation, altered valve leaflets, defective looping, and other cardiac defects [213-215]. Other groups have developed mouse mutants in which the heart grows and loops, but does not begin to beat resulting in embryonic lethality [216, 217]. Unfortunately,

the exact mechanisms of these defects remain largely unknown. Precise imaging tools are necessary to accurately visualize and monitor the contraction of the embryonic heart tube at early stages of development.

Contraction dynamics have been measured with various imaging modalities that are suited for embryonic heart developmental models. Zebrafish contraction has been visualized in 4-D by examining the movement of cells in the developing heart using confocal imaging [218]. Optical coherence tomography has recently emerged a powerful imaging tool that is well suited for studies on cardiac structure and function [29, 31, 85, 86]. Groups have used OCT to image the developing avian embryonic heart and measured the contraction velocities at precise orthogonal cross sectional slices [76, 82, 84, 163]. However, this measurement only examines the contraction speed at that specific cross sectional slice. In order to visualize the complete contraction dynamics along the entire length of the heart tube we need to obtain 3-D volumes over the entire heartbeat cycle. We have recently shown that OCT is capable of making detailed calculations of cardiac function from 4-D OCT data sets [85]. These same data sets should enable visualization and measurements of contraction dynamics.

Here we have presented a method of measuring contraction dynamics using 4-D OCT data sets. Multiple B-scans slices of an embryonic heart were gathered over time and then gated using image-based retrospective gating [74] to produce a 4-D structural data set. The myocardium of the imaged heart tubes were manually segmented and orthogonal cross sections were selected to measure the lumen area at each time point. The cross sectional lumen area was then

measured and plotted versus time at each position along the length of the heart tube. These plots were correlated and used to measure the contractile wave velocity in different regions along the heart tube. These values were then compared this conduction velocities acquired from optical mapping data sets.

5.2 Method

5.2.1 Embryo preparation

Fertilized quail eggs (Coturnix coturnix; Boyd's Bird Company, Inc. Pullman, WA.) were incubated in a humidified, forced draft incubator at 38°C (G.Q.F. Manufacturing Co., Savannah, GA). After 48 hours of development the eggs were taken from the incubator, the eggshell was removed, and the contents were placed in a sterilized 35 mm Petri dish [10]. Once in the Petri dish, the surviving embryos were placed in an environmental OCT imaging chamber [158] with controlled temperature (38°C) and humidity to ensure imaging under physiological conditions.

5.2.2 OCT imaging

The OCT system used to collect the data utilized a buffered Fourier Domain Mode Locked laser as previously described [82]. The in-depth and transverse resolution was 8 μm and 10 μm, respectively, in tissue. 4-D Doppler OCT data were collected by imaging over multiple heartbeats at sequential slice locations and reassembled using image-based retrospective gating [74]. 1000 A-scans were acquired per frame with a line rate of 117 KHz, and after reassembly a total of seventy volumes per heart beat were acquired. A-scans were recorded at 1.4

µm steps in the B-scan direction. Data were also acquired from a calibration interferometer and used to resample the data evenly in wavenumber and to improve the Doppler signal by correcting for laser phase noise[132]. For each B-scan Doppler image a five-line rolling average was employed to reduce phase noise and phase wrapping was corrected using a Goldstein algorithm [159].

5.2.3 Selection of orthogonal cross sectional slices

To measure the contraction wave velocity, a 3-D volume of the heart when it is most expanded (during diastole) was imported into Amira (Figure 5.1B). The myocardium was manually segmented and used to generate a centerline throughout the heart tube (Figure 5.1C and 5.1D). The centerline was created by an Amira module named 'CenterlineTree' which is based on a TEASAR (tree-structure extraction algorithm for accurate and robust skeletons) algorithm [160]. The module was restricted to a single line with a user defined start and end point and the resulting 3-D centerline was smoothed both in Matlab and Amira (Figure 5.1D). Orthogonal cross sectional slice orientations were manually determined at 20 µm intervals along the centerline of the heart tube (Figure 5.1E). At each position the cross sectional images at every time point over the heartbeat were generated and imported into Amira. The myocardium was then manually segmented over the heartbeat at each position (Figure 5.1F).
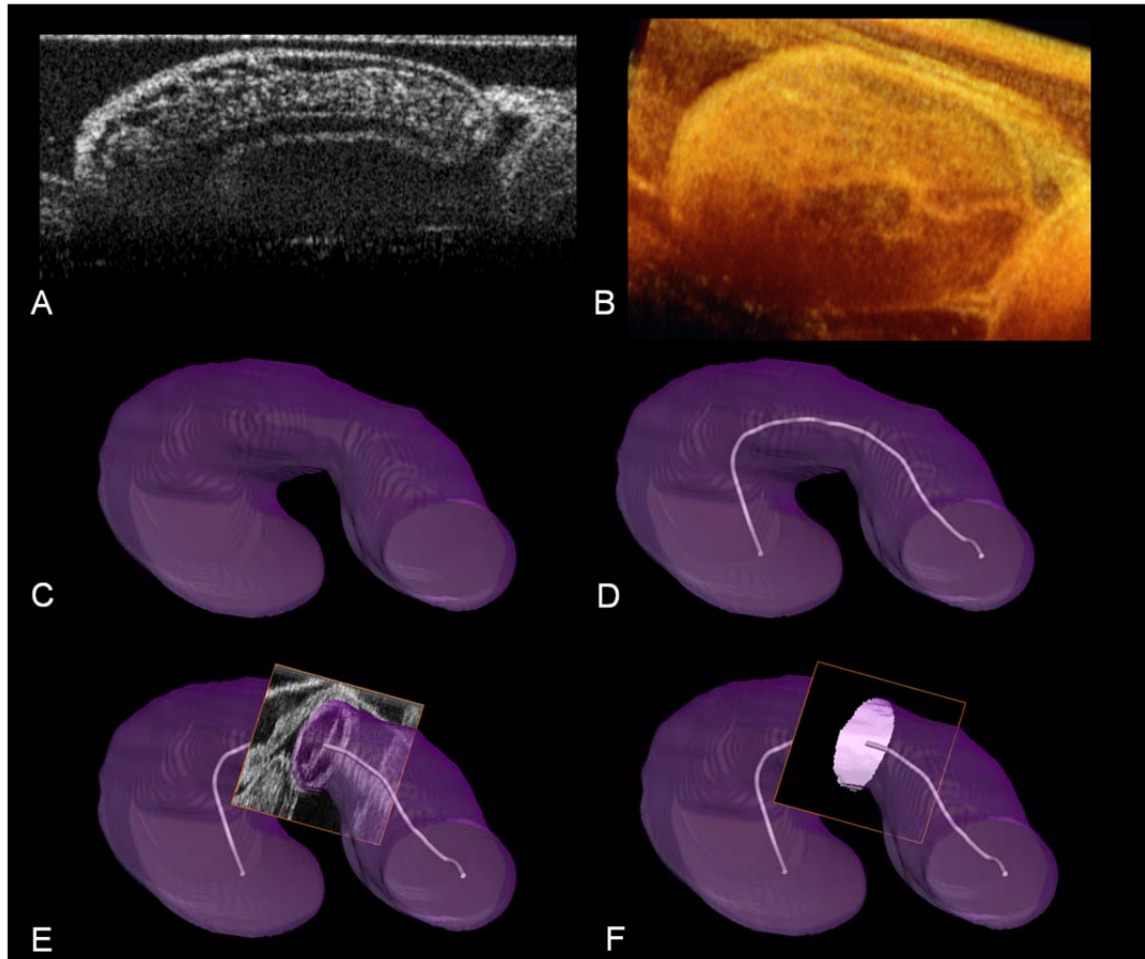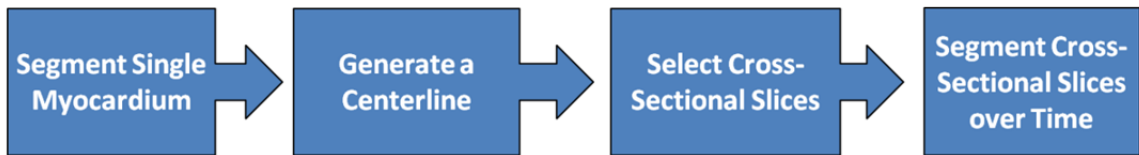
Figure 5.1: Flowchart for the steps utilized in cross sectional selection and segmentation.

(A) 4-D OCT data was acquired in sequential B-scan slices. (B) Those slices were retrospectively gated to generate 3-D volumes at each time point. (C) The 3-D volume of the tubular heart when it was most expanded was imported into Amira and the myocardium was manually segmented. A transparent surface rendering of the segmentation is displayed in purple. (D) The centerline was generated through the segmented myocardium shown as a white line through the surface generation. (E) Orthogonal cross sectional slice were manually selected at 20 µm. (F) The myocardium of the cross sectional slices were then segmented at each time point during the heartbeat.

5.2.4 Measurement of contraction wave velocities

The segmented cross sectional slices at each position were measured to determine the cross sectional area at each point in time. These values were then plotted versus time and normalized. Each plot can then be compared with the subsequent slice position for the determination of various contraction dynamics. The midpoint of the contraction portion of the cross sectional area plot was used to calculate the contraction velocity. The contraction velocities were calculated by measuring the time difference between two points that were chosen near the boundaries of the region of interest. Velocities were calculated in the ventricle as well as the outflow tract of the heart tube.
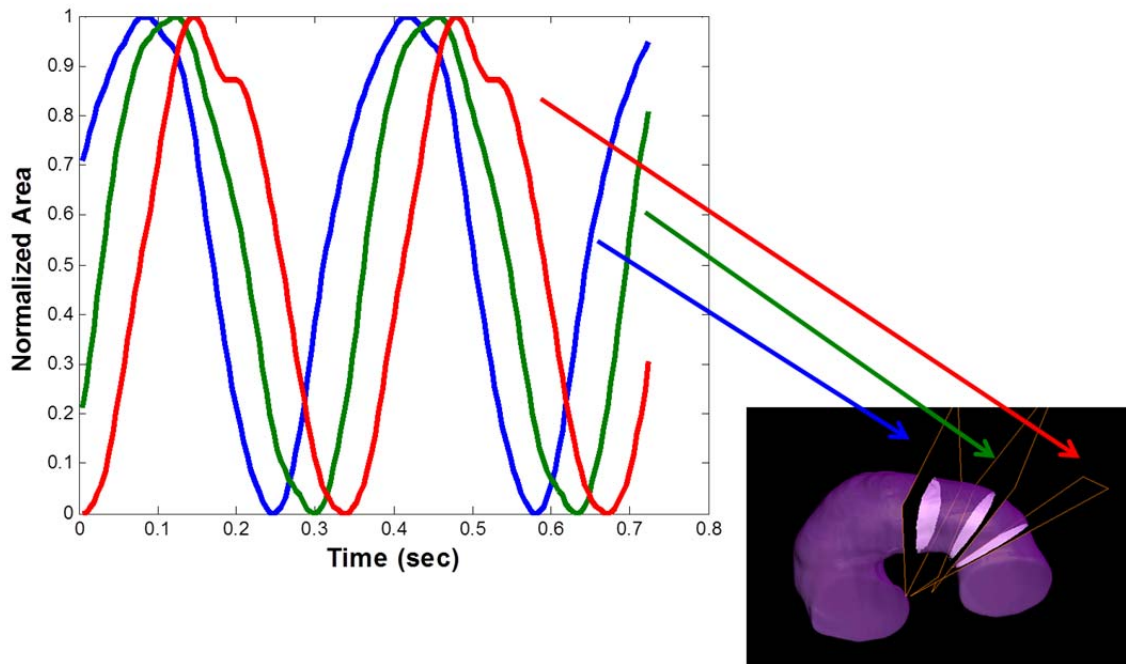
Figure 5.2: Plots of the cross sectional area of the myocardium of sequential orthogonal slices. Three representative slice locations have the myocardium areas plotted versus time in blue, green, and red. Each plot has been normalized for comparison. The corresponding segmented slices are shown on the surface rendering.

5.2.5 Optical Mapping

Contraction wave velocities were compared with conduction velocities obtained from optical mapping protocols as previously described [219, 220]. HH stage 14 quail hearts were dissected out and stained in 300 µL of 10 µM di-4-ANEPPS in Tyrode's solution for 12 minutes at room temperature. The stained hearts were then transferred to an imaging chamber filled with 1 mL of Tyrode's solution as well as 10 µM of cytochalasin D (CytoD) to inhibit myocardial contraction.

The optical mapping apparatus is housed within an enclosed box to reduce ambient light exposure. Two 50 W heaters and a temperature controller were used to maintain the temperature of the solution at 38 °C throughout the imaging. Optical mapping was performed with a broadband light-emitting diode light source. A custom filter and dichroic mirror set was utilized in the imaging apparatus. This set contained an excitation filter with a wavelength of 510 ± 40 nm, an emission filter with a wavelength of 685 ± 40 nm, and a dichroic mirror with a cutoff wavelength of 560 nm. The optical mapping signal was recorded with a 128 x 128 pixel EMCCD camera and an upright microscope. A zoom lens of 0.33X was utilized and images were acquired at 500 Hz.

To calculate conduction velocities two points were chosen at the edges of the region of interest. A cumulative normal distribution function was fit to the upstroke of each action potential trace. The inflection point of the cumulative normal distribution function was used to measure the conduction velocity. Velocities were calculated in the ventricle as well as the outflow tract of the heart tube for comparison with contractile wave velocities.

5.3 Results

The normalized myocardial cross sectional areas were plotted versus time at each position along the centerline of the heart tube. To visualize these plots along the entire length of the heart tube we created a 2-D color image in which the cross sectional area is represented by the colormap (Figure 5.3). Each position is plotted along the x axis and every time point is plotted along the y axis. The 2-D image clearly shows two regions with different contractile wave velocities. The ventricular region of the heart tube (left most section) appears to be contracting at the same time point indicating very rapid contraction propagation. The outflow tract region has a distinct observable slope indicating a slower contraction wave velocity.
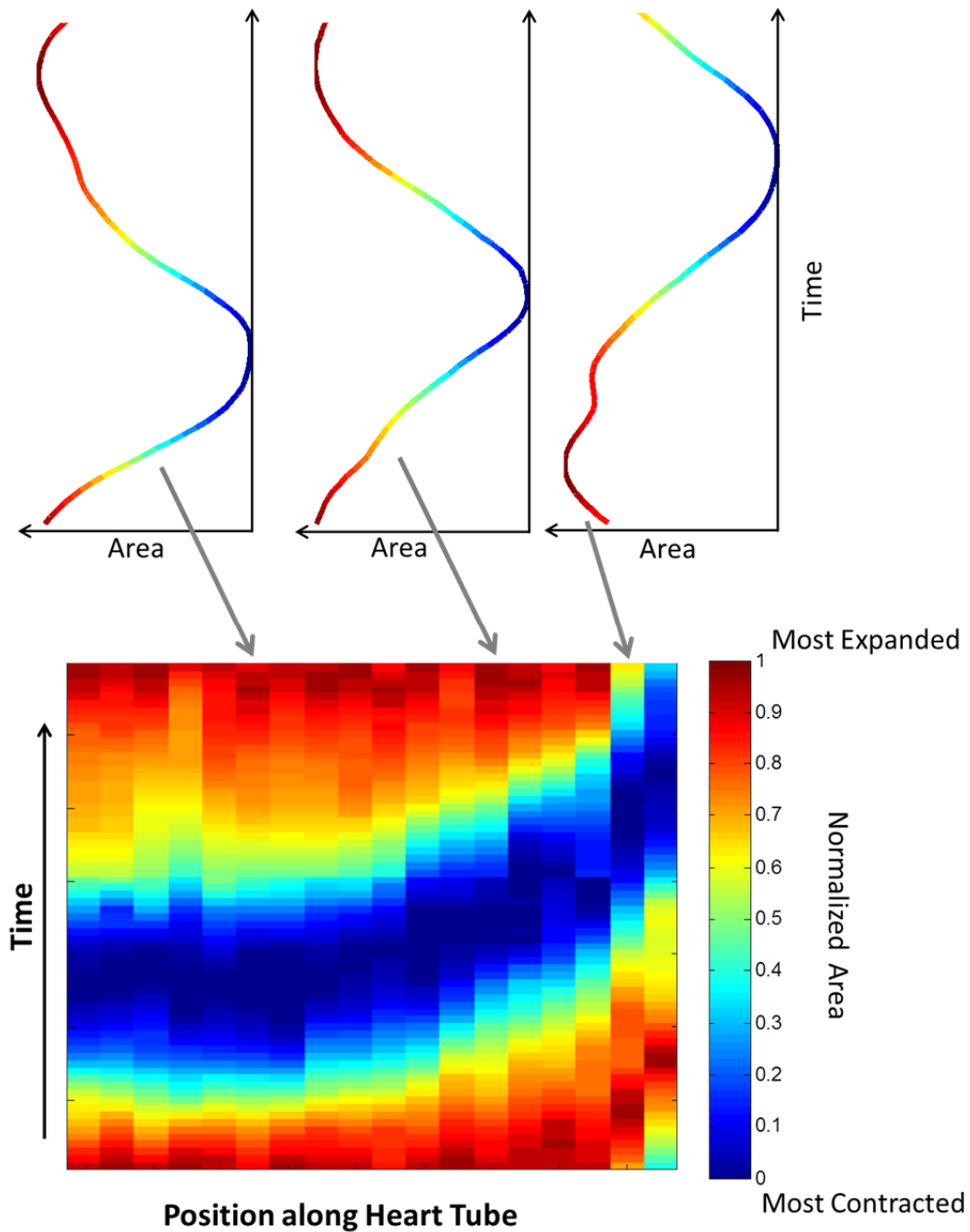
Figure 5.3: 2-D color image representation of the myocardial cross sectional area over time.

3 representative contraction traces are shown and plotted versus time. The normalized cross sectional area is represented by a color map with 0 (blue) representing the most contracted and 1 (red) representing the most expanded time points. Every trace is then stitched together in sequence to generate a 2-D color image with the x-axis representing the position along the heart tube.

The contraction plots along the length of the heart tube enable various types of measurements to be obtained. By selecting different time points of interest within the contraction plot, the contraction wave velocity or the relaxation wave velocities can be measured. The contraction speed and relaxation speed at each position can also be determined. In this work, we focused on measuring the contractile wave velocity by choosing the midpoint of the contraction portion of the cross sectional area plot versus time. The time of the midpoints was compared with those at different positions along the heart tube to obtain contractile wave velocity measurements in both the ventricle and outflow tract of the heart tube. The 3 hearts that were measured had contractile wave velocities of 2.69 mm/sec, 5.60 mm/sec, and 1.59 mm/sec in the outflow tract and 25.92 mm/sec, 26.70 mm/sec, and 24.47 mm/sec in the ventricle (Figure 5.4). The velocities at each region were relatively consistent across the 3 hearts measured despite the very rapid contractile propagation in the ventricle.
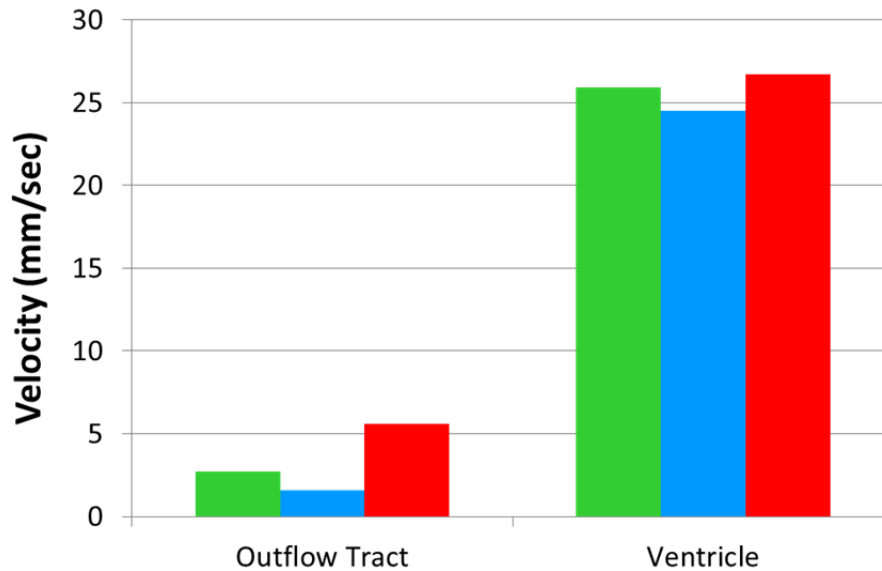
Figure 5.4: Contraction velocity measurements

The bar graph displays the contraction velocity in the outflow tract and the ventricular region of 3 HH stage 14 hearts. The green, blue, and red bars represent the three different hearts measured.

The contractile wave velocities were compared with conduction velocities obtained from optical mapping (Figure 5.5). Although these are different dynamic processes, we expect them to have similar values to help validate the velocities we are measuring. The conduction velocities and contractile wave velocities showed good agreement with each other leading us to believe our contractile wave velocity values. The ventricle conduction velocity and contractile wave velocity had a larger difference than the velocities in the outflow tract. This is potentially the result of the different embryonic heart preparations. The contractile wave velocities were measured with the embryo intact and under physiological conditions whereas the conduction velocities were measured from excised

hearts. The excised heart may have reduced cardiac functions thus resulting in the lower measured ventricle velocities.
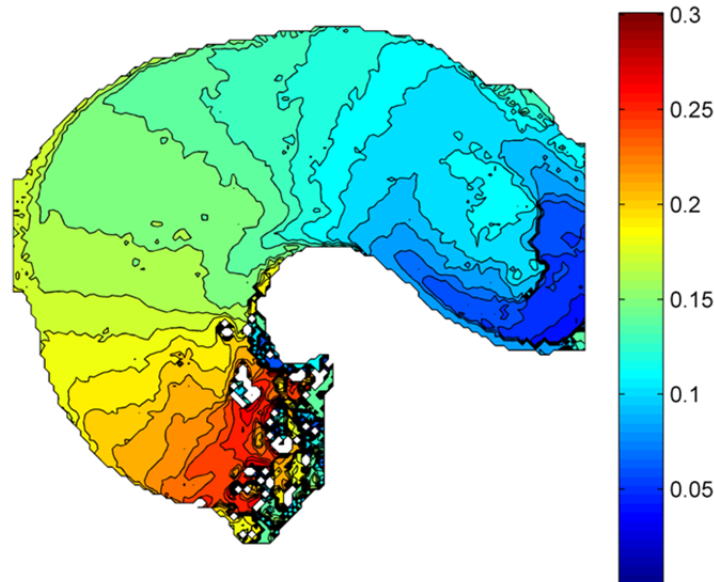
	Outflow Tract	Ventricle
Contractile Velocity	3.3 mm/sec	25.7 mm/sec
Conduction Velocity	3.0 mm/sec	18.5 mm/sec

Figure 5.5: Comparison of contractile wave velocities with conduction velocities

Optical mapping was performed to calculate conduction velocities in the developing embryonic heart. A representative activation map is shown of a HH stage 14 heart. The color map values are in seconds and the isochrones are 10 ms apart. The table shows the average contractile wave velocity and conduction velocity from 3 separate hearts. The measurements were performed in the outflow tract of the heart tube and in the ventricle.

5.4 Discussion

Here we have demonstrated a technique for measuring the contractile wave velocity in different regions of the heart tube. However, this measurement

required some assumptions in order to calculate. Here we utilized a single centerline generated from the segmented myocardium of the heart when it is most expanded. We assumed that the centerline is relatively stationary through the heartbeat. Other groups have investigated the stability of the centerline and found that it only changed slightly [146]. Therefore, we do not believe that this factor will significantly influence the measurements made here. We also assumed that there was no significant bulk motion of the regions of the heart tube measured. Significant bulk motion would alter the section of the myocardium being measured in the cross sectional slices. The regions that we performed our measurements on here (ventricle and outflow tract) are relatively stable sections of the heart throughout the heart beat with little out of plane motion. If out of plane motion were to have a significant influence on the contraction dynamic measurements, image registration could be used in order to compensate.

There are some limitations to the contraction measurements reported here. One limitation is that a single value is used to characterize the contractile wave velocity in each region of the heart tube. The heart is in fact a curved tube and likely has different velocities on either side of the heart tube. We have previously shown that the endocardial shear stress is greater on the inner curvature of the heart versus the outer curvature [85]. The fact that the outer curvature has a longer path for the contraction to travel makes it likely that the heart tube also has different contractile wave velocities. Precise tracking of points along the myocardial wall to measure the contraction at each location would allow for the generation of contraction traces at each tracked position. This in turn would allow

for differential contraction wave velocities within regions of the heart tube. Another limitation is the accuracy of measurements from the ventricle region of the heart tube. In this section, the contractile wave travels very rapidly. Measuring the velocity in this region is challenging due to the few number of time points acquired. This can be overcome with more rapid imaging systems enabling more volumes to be acquired during each heartbeat from the measurements of the ventricle.

To partially validate our contractile wave velocity measurements in each region they were compared with conduction velocities obtained from optical mapping. This comparison was made in view of the fact that myocardial contraction is coupled to electric activation. However, these measurements are made under different experimental circumstances. Optical mapping is performed on excised hearts that have been exposed to cytoD to inhibit myocardial contraction. OCT imaging on the other hand was performed on intact embryos under physiological conditions. Despite these differences in preparation, the two measured velocities yielded similar values in two independent regions of the heart tube.

The measurements presented here were calculated through manual segmentation of the myocardium of the heart tube. In the future, the endocardium could be segmented as well in order to study any potential differences in the contractile wave velocity compared with the myocardium. Additionally, the time difference between contraction traces was made by comparing the midpoint of the contraction portion of the trace. However, this is not necessarily the most

accurate or physiologically relevant method. It would be interesting to investigate any differences in velocities based on the time point of comparison.

In conclusion we have demonstrated a method for measuring contractile ave velocity in the developing heart tube. These velocities were shown to be in good agreement with conduction velocities obtained from the same regions in the heart tube. In the future, these measurements will be useful for probing which specific parameters are affected in various models of CHDs.

Chapter 6: Summary and Future Directions

6.1 Summary

Hemodynamic forces are critical for proper cardiovascular development at early embryonic stages. This dissertation presented several techniques to measure and monitor various cardiac functions using structural and Doppler OCT imaging. 4-D shear stress maps, absolute blood flow measurements, contractile wave velocities, and structural abnormalities were measured in the heart tube as well as the surrounding vasculature. These calculations were also performed on various perturbation models including ethanol exposure and optical pacing to compare with control embryo cardiac function.

In chapter 1, our motivation for investigating hemodynamic forces was introduced. A brief description of CHDs was presented as well as the various embryonic animal models used in studies focusing on heart development. We summarized our rationale for choosing the avian model as well as the general steps of cardiogenesis. The ethanol exposure model that we have developed was introduced as one of the various perturbation models our group uses to assess cardiovascular development. The importance of hemodynamic forces for proper heart development is explained as well as their role in a feedback loop in which cardiac function influences molecular signaling, which in turn alters cardiac structure resulting in abnormal cardiac function. Previous imaging techniques for monitoring and measuring cardiac function are introduced and explained. Finally OCT is shown to be an imaging modality well suited for imaging embryonic heart development. Both TD-OCT and both methods of FD-OCT, SS-OCT and SD-OCT, are explained with system diagrams. An explanation of Doppler OCT is

presented and explained to be a powerful tool for investigations of hemodynamic forces in the developing embryonic heart.

A technique to generate 4-D shear stress maps is the first hemodynamic measurement explained in this thesis work. Shear stress is a critical biomechanical force that has been shown to influence various molecular signals that are critical for proper heart development. To precisely determine the location within the heart tube that the shear stress is influencing, a 3-D map is required at multiple time points throughout the heartbeat. 4-D Doppler OCT data was acquired via image based retrospective gating. The endocardium at multiple time points was then segmented and used as a surface for generating the shear stress maps. The generated 4-D shear stress maps enable precise spatial and temporal analysis of the forces at different parts of the heart tube. The shear stress at any point along the heart tube is able to be monitored and measured throughout the duration of the heartbeat. We also observed increased peak shear stress values along the inner curvature of the heart tube's outflow tract compared with the outer curvature. The shear stress measurements were validated by imaging a capillary tube flow phantom at various shear rates. This technique was also used to observe altered shear stress and OSI values in optically paced embryos compared with control embryos.

The third chapter describes a technique for orientation independent absolute blood flow measurements. One of the drawbacks of Doppler OCT is that it is only sensitive to movement in the axial direction or in the direction that is parallel with the imaging beam. Here we utilized a dual angle delay encoded

125

technique to measure the same position in a blood vessel from two different angles with a known angular separation. This is done by inserting a piece of glass partway into the imaging beam, splitting the incident light into two different sub-beams with different incident angles. When these beams are orientated perpendicularly to the B-scan direction, the absolute blood flow can be calculated from a single cross sectional image. This technique was validated by imaging an optical flow phantom as well as imaging embryonic yolk sac vessels. The calculated flow rates showed that the technique was angle independent and capable of measuring pulsatile blood flow from individual B-scan images.

Chapter 4 presented our work with imaging the aortic arches of control and ethanol-exposed embryos. Ethanol exposure at early stages of development has been shown to influence the patterning and dimensions of the great vessels of the late stage heart. To determine the role hemodynamics may play in these defects, the blood flow and shear stress were measured in the developing aortic arches, which are the precursors for the great vessels. The blood flow was calculated from individual cross sectional slices as detailed in chapter 3. This information was then used to determine the shear stress in the aortic arch. Ethanol exposed embryos were observed to have increased average blood flow and average shear stress values when compared with control embryos. Perturbed embryos were also observed to have significantly increased peak forward shear stress and retrograde shear stress. In addition to blood flow and its resulting forces, the structure of the aortic arches and the surrounding pharyngeal arch tissue was measured with 3-D OCT volumes. Orthogonal cross

sectional slices were manually selected and segmented to measure the lumen area as well as the mesenchymal tissue surrounding the aortic arch. The lumen cross sectional area was shown to be the same in all embryo cohorts; however, the surrounding tissue was significantly reduced in the ethanol exposed embryos compared with control embryos. This is likely due to abnormalities related to the cardiac neural crest cells.

Finally, contractile wave velocities were calculated in sections of the developing embryonic heart. 4-D OCT data sets were acquired and the myocardium was manually segmented. A centerline was generated and used to manually select orthogonal cross sectional slices. The cross sectional area was measured at each time point during the heartbeat. The lumen area was then plotted versus time at each sequential position along the length of the heart tube. Contractile wave velocities in the ventricle and the outflow tract were calculated by correlating the cross sectional area plots to determine the temporal delay between subsequent positions. These velocities were compared with conduction velocities in the same regions obtained from optical mapping. The velocities from both the OCT images and the optical mapping showed good correlation in both the ventricle and the outflow tract of the heart tube.

The techniques developed and demonstrated in these chapters have shown that structural and Doppler OCT is well suited for investigating the hemodynamic forces in the developing embryonic heart tube. The ability to measure these cardiac functions may help investigators determine the exact mechanisms that contribute to congenital heart defects.

6.2 Future Directions

The techniques presented here may open up the possibility for many interesting investigations in the future. In this section we discuss some future studies that may make use of these hemodynamic measurements as well as some potential improvements to the techniques developed here.

6.2.1 Complete 4-D Shear Stress Maps

In this dissertation we presented a technique for generating shear stress maps of the developing embryonic heart in 4-D. These maps presented precise spatial and temporal shear stress values in the outflow tract and AV junction of the heart where we were primarily interested. Unfortunately, due to Doppler OCT only bring sensitive to movement in the direction parallel with the imaging beam, we were unable to calculate accurate shear stress values for the top most region of the heart tube where the flow is perpendicular to the imaging beam (Figure 2.3). Future studies may be able to utilize some of the methods described in chapter 3 to acquire accurate blood velocities in this region of the heart tube. Alternatively, an additional 4-D Doppler OCT data set could be acquired from a different incident angle. The resulting volumes could then be registered with those already obtained to create a complete 4-D Doppler data set. The registered Doppler data would then allow for a complete 4-D shear stress map.

6.2.2 4-D Aortic Arch Shear Stress Maps

We presented our work on measuring altered hemodynamics and abnormal morphology in ethanol exposed aortic arches compared with control embryos. Although these measurements showed that the hemodynamic forces were

significantly increased in ethanol exposed embryos, they generated a single shear stress value to represent the entire aortic arch. This was partially necessitated by the significant bulk motion of the embryo at this stage of development making 4-D data acquisition challenging. Significant advancements in high speed lasers have made megahertz A-scan rates possible [119]. These speeds will allow for 4-D data sets to be acquired of the entire aortic arches without worry of embryonic motion. This increased speed will enable detailed spatial and temporal shear stress maps of the aortic arches like the ones demonstrated in chapter 2.

6.2.3 Longitudinal Studies

Our investigations using the ethanol exposed model have yielded insights into various hemodynamic and structural abnormalities in the early stage heart tube as well as late stage hearts. We have observed altered great vessel morphology and abnormal pharyngeal arch tissue cross sectional areas, but we have yet to acquire these measurements from the exact same embryo at these two different stages of development. As a noninvasive, noncontact imaging modality, OCT is well suited for longitudinal studies. With improved culturing techniques we will be able to follow control and perturbed embryos across various developmental stages. Future longitudinal studies may help determine the correlation between our observed early stage hemodynamic abnormalities and the later stage structural defects.

6.2.4 Real-Time Hemodynamic Measurements

Future studies of embryonic heart development could benefit from real-time 3-D visualization of the beating heart as well as real-time measurements of hemodynamics. Advancements in GPU processing have already enabled video rate volumetric rendering of the human eye [221]. These same processing techniques could be applied to imaging the developing heart tube enabling real-time 3-D visualization of contraction throughout the heartbeat. In addition to monitoring the heart in 4-D, hemodynamic measurements could also be acquired in real-time. The technique to measure absolute blood flow from individual cross sectional slices detailed in chapter 3 can be used to report blood flow rates in real-time. By automatically segmenting the lumen area using speckle or phase variance the blood flow can then be calculated with the user simply selecting the region of interest. This information could also be used to calculate the shear stress in that cross sectional region. Pulsed Doppler traces could be acquired by selecting points of interest and plotting the phase differences as the OCT data is acquired. These real-time measurements and visualizations can improve the utility of OCT by enabling precise monitoring of various perturbations.

Bibliography

1. Go, A.S., et al., *Heart Disease and Stroke Statistics—2013 Update: A Report From the American Heart Association.* Circulation, 2013. **127**(1): p. e6-e245.

2. Lloyd-Jones, D.M., et al., *Defining and Setting National Goals for Cardiovascular Health Promotion and Disease Reduction: The American Heart Association's Strategic Impact Goal Through 2020 and Beyond.* Circulation, 2010. **121**(4): p. 586-613.

3. Marelli, A.J., et al., *Congenital Heart Disease in the General Population: Changing Prevalence and Age Distribution.* Circulation, 2007. **115**(2): p. 163-172.

4. Lane, D.A., G.Y.H. Lip, and T.A. Millane, *Quality of life in adults with congenital heart disease.* Heart, 2002. **88**(1): p. 71-75.

5. Syed, S.H., et al., *Optical coherence tomography for high-resolution imaging of mouse development in utero.* Journal of Biomedical Optics, 2011. **16**(4): p. 046004.

6. Takahashi, M. and N. Osumi, *The method of rodent whole embryo culture using the rotator-type bottle culture system.* J Vis Exp, 2010(42).

7. Kalaskar, V.K. and J.D. Lauderdale, *Mouse embryonic development in a serum-free whole embryo culture system.* J Vis Exp, 2014(85).

8. Kirby, M.L., *Cardiac development*. 2007, Oxford ; New York: Oxford University Press. xiii, 273 p.

9. Schomann, T., et al., *Improved Method for Ex Ovo-Cultivation of Developing Chicken Embryos for Human Stem Cell Xenografts.* Stem Cells International, 2013. **2013**: p. 960958.

10. Dunn, B.E., *Technique of shell-less culture of the 72-hour avian embryo.* Poult Sci, 1974. **53**(1): p. 409-12.

11. *Sequence and comparative analysis of the chicken genome provide unique perspectives on vertebrate evolution.* Nature, 2004. **432**(7018): p. 695-716.

12. Wallis, J.W., et al., *A physical map of the chicken genome.* Nature, 2004. **432**(7018): p. 761-764.

13. Wong, G.K., et al., *A genetic variation map for chicken with 2.8 million single-nucleotide polymorphisms.* Nature, 2004. **432**(7018): p. 717-22.

14. Jensen, P., *Genomics: The chicken genome sequence.* Heredity, 2005. **94**(6): p. 567-568.

15. Robb, E.A., et al., *Chromosomal Mapping and Candidate Gene Discovery of Chicken Developmental Mutants and Genome-Wide Variation Analysis of MHC Congenics.* Journal of Heredity, 2011. **102**(2): p. 141-156.

16. Markwald, R., T. Trusk, and R. Moreno-Rodriguez, *Formation and Septation of the Tubular Heart: Integrating the Dynamics of Morphology With Emerging Molecular Concepts*, in *Living Morphogenesis of the Heart*, M. de la Cruz and R. Markwald, Editors. 1998, Birkhäuser Boston. p. 43-84.

17. Manasek, F., *Heart development: interactions involved in cardiac morphogenesis.* Cell surface reviews, 1976.

18. Goldstein, A.M., B.S. Ticho, and M.C. Fishman, *Patterning the heart's left-right axis: From zebrafish to man.* Developmental Genetics, 1998. **22**(3): p. 278-287.

19. Floyd, R.L. and J.S. Sidhu, *Monitoring prenatal alcohol exposure.* Am J Med Genet C Semin Med Genet, 2004. **127C**(1): p. 3-9.

20. Finer, L.B. and S.K. Henshaw, *Disparities in rates of unintended pregnancy in the United States, 1994 and 2001.* Perspect Sex Reprod Health, 2006. **38**(2): p. 90-6.

21. Jones, K.L. and D.W. Smith, *Recognition of the fetal alcohol syndrome in early infancy.* Lancet, 1973. **302**(7836): p. 999-1001.

22. Clarren, S.K. and D.W. Smith, *The fetal alcohol syndrome.* Lamp, 1978. **35**(10): p. 4-7.

23. Abel, E., ed. *Fetal Alcohol syndrome*. 1990, Medical Economics Books: Oradell, NJ.

24. Grewal, J., et al., *Maternal periconceptional smoking and alcohol consumption and risk for select congenital anomalies.* Birth Defects Res A Clin Mol Teratol, 2008. **82**(7): p. 519-26.

25. Flentke, G.R., et al., *Calcium-mediated repression of beta-catenin and its transcriptional signaling mediates neural crest cell death in an avian model of fetal alcohol syndrome.* Birth Defects Res A Clin Mol Teratol, 2011. **91**(7): p. 591-602.

26. Binkhorst, M., et al., *Glycosylation defects underlying fetal alcohol spectrum disorder: a novel pathogenetic model. "When the wine goes in, strange things come out" - S.T. Coleridge, The Piccolomini.* J Inherit Metab Dis, 2012. **35**(3): p. 399-405.

27. Marrs, J.A., et al., *Zebrafish fetal alcohol syndrome model: effects of ethanol are rescued by retinoic acid supplement.* Alcohol, 2010. **44**(7-8): p. 707-15.

28. Serrano, M., et al., *Fetal alcohol syndrome: cardiac birth defects in mice and prevention with folate.* Am J Obstet Gynecol, 2010. **203**(1): p. 75 e7-75 e15.

29. Karunamuni, G., et al., *Ethanol exposure alters early cardiac function in the looping heart: a mechanism for congenital heart defects?* American Journal of Physiology - Heart and Circulatory Physiology, 2013.

30. Hamburger, V. and H.L. Hamilton, *A series of normal stages in the development of the chick embryo.* Journal of Morphology, 1951. **88**(1): p. 49-92.

31. Karunamuni, G., et al., *Using optical coherence tomography to rapidly phenotype and quantify congenital heart defects associated with prenatal alcohol exposure.* Dev Dyn, 2014.

32. Hogers, B., et al., *Extraembryonic venous obstructions lead to cardiovascular malformations and can be embryolethal.* Cardiovascular Research, 1999. **41**(1): p. 87-99.

33. Broekhuizen, M.L.A., et al., *Altered hemodynamics in chick embryos after extraembryonic venous obstruction.* Ultrasound in Obstetrics and Gynecology, 1999. **13**(6): p. 437-445.

34. Hove, J.R., et al., *Intracardiac fluid forces are an essential epigenetic factor for embryonic cardiogenesis.* Nature, 2003. **421**(6919): p. 172-7.

35. Reckova, M., et al., *Hemodynamics is a key epigenetic factor in development of the cardiac conduction system.* Circ Res, 2003. **93**(1): p. 77-85.

36. Groenendijk, B.C.W., et al., *Changes in Shear Stress–Related Gene Expression After Experimentally Altered Venous Return in the Chicken Embryo.* Circulation Research, 2005. **96**(12): p. 1291-1298.

37. Hogers, B., et al., *Unilateral vitelline vein ligation alters intracardiac blood flow patterns and morphogenesis in the chick embryo.* Circ Res, 1997. **80**(4): p. 473-81.

38. Vermot, J., et al., *Reversing Blood Flows Act through klf2a to Ensure Normal Valvulogenesis in the Developing Heart.* Plos Biology, 2009. **7**(11): p. -.

39. Jenkins, M.W., et al., *Optical pacing of the embryonic heart.* Nat Photon, 2010. **4**(9): p. 623-626.

40. Peterson, L.M., et al. *Altering embryonic cardiac dynamics with optical pacing*. in *Engineering in Medicine and Biology Society (EMBC), 2012 Annual International Conference of the IEEE*. 2012.

41. Ford, S. *Altering Hemodynamics in Early Heart Development with Optical Pacing Leads to Congenital Heart Defects*. in *2014 AAP National Conference and Exhibition*. 2014: American Academy of Pediatrics.

42. Huddleson, J.P., N. Ahmad, and J.B. Lingrel, *Up-regulation of the KLF2 Transcription Factor by Fluid Shear Stress Requires Nucleolin.* Journal of Biological Chemistry, 2006. **281**(22): p. 15121-15128.

43. Atkins, G.B. and M.K. Jain, *Role of Kruppel-like transcription factors in endothelial biology.* Circulation Research, 2007. **100**(12): p. 1686-95.

44. Basu, P., et al., *KLF2 is essential for primitive erythropoiesis and regulates the human and murine embryonic beta-like globin genes in vivo.* Blood, 2005. **106**(7): p. 2566-2571.

45. Groenendijk, B.C., et al., *The role of shear stress on ET-1, KLF2, and NOS-3 expression in the developing cardiovascular system of chicken embryos in a venous ligation model.* Physiology (Bethesda), 2007. **22**: p. 380-9.

46. Dekker, R.J., et al., *Prolonged fluid shear stress induces a distinct set of endothelial cell genes, most specifically lung Krüppel-like factor (KLF2).* Blood, 2002. **100**(5): p. 1689-1698.

47. Bremer, J.L., *The presence and influence of two spiral streams in the heart of the chick embryo.* American Journal of Anatomy, 1932. **49**(3): p. 409-440.

48. Jaffee, O.C., *HEMODYNAMIC FACTORS IN THE DEVELOPMENT OF THE CHICK EMBRYO HEART.* Anat Rec, 1965. **151**: p. 69-75.

49. Leyhane, J., *Visualization of blood streams in the developing chick heart.* Anat Rec, 1969(163): p. 312-313.

50. Hogers, B., et al., *Intracardiac Blood Flow Patterns Related to the Yolk Sac Circulation of the Chick Embryo.* Circulation Research, 1995. **76**(5): p. 871-877.

51. Wang, Y., et al., *Aortic arch morphogenesis and flow modeling in the chick embryo.* Annals of Biomedical Engineering, 2009. **37**(6): p. 1069-81.

52. Yoshida, H., F. Manasek, and R.A. Arcilla, *Intracardiac flow patterns in early embryonic life. A reexamination.* Circ Res, 1983. **53**(3): p. 363-71.

53. Lee, J.Y., H.S. Ji, and S.J. Lee, *Micro-PIV measurements of blood flow in extraembryonic blood vessels of chicken embryos.* Physiol Meas, 2007. **28**(10): p. 1149-62.

54. Vennemann, P., et al., *In vivo micro particle image velocimetry measurements of blood-plasma in the embryonic avian heart.* Journal of Biomechanics, 2006. **39**(7): p. 1191-1200.

55. Poelma, C., et al., *Measurements of the wall shear stress distribution in the outflow tract of an embryonic chicken heart.* Journal of the Royal Society Interface, 2010. **7**(42): p. 91-103.

56. Chen, C.Y., et al., *Analysis of early embryonic great-vessel microcirculation in zebrafish using high-speed confocal muPIV.* Biorheology, 2011. **48**(5): p. 305-21.

57. Hu, N. and E.B. Clark, *Hemodynamics of the stage 12 to stage 29 chick embryo.* Circ Res, 1989. **65**(6): p. 1665-70.

58. Broekhuizen, M.L., et al., *Hemodynamic parameters of stage 20 to stage 35 chick embryo.* Pediatr Res, 1993. **34**(1): p. 44-6.

59. Phoon, C.K.L., O. Aristizabal, and D.H. Turnbull, *40 MHz Doppler characterization of umbilical and dorsal aortic blood flow in the early mouse embryo.* Ultrasound in Medicine & Biology, 2000. **26**(8): p. 1275-1283.

60. Ursem, N.T., et al., *Dorsal aortic flow velocity in chick embryos of stage 16 to 28.* Ultrasound Med Biol, 2001. **27**(7): p. 919-24.

61. Gui, Y.H., et al., *Doppler echocardiography of normal and abnormal embryonic mouse heart.* Pediatr Res, 1996. **40**(4): p. 633-42.

62. Linask, K.K. and J.C. Huhta, *Use of Doppler echocardiography to monitor embryonic mouse heart function.* Methods Mol Biol, 2000. **135**: p. 245-52.

63. Zhou, Y.Q., et al., *Developmental changes in left and right ventricular diastolic filling patterns in mice.* Am J Physiol Heart Circ Physiol, 2003. **285**(4): p. H1563-75.

64. Butcher, J.T., et al., *Transitions in early embryonic atrioventricular valvular function correspond with changes in cushion biomechanics that are predictable by tissue composition.* Circ Res, 2007. **100**(10): p. 1503-11.

65. Hu, N., et al., *Dependence of aortic arch morphogenesis on intracardiac blood flow in the left atrial ligated chick embryo.* Anat Rec (Hoboken), 2009. **292**(5): p. 652-60.

66. Oosterbaan, A.M., et al., *Doppler flow velocity waveforms in the embryonic chicken heart at developmental stages corresponding to 5-8 weeks of human gestation.* Ultrasound Obstet Gynecol, 2009. **33**(6): p. 638-44.

67. Corrigan, N., D.P. Brazil, and F.M. Auliffe, *High-frequency ultrasound assessment of the murine heart from embryo through to juvenile.* Reprod Sci, 2010. **17**(2): p. 147-57.

68. Hahurij, N.D., et al., *Echocardiographic Assessment of Embryonic and Fetal Mouse Heart Development: A Focus on Haemodynamics and Morphology.* The Scientific World Journal, 2014. **2014**: p. 11.

69. Linask, K.K., M. Han, and N.J.M. Bravo-Valenzuela, *Changes in Vitelline and Utero-Placental Hemodynamics: Implications for Cardiovascular Development.* Frontiers in Physiology, 2014. **5**.

70. Ramasubramanian, A., et al., *On Modeling Morphogenesis of the Looping Heart Following Mechanical Perturbations.* Journal of Biomechanical Engineering, 2008. **130**(6): p. 061018.

71. Davis, A., J. Izatt, and F. Rothenberg, *Quantitative measurement of blood flow dynamics in embryonic vasculature using spectral Doppler velocimetry.* Anat Rec (Hoboken), 2009. **292**(3): p. 311-9.

72. Davis, A.M., et al., *In vivo spectral domain optical coherence tomography volumetric imaging and spectral Doppler velocimetry of early stage embryonic chicken heart development.* J. Opt. Soc. Am. A, 2008. **25**(12): p. 3134-3143.

73. Gargesha, M., et al., *Denoising and 4D visualization of OCT images.* Optics Express, 2008. **16**(16): p. 12313-12333.

74. Gargesha, M., et al., *High temporal resolution OCT using image-based retrospective gating.* Optics Express, 2009. **17**(13): p. 10786-10799.

75. Liu, A., et al., *Efficient postacquisition synchronization of 4-D nongated cardiac images obtained from optical coherence tomography: application to 4-D reconstruction of the chick embryonic heart.* Journal of Biomedical Optics, 2009. **14**(4): p. 044020-044020.

76. Manner, J., et al., *High-resolution in vivo imaging of the cross-sectional deformations of contracting embryonic heart loops using optical coherence tomography.* Dev. Dyn., 2008. **237**(4): p. 953-961.

77. Thrane, L., et al., *Field programmable gate-array-based real-time optical Doppler tomography system for in vivo imaging of cardiac dynamics in the chick embryo.* Optical Engineering, 2009. **48**(2): p. 023201-13.

78. Yelbuz, T.M., et al., *Optical Coherence Tomography: A New High-Resolution Imaging Technology to Study Cardiac Development in Chick Embryos.* Circulation, 2002. **106**(22): p. 2771-2774.

79. Jenkins, M.W., et al., *4D embryonic cardiography using gated optical coherence tomography.* Optics Express, 2006. **14**(2): p. 736-748.

80. Davis, A.M., F. Rothenberg, and J.A. Izatt. *Volumetric Imaging of Chick Embryo Heart Development in vivo Using a High Speed Doppler Spectral Domain OCT Microscope*. in *SPIE (BiOS)*. 2007. San Jose.

81. Filas, B., I. Efimov, and L. Taber, *Optical coherence tomography as a tool for measuring morphogenetic deformation of the looping heart.* Anat Rec, 2007. **290**(9): p. 1057-68.

82. Jenkins, M.W., et al., *Ultrahigh-speed optical coherence tomography imaging and visualization of the embryonic avian heart using a buffered Fourier Domain Mode Locked laser.* Opt. Express, 2007. **15**(10): p. 6251-6267.

83. Norozi, K., et al., *In vivo visualisation of coronary artery development by high-resolution optical coherence tomography.* Heart, 2008. **94**(2): p. 130-.

84. Rugonyi, S., et al., *Changes in wall motion and blood flow in the outflow tract of chick embryonic hearts observed with optical coherence tomography after outflow tract banding and vitelline-vein ligation.* Phys Med Biol, 2008. **53**(18): p. 5077-91.

85. Peterson, L.M., et al., *4D shear stress maps of the developing heart using Doppler optical coherence tomography.* Biomedical Optics Express, 2012. **3**(11): p. 3022-3032.

86. Peterson, L.M., et al., *Orientation-independent rapid pulsatile flow measurement using dual-angle Doppler OCT.* Biomed Opt Express, 2014. **5**(2): p. 499-514.

87. Larina, I.V., et al., *Enhanced OCT imaging of embryonic tissue with optical clearing.* Laser Physics Letters, 2008. **5**(6): p. 476-479.

88. Larina, I.V., et al., *Hemodynamic measurements from individual blood cells in early mammalian embryos with Doppler swept source OCT.* Optics Letters, 2009. **34**(7): p. 986-988.

89. Luo, W., et al., *Three-dimensional optical coherence tomography of the embryonic murine cardiovascular system.* Journal of Biomedical Optics, 2006. **11**(2): p. 021014-8.

90. Jenkins, M.W., et al., *Phenotyping transgenic embryonic murine hearts using optical coherence tomography.* Appl. Opt., 2007. **46**(10): p. 1776-1781.

91. Iftimia, N.V., et al., *Dual-beam Fourier domain optical Doppler tomography of zebrafish.* Optics Express, 2008. **16**(18): p. 13624-13636.

92. Kagemann, L., et al., *Repeated, noninvasive, high resolution spectral domain optical coherence tomography imaging of zebrafish embryos.* Molecular Vision, 2008. **14**(253-55): p. 2157-2170.

93. Bradu, A., et al., *Dual optical coherence tomography/fluorescence microscopy for monitoring of Drosophila melanogaster larval heart.* Journal of Biophotonics, 2009. **2**(6-7): p. 380-388.

94. Choma, M.A., et al., *In Vivo Imaging of the Adult Drosophila melanogaster Heart With Real-Time Optical Coherence Tomography.* Circulation, 2006. **114**(2): p. e35-36.

95. Boppart, S.A., et al., *Noninvasive assessment of the developing Xenopus cardiovascular system using optical coherence tomography.* Proceedings of the National Academy of Sciences, 1997. **94**(9): p. 4256-4261.

96. Yazdanfar, S., M. Kulkarni, and J. Izatt, *High resolution imaging of in vivo cardiac dynamics using color Doppler optical coherence tomography.* Optics Express, 1997. **1**(13): p. 424-431.

97. Yang, V.X.D., et al., *High speed, wide velocity dynamic range Doppler optical coherence tomography (Part II): Imaging in vivo cardiac dynamics of Xenopus laevis.* Optics Express, 2003. **11**(14): p. 1650-1658.

98. Mariampillai, A., et al., *Doppler optical cardiogram gated 2D color flow imaging at 1000 fps and 4D in vivo visualization of embryonic heart at 45 fps on a swept source OCT system.* Optics Express, 2007. **15**(4): p. 1627-1638.

99. Yelin, R., et al., *Multimodality optical imaging of embryonic heart microstructure.* Journal of Biomedical Optics, 2007. **12**(6): p. 064021-12.

100. Huang, D., et al., *Optical coherence tomography.* Science, 1991. **254**(5035): p. 1178-1181.

101. Chen, J. and L. Lee, *Clinical applications and new developments of optical coherence tomography: an evidence-based review.* Clin Exp Optom, 2007. **90**(5): p. 317-35.

102. Yabushita, H., et al., *Characterization of human atherosclerosis by optical coherence tomography.* Circulation, 2002. **106**(13): p. 1640-5.

103. Jang, I.K., et al., *Visualization of coronary atherosclerotic plaques in patients using optical coherence tomography: comparison with intravascular ultrasound.* J Am Coll Cardiol, 2002. **39**(4): p. 604-9.

104.   Wang, Z., et al., *Volumetric quantification of fibrous caps using intravascular optical coherence tomography.* Biomedical Optics Express, 2012. **3**(6): p. 1413-1426.

105.   Rollins, A.M., et al., *Real-time in vivo imaging of human gastrointestinal ultrastructure by use of endoscopic optical coherence tomography with a novel efficient interferometer design.* Optics Letters, 1999. **24**(19): p. 1358-1360.

106.   Kang, W., et al., *Endoscopically guided spectral-domain OCT with double-balloon catheters.* Optics Express, 2010. **18**(16): p. 17364-17372.

107.   Tearney, G.J., et al., *In vivo endoscopic optical biopsy with optical coherence tomography.* Science, 1997. **276**(5321): p. 2037-9.

108.   Pitris, C., et al., *High resolution imaging of the upper respiratory tract with optical coherence tomography: a feasibility study.* Am J Respir Crit Care Med, 1998. **157**(5 Pt 1): p. 1640-4.

109.   Gambichler, T., et al., *Applications of optical coherence tomography in dermatology.* Journal of Dermatological Science. **40**(2): p. 85-94.

110.   Jones, R.S., et al., *Remineralization of in vitro dental caries assessed with polarization-sensitive optical coherence tomography.* J Biomed Opt, 2006. **11**(1): p. 014016.

111.   Choma, M., et al., *Sensitivity advantage of swept source and Fourier domain optical coherence tomography.* Optics Express, 2003. **11**(18): p. 2183-2189.

112.   de Boer, J.F., et al., *Improved signal-to-noise ratio in spectral-domain compared with time-domain optical coherence tomography.* Optics Letters, 2003. **28**(21): p. 2067-2069.

113.   Leitgeb, R., C. Hitzenberger, and A. Fercher, *Performance of fourier domain vs. time domain optical coherence tomography.* Optics Express, 2003. **11**(8): p. 889-894.

114.   Fercher, A.F., et al., *Measurement of intraocular distances by backscattering spectral interferometry.* Optics Communications, 1995. **117**(1–2): p. 43-48.

115.   Wojtkowski, M., et al., *In vivo human retinal imaging by Fourier domain optical coherence tomography.* Journal of Biomedical Optics, 2002. **7**(3): p. 457-463.

116. Chinn, S.R., E.A. Swanson, and J.G. Fujimoto, *Optical coherence tomography using a frequency-tunable optical source.* Optics Letters, 1997. **22**(5): p. 340-342.

117. Golubovic, B., et al., *Optical frequency-domain reflectometry using rapid wavelength tuning of a Cr4+:forsterite laser.* Optics Letters, 1997. **22**(22): p. 1704-1706.

118. Huber, R., M. Wojtkowski, and J.G. Fujimoto, *Fourier Domain Mode Locking (FDML): A new laser operating regime and applications for optical coherence tomography.* Optics Express, 2006. **14**(8): p. 3225-3237.

119. Klein, T., et al. *Multi-MHz retinal OCT imaging using an FDML laser*. in *Biomedical Optics and 3-D Imaging*. 2012. Miami, Florida: Optical Society of America.

120. Zhang, K. and J.U. Kang, *Real-time 4D signal processing and visualization using graphics processing unit on a regular nonlinear-k Fourier-domain OCT system.* Optics Express, 2010. **18**(11): p. 11772-11784.

121. Izatt, J.A., et al., *In vivo bidirectional color Doppler flow imaging of picoliter blood volumes using optical coherence tomography.* Optics Letters, 1997. **22**(18): p. 1439-1441.

122. Chen, Z., et al., *Noninvasive imaging of in vivo blood flow velocity using optical Doppler tomography.* Optics Letters, 1997. **22**(14): p. 1119-1121.

123. Westphal, V., et al., *Real-time, high velocity-resolution color Doppler optical coherence tomography.* Optics Letters, 2002. **27**(1): p. 34-36.

124. Yazdanfar, S., A.M. Rollins, and J.A. Izatt, *IN vivo imaging of human retinal flow dynamics by color doppler optical coherence tomography.* Archives of Ophthalmology, 2003. **121**(2): p. 235-239.

125. Grulkowski, I., et al., *Scanning protocols dedicated to smart velocity ranging in Spectral OCT.* Optics Express, 2009. **17**(26): p. 23736-23754.

126. Yun, S.H., et al., *Motion artifacts in optical coherence tomography with frequency-domain ranging.* Opt Express, 2004. **12**(13): p. 2977-98.

127. Vakoc, B., et al., *Phase-resolved optical frequency domain imaging.* Optics Express, 2005. **13**(14): p. 5483-5493.

128. Hong, Y.J., et al., *High-penetration swept source Doppler optical coherence angiography by fully numerical phase stabilization.* Opt Express, 2012. **20**(3): p. 2740-60.

129. Braaf, B., et al., *Phase-stabilized optical frequency domain imaging at 1-µm for the measurement of blood flow in the human choroid.* Optics Express, 2011. **19**(21): p. 20886-20903.

130. Michaely, R., et al., *Vectorial reconstruction of retinal blood flow in three dimensions measured with high resolution resonant Doppler Fourier domain optical coherence tomography.* Journal of Biomedical Optics, 2007. **12**(4): p. 041213-7.

131. Makita, S., T. Fabritius, and Y. Yasuno, *Quantitative retinal-blood flow measurement with three-dimensional vessel geometry determination using ultrahigh-resolution Doppler optical coherence angiography.* Optics Letters, 2008. **33**(8): p. 836-838.

132. Jenkins, M.W., et al., *Measuring hemodynamics in the developing heart tube with four-dimensional gated Doppler optical coherence tomography.* Journal of Biomedical Optics, 2010. **15**(6): p. 066022-066022.

133. Michaely, R., et al., *Resonant Doppler flow imaging and optical vivisection of retinal blood vessels.* J Biomed. Opt., 2007. **12**: p. 021213.

134. Wang, Y., et al., *In vivo total retinal blood flow measurement by Fourier domain Doppler optical coherence tomography.* Journal of Biomedical Optics, 2007. **12**(4): p. 041215.

135. Wang, Y., et al., *Retinal blood flow measurement by circumpapillary Fourier domain Doppler optical coherence tomography.* Journal of Biomedical Optics, 2008. **13**(6): p. 064003.

136. Wang, Y., et al., *Measurement of total blood flow in the normal human retina using Doppler Fourier-domain optical coherence tomography.* British Journal of Ophthalmology, 2009. **93**(5): p. 634-637.

137. Hwang, J.C., et al., *Relationship among Visual Field, Blood Flow, and Neural Structure Measurements in Glaucoma.* Investigative Ophthalmology & Visual Science, 2012. **53**(6): p. 3020-3026.

138. Ahn, Y.-C., W. Jung, and Z. Chen, *Quantification of a three-dimensional velocity vector using spectral-domain Doppler optical coherence tomography.* Optics Letters, 2007. **32**(11): p. 1587-1589.

139. Haindl, R., et al. *Absolute velocity profile measurement by 3-beam Doppler optical coherence tomography utilizing a MEMS scanning mirror.* in *Biomedical Optics 2014.* 2014. Miami, Florida: Optical Society of America.

140. Davé, D.P. and T.E. Milner, *Doppler-angle measurement in highly scattering media.* Optics Letters, 2000. **25**(20): p. 1523-1525.

141. Werkmeister, R.M., et al., *Bidirectional Doppler Fourier-domain optical coherence tomography for measurement of absolute flow velocities in human retinal vessels.* Optics Letters, 2008. **33**(24): p. 2967-2969.

142. Pedersen, C.J., et al., *Measurement of absolute flow velocity vector using dual-angle, delay-encoded Doppler optical coherence tomography.* Optics Letters, 2007. **32**(5): p. 506-508.

143. Gu, S., et al., *Optical coherence tomography captures rapid hemodynamic responses to acute hypoxia in the cardiovascular system of early embryos.* Dev Dyn, 2012. **241**(3): p. 534-44.

144. Li, P., et al., *In vivo functional imaging of blood flow and wall strain rate in outflow tract of embryonic chick heart using ultrafast spectral domain optical coherence tomography.* Journal of Biomedical Optics, 2012. **17**(9): p. 096006.

145. Liu, A., et al., *Dynamic variation of hemodynamic shear stress on the walls of developing chick hearts: computational models of the heart outflow tract.* Eng. with Comput., 2009. **25**(1): p. 73-86.

146. Liu, A., et al., *Quantifying blood flow and wall shear stresses in the outflow tract of chick embryonic hearts.* Computers and Structures, 2011. **89**(11-12): p. 855-867.

147. van Leeuwen, T.G., et al., *High-flow-velocity and shear-rate imaging by use of color Doppler optical coherence tomography.* Optics Letters, 1999. **24**: p. 1584-1586.

148. Li, P., et al., *Assessment of strain and strain rate in embryonic chick heart in vivo using tissue Doppler optical coherence tomography.* Phys Med Biol, 2011. **56**(22): p. 7081-92.

149. Poelmann, R.E., A.C. Gittenberger-de Groot, and B.P. Hierck, *The development of the heart and microcirculation: role of shear stress.* Med Biol Eng Comput, 2008. **46**(5): p. 479-84.

150. Azuma, N., et al., *Endothelial cell response to different mechanical forces.* Journal of Vascular Surgery, 2000. **32**(4): p. 789-794.

151. Yashiro, K., H. Shiratori, and H. Hamada, *Haemodynamics determined by a genetic programme govern asymmetric development of the aortic arch.* Nature, 2007. **450**(7167): p. 285-288.

152. Hierck, B.P., et al., *Fluid shear stress and inner curvature remodeling of the embryonic heart. Choosing the right lane!* ScientificWorldJournal, 2008. **8**: p. 212-22.

153. Phoon, C.K.L., O. Aristizábal, and D.H. Turnbull, *Spatial velocity profile in mouse embryonic aorta and Doppler-derived volumetric flow: a preliminary model.* American Journal of Physiology - Heart and Circulatory Physiology, 2002. **283**(3): p. H908-H916.

154. Manner, J., et al., *In vivo imaging of the cyclic changes in cross-sectional shape of the ventricular segment of pulsating embryonic chick hearts at stages 14 to 17: a contribution to the understanding of the ontogenesis of cardiac pumping function.* Dev Dyn, 2009. **238**(12): p. 3273-84.

155. Jenkins, M.W., et al., *An environmental chamber based OCT system for high-throughput longitudinal imaging of the embryonic heart*, in *Bios SPIE*. 2008: San Jose.

156. Happel, C.M., et al., *Integration of an optical coherence tomography (OCT) system into an examination incubator to facilitate in vivo imaging of cardiovascular development in higher vertebrate embryos under stable physiological conditions.* Annals of Anatomy - Anatomischer Anzeiger, 2011. **193**(5): p. 425-435.

157. Happel, C.M., et al., *Rotationally acquired four-dimensional optical coherence tomography of embryonic chick hearts using retrospective gating on the common central A-scan.* Journal of Biomedical Optics, 2011. **16**(9): p. 096007-096007.

158. Jenkins, M.W., M. Watanabe, and A.M. Rollins, *Longitudinal Imaging of Heart Development With Optical Coherence Tomography.* Selected Topics in Quantum Electronics, IEEE Journal of, 2012. **18**(3): p. 1166-1175.

159. Goldstein, R.M., H.A. Zebker, and C.L. Werner, *Satellite radar interferometry: Two-dimensional phase unwrapping.* Radio Sci., 1988. **23**(4): p. 713-720.

160. Sato, M., et al. *TEASAR: tree-structure extraction algorithm for accurate and robust skeletons*. in *Computer Graphics and Applications, 2000. Proceedings. The Eighth Pacific Conference on*. 2000.

161. Taylor, C.A., T.J.R. Hughes, and C.K. Zarins, *Finite Element Modeling of Three-Dimensional Pulsatile Flow in the Abdominal Aorta: Relevance to Atherosclerosis.* Annals of Biomedical Engineering, 1998. **26**(6): p. 975-987.

162. Garita, B., et al., *Blood flow dynamics of one cardiac cycle and relationship to mechanotransduction and trabeculation during heart looping.* Am J Physiol Heart Circ Physiol, 2011. **300**(3): p. H879-91.

163. Choi, W., et al., *Measurement of pulsatile total blood flow in the human and rat retina with ultrahigh speed spectral/Fourier domain OCT.* Biomed. Opt. Express, 2012. **3**(5): p. 1047-1061.

164. Yazdanfar, S., A.M. Rollins, and J.A. Izatt, *Imaging and velocimetry of the human retinal circulation with color Doppler optical coherence tomography.* Optics Letters, 2000. **25**(19): p. 1448-1450.

165. Liu, G., et al., *A comparison of Doppler optical coherence tomography methods.* Biomedical Optics Express, 2012. **3**(10): p. 2669-2680.

166. Baumann, B., et al., *Total retinal blood flow measurement with ultrahigh speed swept source/Fourier domain OCT.* Biomed. Opt. Express, 2011. **2**(6): p. 1539-1552.

167. Blatter, C., et al., *Dove prism based rotating dual beam bidirectional Doppler OCT.* Biomed. Opt. Express, 2013. **4**(7): p. 1188-1203.

168. Srinivasan, V.J., et al., *Quantitative cerebral blood flow with Optical Coherence Tomography.* Optics Express, 2010. **18**(3): p. 2477-2494.

169. Schmoll, T. and R.A. Leitgeb, *Heart-beat-phase-coherent Doppler optical coherence tomography for measuring pulsatile ocular blood flow.* Journal of Biophotonics, 2013. **6**(3): p. 275-282.

170. Miura, M., et al., *An Approach to Measure Blood Flow in Single Choroidal Vessel Using Doppler Optical Coherence Tomography.* Investigative Ophthalmology & Visual Science, 2012. **53**(11): p. 7137-7141.

171. Hu, Z. and A. Rollins, *Quasi-telecentric optical design of a microscope-compatible OCT scanner.* Optics Express, 2005. **13**(17): p. 6407-6415.

172. Hu, Z. and A.M. Rollins, *Fourier domain optical coherence tomography with a linear-in-wavenumber spectrometer.* Optics Letters, 2007. **32**(24): p. 3525-3527.

173. Blatter, C., et al., *Angle independent flow assessment with bidirectional Doppler optical coherence tomography.* Optics Letters, 2013. **38**(21): p. 4433-4436.

174. Jaffe, G.J. and J. Caprioli, *Optical coherence tomography to detect and manage retinal disease and glaucoma.* American Journal of Ophthalmology, 2004. **137**(1): p. 156-169.

175. Jindahra, P., et al., *Optical coherence tomography of the retina: applications in neurology.* Curr Opin Neurol, 2010. **23**(1): p. 16-23.

176. Friedman, E., et al., *Ocular Blood Flow Velocity in Age-related Macular Degeneration.* Ophthalmology, 1995. **102**(4): p. 640-646.

177. Remsch, H., et al., *Changes of retinal capillary blood flow in age-related maculopathy.* Graefes Arch Clin Exp Ophthalmol, 2000. **238**(12): p. 960-964.

178. Boltz, A., et al., *Choroidal Blood Flow and Progression of Age-Related Macular Degeneration in the Fellow Eye in Patients with Unilateral Choroidal Neovascularization.* Investigative Ophthalmology & Visual Science, 2010. **51**(8): p. 4220-4225.

179. Flammer, J., *The vascular concept of glaucoma.* Survey of Ophthalmology, 1994. **38 Supplement**(0): p. S3-S6.

180. Flammer, J., et al., *The impact of ocular blood flow in glaucoma.* Progress in Retinal and Eye Research, 2002. **21**(4): p. 359-393.

181. Sakata, K., et al., *Relationship between Macular Microcirculation and Progression of Diabetic Macular Edema.* Ophthalmology, 2006. **113**(8): p. 1385-1391.

182. Landa, G., et al., *Cilioretinal Arteries in Diabetic Eyes Are Associated With Increased Retinal Blood Flow Velocity and Occurrence of Diabetic Macular Edema.* RETINA, 2011. **31**(2): p. 304-311.

183. CDC, *Alcohol use and binge drinking among women of childbearing age - United States, 2006-2010.* MMWR Morb Mortal Wkly Rep, 2012. **61**: p. 534-538.

184. Walker, D.S., et al., *Fetal alcohol spectrum disorders prevention: an exploratory study of women's use of, attitudes toward, and knowledge about alcohol.* J Am Acad Nurse Pract, 2005. **17**(5): p. 187-93.

185. Harwood H, N.D., *Economic implications of the fetal alcohol syndrome.* Alcohol Health and Research World, 1985. **10**: p. 38-43.

186. O'Leary, C.M., et al., *Exploring the potential to use data linkage for investigating the relationship between birth defects and prenatal alcohol exposure.* Birth Defects Research Part A: Clinical and Molecular Teratology, 2013. **97**(7): p. 497-504.

187. Daft, P.A., M.C. Johnston, and K.K. Sulik, *Abnormal heart and great vessel development following acute ethanol exposure in mice.* Teratology, 1986. **33**: p. 95-103.

188. Hiruma, T. and R. Hirakow, *Formation of the pharyngeal arch arteries in the chick embryo. Observations of corrosion casts by scanning electron microscopy.* Anatomy and Embryology, 1995. **191**(5): p. 415-423.

189. Kowalski, W.J., et al., *Critical Transitions in Early Embryonic Aortic Arch Patterning and Hemodynamics.* PLoS ONE, 2013. **8**(3): p. e60271.

190. Karunamuni, G., et al., *Using optical coherence tomography to rapidly phenotype and quantify congenital heart defects associated with prenatal alcohol exposure.* Developmental Dynamics, 2014: p. n/a-n/a.

191. Potsaid, B., et al., *Ultrahigh speed 1050nm swept source / Fourier domain OCT retinal and anterior segment imaging at 100,000 to 400,000 axial scans per second.* Optics Express, 2010. **18**(19): p. 20029-20048.

192. Ainsworth, S.J., R.L. Stanley, and D.J.R. Evans, *Developmental stages of the Japanese quail.* Journal of Anatomy, 2010. **216**(1): p. 3-15.

193. Kirby, M.L. and M.R. Hutson, *Factors controlling cardiac neural crest cell migration.* Cell Adh Migr, 2010. **4**(4): p. 609-21.

194. Poelmann, R.E. and A.C. Gittenberger-de Groot, *A subpopulation of apoptosis-prone cardiac neural crest cells targets to the venous pole: multiple functions in heart development?* Dev Biol, 1999. **207**(2): p. 271-86.

195. High, F.A., et al., *An essential role for Notch in neural crest during cardiovascular development and smooth muscle differentiation.* J Clin Invest, 2007. **117**(2): p. 353-63.

196. Nomura-Kitabayashi, A., et al., *Outflow tract cushions perform a critical valve-like function in the early embryonic heart requiring BMPRIA-mediated signaling in cardiac neural crest.* Am J Physiol Heart Circ Physiol, 2009. **297**(5): p. H1617-28.

197. Hutson, M.R. and M.L. Kirby, *Model systems for the study of heart development and disease. Cardiac neural crest and conotruncal malformations.* Semin Cell Dev Biol, 2007. **18**(1): p. 101-10.

198. Yelbuz, T.M., et al., *Shortened outflow tract leads to altered cardiac looping after neural crest ablation.* Circulation, 2002. **106**(4): p. 504-10.

199. Sulik, K.K., M.C. Johnston, and M.A. Webb, *Fetal alcohol syndrome: embryogenesis in a mouse model.* Science, 1981. **214**(4523): p. 936-8.

200. Kotch, L.E. and K.K. Sulik, *Experimental fetal alcohol syndrome: proposed pathogenic basis for a variety of associated facial and brain anomalies.* Am J Med Genet, 1992. **44**(2): p. 168-76.

201. Cartwright, M.M. and S.M. Smith, *Increased cell death and reduced neural crest cell numbers in ethanol-exposed embryos: partial basis for the fetal alcohol syndrome phenotype.* Alcohol Clin Exp Res, 1995. **19**(2): p. 378-86.

202. Cartwright, M.M., L.L. Tessmer, and S.M. Smith, *Ethanol-induced neural crest apoptosis is coincident with their endogenous death, but is mechanistically distinct.* Alcohol Clin Exp Res, 1998. **22**(1): p. 142-9.

203. Rovasio, R.A. and N.L. Battiato, *Ethanol induces morphological and dynamic changes on in vivo and in vitro neural crest cells.* Alcohol Clin Exp Res, 2002. **26**(8): p. 1286-98.

204. Czarnobaj, J., et al., *The different effects on cranial and trunk neural crest cell behaviour following exposure to a low concentration of alcohol in vitro.* Arch Oral Biol, 2014. **59**(5): p. 500-12.

205. Stewart, D.E., M.L. Kirby, and K.K. Sulik, *Hemodynamic changes in chick embryos precede heart defects after cardiac neural crest ablation.* Circ Res, 1986. **59**(5): p. 545-50.

206. Leatherbury, L., et al., *Hemodynamic changes. Wall stresses and pressure gradients in neural crest-ablated chick embryos.* Ann N Y Acad Sci, 1990. **588**: p. 305-13.

207. Leatherbury, L., et al., *Hemodynamic changes and compensatory mechanisms during early cardiogenesis after neural crest ablation in chick embryos.* Pediatr Res, 1991. **30**(6): p. 509-12.

208. Tomita, H., et al., *Relation of early hemodynamic changes to final cardiac phenotype and survival after neural crest ablation in chick embryos.* Circulation, 1991. **84**(3): p. 1289-95.

209. Kuwajima, T., et al., *ClearT: a detergent- and solvent-free clearing method for neuronal and non-neuronal tissue.* Development, 2013. **140**(6): p. 1364-8.

210. Cirotto, C. and I. Arangi, *How do avian embryos breathe? oxygen transport in the blood of early chick embryos.* Comparative Biochemistry and Physiology Part A: Physiology, 1989. **94**(4): p. 607-613.

211. Burggren, W.W., S.J. Warburton, and M.D. Slivkoff, *Interruption of cardiac output does not affect short-term growth and metabolic rate in day 3 and 4 chick embryos.* J Exp Biol, 2000. **203**(Pt 24): p. 3831-8.

212. Bartman, T., et al., *Early Myocardial Function Affects Endocardial Cushion Development in Zebrafish.* Plos Biology, 2004. **2**(5): p. e129.

213. Abu-Daya, A., et al., *Absence of heartbeat in the Xenopus tropicalis mutation muzak is caused by a nonsense mutation in cardiac myosin myh6.* Dev Biol, 2009. **336**(1): p. 20-9.

214. Rutland, C., et al., *Knockdown of alpha myosin heavy chain disrupts the cytoskeleton and leads to multiple defects during chick cardiogenesis.* J Anat, 2009. **214**(6): p. 905-15.

215. Huang, C., et al., *Embryonic atrial function is essential for mouse embryogenesis, cardiac morphogenesis and angiogenesis.* Development, 2003. **130**(24): p. 6111-9.

216. Fritz-Six, K.L., et al., *Aberrant myofibril assembly in tropomodulin1 null mice leads to aborted heart development and embryonic lethality.* The Journal of Cell Biology, 2003. **163**(5): p. 1033-1044.

217. Koushik, S.V., et al., *Targeted inactivation of the sodium-calcium exchanger (Ncx1) results in the lack of a heartbeat and abnormal myofibrillar organization.* The FASEB Journal, 2001. **15**(7): p. 1209-1211.

218. Forouhar, A.S., et al., *The Embryonic Vertebrate Heart Tube Is a Dynamic Suction Pump.* Science, 2006. **312**(5774): p. 751-753.

219. Wang, Y.T., et al., *Optical stimulation enables paced electrophysiological studies in embryonic hearts.* Biomedical Optics Express, 2014. **5**(4): p. 1000-1013.

220. Ma, P., et al., *Three-dimensional correction of conduction velocity in the embryonic heart using integrated optical mapping and optical coherence tomography.* Journal of Biomedical Optics, 2014. **19**(7): p. 076004-076004.

221. Jian, Y., K. Wong, and M.V. Sarunic, *Graphics processing unit accelerated optical coherence tomography processing at megahertz axial scan rate and high resolution video rate volumetric rendering.* Journal of Biomedical Optics, 2013. **18**(2): p. 026002-026002.